

博士論文

**Kinetic and Spectroscopic Studies of Catalytic
Mechanisms: Hydrodeoxygenation of γ -Valerolactone
on Transition Metal Phosphide Catalysts**

(遷移金属リン化触媒を用いた γ バレロラク톤の水素化脱酸素反応における触媒反応機構の速度論的および分光学的研究)

Gwang-Nam Yun

尹 光男

Thesis Evaluation Committee

Professor Kazunari Domen, The University of Tokyo

Professor Masaru Ogura, The University of Tokyo

Professor Tetsuya Shishido, The University of Tokyo Metropolitan

Professor Ryuji Kikuchi, The University of Tokyo

Professor Tsutomu Minegishi, The University of Tokyo

Professor S. Ted Oyama (Supervisor), The University of Tokyo

Chapter 1

Research Background and General Introduction

1.1	Biomass as a sustainable energy resource	5
1.2	Catalytic upgrading of bio-oil: Hydrodeoxygenation (HDO)	8
1.3	Transition metal phosphide catalysts	10
1.4	Dissertation overview	13

Chapter 2

Hydrodeoxygenation of γ -Valerolactone on Transition Metal Phosphide Catalysts

2.1	Introduction	23
2.2	Experimental	26
2.2.1	Preparation of supported transition metal phosphide catalysts	26
2.2.2	Characterization of prepared catalyst samples	27
2.2.3	Activity test for HDO of GVL	28
2.3	Results and discussion	30
2.3.1	Characterizations of the prepared catalysts	30
2.3.2	Catalyst stability test	35
2.3.3	Reactivity as a function of temperature	36
2.3.4	Reaction network for HDO of GVL	46
2.4	Conclusion	50
2.5	Supplemental information	51
2.6	Appendix	52

Chapter 3

Hydrodeoxygenation of γ -Valerolactone on Bimetallic NiMo Phosphide Catalysts

3.1	Introduction	61
3.2	Experimental	64
3.2.1	Preparation of bimetallic phosphide catalysts	64
3.2.2	Characterizations	65
3.2.3	Activity testing	66

3.3	Results and discussion	68
3.3.1	Synthesis and characterization	68
3.3.2	Reactivity studies	79
3.4	Conclusion	90

Chapter 4

Kinetic and Spectroscopic Studies of Catalytic Mechanisms: Hydrodeoxygenation of γ -Valerolactone on Ni₂P/MCM-41

4.1	Introduction	97
4.2	Experimental	99
4.2.1	Preparation and characterization of Ni ₂ P supported on MCM-41	99
4.2.2	Catalytic activity test	100
4.2.3	In situ Fourier transform infrared spectroscopy (FTIR) measurement	101
4.2.4	In situ quick X-ray absorption fine-structure (QXAFS) measurement	102
4.3	Results and discussion	104
4.3.1	Characterization of Ni ₂ P/MCM-41 catalyst	104
4.3.2	Contact time analysis and reaction network	105
4.3.3	Partial pressure analysis	110
4.3.4	In situ Fourier transform infrared spectroscopy (FTIR) analysis	116
4.3.5	In situ extended X-ray absorption fine structure (EXAFS) analysis	121
4.4	Conclusion	126

Chapter 5

General Conclusion

Publication List	136
Acknowledgement	137

Chapter 1

Research Background and General Introduction

1.1 Biomass as a sustainable energy resource

The world energy demand is significantly growing and it is expected that total energy consumption will increase from 549 quadrillion British thermal units (Btu) in 2012 to 815 quadrillion Btu in 2040. This increase in demand cannot be met by the existing energy sources. Furthermore, liquid fuels derived from crude oil, which currently account for more than one-third of the global primary energy supply and more than 95 % of transportation energy use according to the International Energy Outlook 2016 (IEO2016) shown in Fig.1.1 [1], are estimated to be depleted within 50 years.

Thus, it is imperative to find alternative energy resource [2].

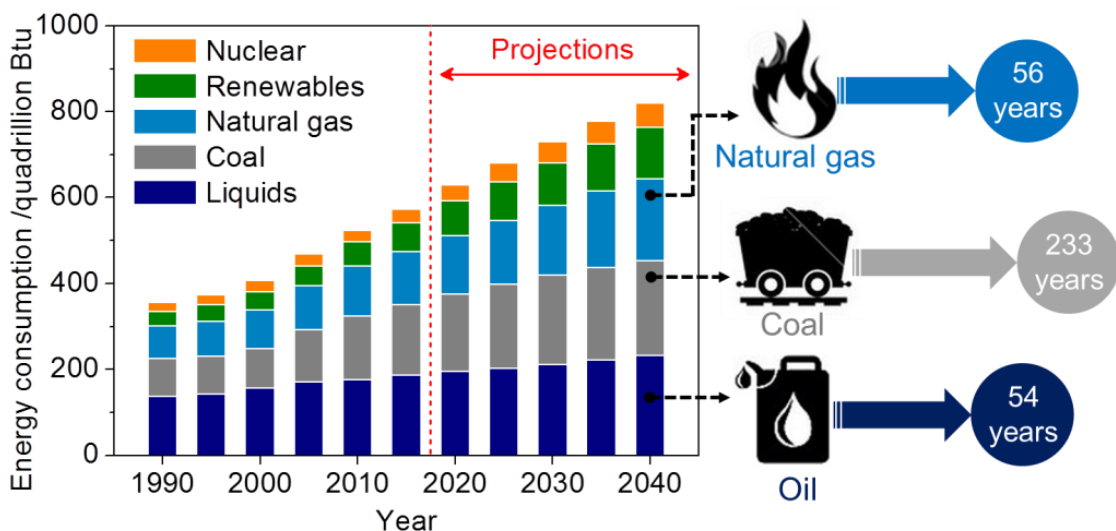


Figure 1.1. Worldwide energy consumption and depletion of energy resources as reported in International Energy Outlook 2016 (IEO2016) [1]

To address the looming energy crisis, biomass has received considerable attention as a sustainable energy resource to replace crude oil because it is available in various forms and can be grown in relative ease around the world. Biomass is derived from municipal solid wastes, animal residues, industrial residues, forestry crops, agricultural crops, and sewage. For that reasons, several approaches for fuel production from biomass have been developed as shown in Fig. 1.2.

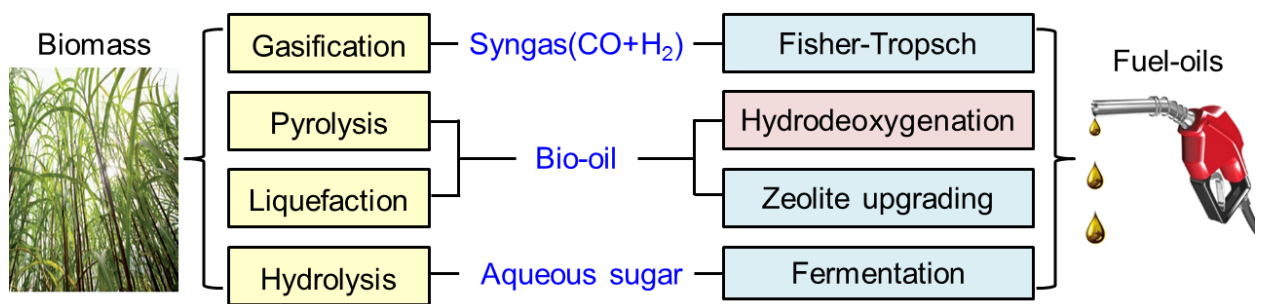


Figure 1.2. Strategies for biomass upgrading into fuel oils

Four of the processes can be considered as the main pathways to transform biomass to transportation fuel as shown in Fig. 1.2. They include gasification to syngas, followed by Fisher-Tropsch synthesis; pyrolysis or liquefaction to bio-oils, followed by catalytic upgrading (zeolite upgrading and hydrodeoxygenation); and hydrolysis to aqueous sugar, followed by aqueous-phase catalytic processing or fermentation [3-5].

Gasification is the thermochemical conversion of solid biomass into combustible and flammable fuel such as syngas ($\text{CO}+\text{H}_2$), methane and other hydrocarbons in a low oxygen condition [6, 7]. Leijenhurst et al. reported that staged biomass gasification by autothermal catalytic reforming achieved high overall energetic efficiency (65 % for clean wood and 55 % for residue materials) [8]. Wang et al. reported that biomass gasification in a pilot scale two-stage gasification gasifier for BTL (biomass to liquid)

via one-step DME (dimethyl ether) synthesis reached 80 % of carbon conversion efficiency with more than 70 vol. % of $H_2 + CO$ and $H_2/CO = 1$ [9]. Even though these studies demonstrate the capability to utilize various sources of biomass to produce more readily usable fuel, it is energy-intensive (750-900 °C) which limits the economic viability of the process [10].

Fermentation is an anaerobic biological process involving a series of chemical reactions to produce ethanol with addition of bacteria or yeast. Tavva et al. studied bioethanol production via hydrolysis and fermentation of *Partheniumhysterophorus* biomass and attained 0.24-0.27 $g_{ethanol}/g_{biomass}$ [11]. Yeh et al. reported that high ethanol yield (0.124 wt. %) was achieved from raw material of *M. floridulus* by simultaneous saccharification and fermentation [12]. However, since fermentation uses bacteria or yeast, they cannot be applied at high temperature which limits their application.

Hydrothermal liquefaction is one of the thermochemical conversion routes and carried out at around 250-375 °C and 4-22 MPa under pressurized water environment to depolymerize the solid feedstock into mainly liquid components [13, 14]. Li et al. reported that hydrothermal treatment of bagasse lignin at 200 °C for 30 min under microwave irradiation led to 79 % yield of liquefied products consisting of single- or double-displacement phenolic compounds [15]. However, this process is still constrained by heat and mass transfer limitations and the formation of undesirable products, resulting in low efficiency; furthermore, additional separation, purification and/or modification systems are required to improve products selectivity [16].

Pyrolysis is the other thermochemical method and is operated at moderate temperature of around 500 °C and very short reaction times of up to 2 s in the absence of oxygen [17]. Huber et al. proposed modified fast pyrolysis which can achieve high

yields of bio-oil (around 80 wt.%) with up to 70 % of the energy of the biomass feedstock [18]. Xue et al. reported the fast pyrolysis of biomass and waste plastic in a fluidized bed reactor, and obtained 58 wt. % yield of pyrolysis oil with higher heating value (HHV) up to 36.6 MJ/kg at 625 °C [19]. These merits will eventually lead to proclaim that the pyrolysis is most suitable process for biomass upgrading into liquid fuels.

1.2 Catalytic upgrading of bio-oil: Hydrodeoxygenation

Among the primary conversion technologies, pyrolysis has gained considerable attention because it is the simplest and the most cost-effective method, and thus the produced bio-oil has become a potential source of renewable liquid fuels [20, 21]. However, unlike conventional fuel-oil (Table 1.1 [22, 23]), the bio-oil has a high oxygen content (36-52 wt.%) in the form of water, acids, esters, alcohols, aldehydes, guaiacols, furans, pyrans, acetic acid, formic acid, carboxylic acids, and ketones as shown in Fig. 1.3 [18, 24-26].

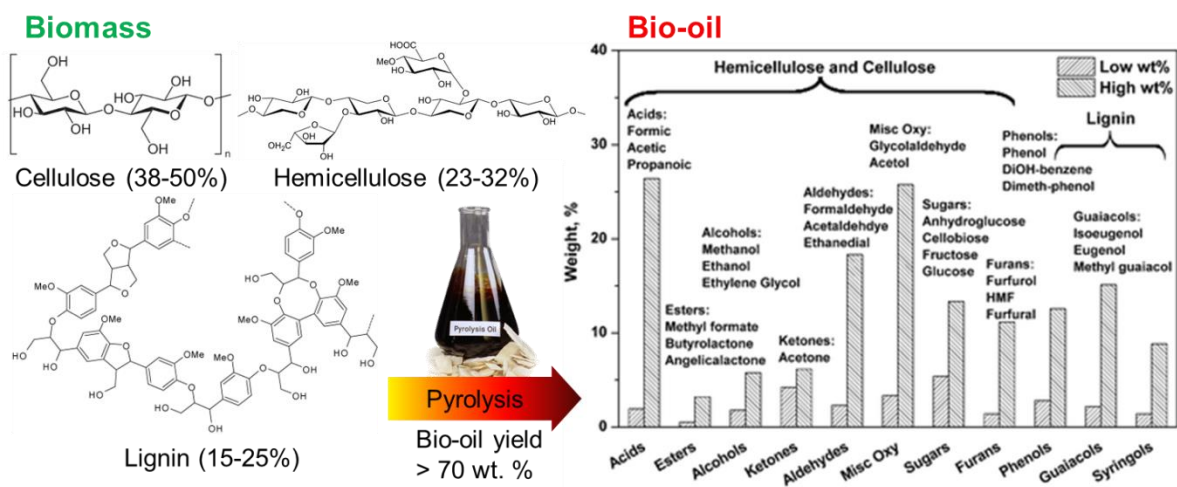


Figure 1.3. Composition of biomass and bio-oil [18]

Table 1.1. Typical compositions and physical properties of bio-oil and fuel oil [22, 23]

	Pyrolysis bio-oil	Fuel-oil
Carbon /wt. %	40 – 50	85
Hydrogen /wt. %	6.0 – 7.6	11–13
Oxygen /wt. %	36 – 52	0.1–1.0
Sulfur /wt. %	0.00 – 0.02	1.0–1.8
Nitrogen /wt. %	0.00 – 0.15	0.1
Water /wt. %	15 – 30	0.02–0.1
pH	2.8 – 3.8	-
Viscosity (50 °C) /cP	40 – 100	180
HHV /MJkg ⁻¹	16 – 19	44
Density /kgm ⁻³	1.2–1.3	0.86–0.94

The presence of these oxygenates leads to undesirable characteristics such as low heating value, high acidity, and chemical and thermal instability [23]. Therefore, the oxygen in bio-oil needs to be removed to obtain liquid fuel of required quality.

In this regard, the two processes that have received the most attention are zeolite upgrading and hydrodeoxygenation (HDO). Zeolite upgrading is a catalytic cracking reaction to remove oxygen in bio-oil in the forms of CO, CO₂, and H₂O at high temperature (300-600 °C) and atmospheric pressure without H₂ [27]. However, this process results in low hydrocarbon yield due to coke formation and dealumination of zeolite, which deactivates the catalysts [17]. The HDO is a hydroprocessing reaction to remove oxygen in form of H₂O in the presence of H₂ with production of hydrocarbons by saturating C=O bond, cleaving C-O, and forming C-H bond [17, 28, 29]. It is analogous to hydrodesulfurization (HDS) [30-34] and hydrodenitrogenation (HDN) [35-37], which are the critical processes in modern oil refining to produce usable liquid fuels [38-40], to remove sulfur and nitrogen heteroatoms, respectively, from petroleum crude. Unlike HDS and HDN, the HDO had received little attention because of the low

oxygen content (< 0.3 wt. %) in crude oil feedstock [17, 41]. However, interest in biomass over the last decade has stimulated research in HDO.

1.3 Transition metal phosphide catalysts

Hydrodeoxygenation of bio-oil is complicated by the different reactivity of oxygenates shown in Fig. 1.3. It is known that reactivity follows the order: alcohols > ketones > alkylethers > carboxylic acids > phenols > furans > benzofurans > dibenzofurans [41], and thus several HDO studies have focused on model compounds to elucidate reaction pathways relevant to upgrading of actual bio-oil feed. Another challenging aspect of HDO reaction is the development of effective catalysts. In that regard, model compound studies are also relevant towards providing detailed insights into factors controlling catalyst performance in order to develop novel catalysts. Initial HDO studies used commercial HDS and HDN catalysts, transition metal sulfide catalysts (CoMoS and NiMoS) supported on γ -Al₂O₃, due to the similarities between hydroprocessing reactions and applicable to current infrastructures. In a previous study, the HDO of waste oils was carried out in a high-pressure batch reactor and a fixed bed flow reactor at 250-350 °C over transition metal sulfide catalysts, in which NiMoS and NiWS catalysts showed high and stable activity, whereas CoMoS catalyst suffered from deactivation [42]. A study of the HDO of phenol and 2-ethylphenol over sulfided Mo/Al₂O₃ and CoMo/Al₂O₃ catalysts showed that HDO followed two pathways: hydrogenation of the aromatic ring followed by C_{sp3}-O bond cleavage (HYD pathway) or direct cleavage of the C_{sp2}-O bond (DDO pathway). The addition of Co favored both pathways, but the presence of the alkyl substituent on the phenolic ring led to DDO pathway being more favored over the HYD pathway [43]. Even though studies over

sulfide catalysts provided initial insight into several important factors in HDO, the application of sulfide catalysts for bio-oil upgrading is hampered by their need for a sulfur source to maintain their activity, leading to increased interest in non-sulfide catalysts [44, 45].

Transition metal phosphide catalysts (metal-rich compounds, MP or M_2P) [40], which have been demonstrated to be effective HDS and HDN catalysts [40], are considered as alternative catalysts for HDO as summarized in Table 1.2. Recently, numerous studies over transition metal phosphide catalysts have been reported for HDO of bio-oil model compounds (dibenzofuran [46-48], furans [49-51], phenols [52-54], guaiacol [44, 55, 56] and ketones [57]) as well as bio-oil feedstock (soybean oil [58], palm oil [59] and cedar chips oil [60]). A study of HDO of 2-methyltetrahydrofuran (2-MTHF) on a series of silica-supported transition metal phosphide catalysts was performed and the catalytic activity was found to follow the order: $Ni_2P > WP > MoP > CoP > FeP > Pd/Al_2O_3$ [51]. Furthermore, a series of studies for HDO of 2-MTHF on Ni_2P/SiO_2 suggested that rate-determining step involves ring-opening steps [49-51]. It has been previously reported that during HDO of guaiacol, a commercial $CoMoS/Al_2O_3$ catalyst quickly deactivated and exhibited lower activity compared to the phosphide catalysts at the same reaction conditions, while a commercial Pd/Al_2O_3 catalyst mainly produced undesirable catechol [44].

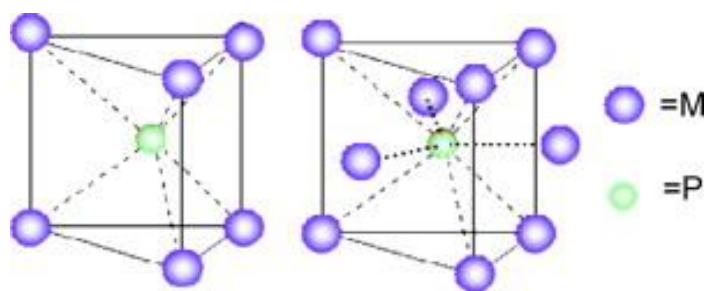


Figure 1.4 Triangular prism (mono-phosphide-MP) and tetrakaidecahedral structures (metal-rich phosphide- M_2P) in phosphides [40]

Table 1.2. Summary of HDO of bio-oil and its model compounds on transition metal phosphide catalysts

Year	Catalysts	Reactants	Reference
2011	Ni ₂ P/SiO ₂ , MoP/SiO ₂ , NiMoP/SiO ₂	Anisole	K.Li [61]
2011	Ni ₂ P/SiO ₂ , Co ₂ P/SiO ₂ , Fe ₂ P/SiO ₂ , WP/SiO ₂ , MoP/SiO ₂	Guaiacol	H. Y. Zhao [44]
2012	Ni ₂ P/SiO ₂ , CoP/SiO ₂ , FeP/SiO ₂ , WP/SiO ₂ , MoP/SiO ₂	2-Methyltetrahydrofuran	P. Bui [62]
2012	Ni ₂ P/SiO ₂ , FeP/SiO ₂ , NiFeP/SiO ₂	2-Methyltetrahydrofuran	A. Cho [63]
2012	unsupported MoP	4-Methylphenol	V.M.L.Whiffen[54]
2013	Ni ₂ P/SiO ₂	Dibenzofuran	J.A.Cecilia[47]
2013	unsupported Ni-P	p-Cresol	W. Y. Wang[64]
2013	Ni ₂ P/ZrO ₂ , Ni ₂ P/Al ₂ O ₃ , Ni ₂ P/SiO ₂	Guaiacol	S. K.Wu[65]
2014	MoP/TiO ₂	Phenol	S.Boullosa-Eiras[52]
2014	CoP/Al ₂ O ₃	2-Fury methyl ketone	T. A.Le[57]
2015	Ni ₂ P/SiO ₂	Methyl palmitate	F.Han[66]
2015	Ni ₂ P/SiO ₂ ,CoP/SiO ₂	Dibenzofuran	A.Infantes-Molina[46]
2015	Ni ₂ P/USY	2-Methyltetrahydrofuran	A. Cho[67]
2015	Ni ₂ P/SAPO-11	Castor oil	S. Y.Liu[68]
2015	Ni ₂ P/ASA, Ni ₂ P/FCC, Ni ₂ P/ZSM-5	Guaiacol	S. T.Oyama[69]
2015	Ni ₂ P/MCM-41	Benzofuran	H.Song[70]
2015	Ni ₂ P/SBA-15, Fe/SBA-15, CoP/SBA-15, MoP/SBA-15	Methyl ester, Methyl oleate	Y. X.Yang[71]
2015	Ni ₂ P/SiO ₂ , Ni ₂ P/HY	Soybean oil	R.Zarchin[58]
2016	Ni ₂ P, Co ₂ P and MoP supported on Al-SBA-15, gamma-Al ₂ O ₃ and ordered mesoporous carbon	Phenol	A.Berenguer[72]
2016	MoP, Mo ₈ WP ₉ , Mo ₈ CuP ₉ Ni ₂ P, Ni ₃₈ W ₂ P ₂₀	Methyl palmitate	M. Y.Lu[73]
2016	Ni ₂ P/SiO ₂	Cedar chips oil	N.Koike[60]
2016	Ni ₂ P/Al ₂ O ₃ , MoP/Al ₂ O ₃	Palmitic acid	M.Peroni[74]
2016	FeMoP	Phenol	D. J.Rensel[75]
2016	Ni ₂ P/Al ₂ O ₃ @TiO ₂	Benzofuran	H.Song[76]
2017	Ni ₂ P/SiO ₂	m-Cresol, p-Cresol and o-Cresol	V. O. O.Goncalves[77]
2017	Ni ₂ P/MCM-41, CoP/MCM-41, WP/MCM-41, MoP/MCM-41	γ-Valerolactone	G. N. Yun [78]

1.4 Dissertation overview

Chapter 1 describes the general motivation of this research, which is the use of biomass as a sustainable energy resource to replace petroleum liquid fuels. Then, literature review provides information including strategies for biomass upgrading and catalyst development for bio-oil.

Chapter 2 describes a series of transition metal phosphide catalysts supported on MCM-41 ($\text{Ni}_2\text{P}/\text{MCM-41}$, $\text{CoP}/\text{MCM-41}$, $\text{MoP}/\text{MCM-41}$, and $\text{WP}/\text{MCM-41}$) to investigate its activity in the hydrodeoxygenation (HDO) of γ -valerolactone (GVL). The performance, including catalytic activity and product selectivity, are compared at various temperatures with those of a commercial $\text{Pd}/\text{Al}_2\text{O}_3$ catalyst.

Chapter 3 describes a series of bimetallic NiMoP catalysts with various Ni and Mo metal to investigate its activity in the HDO of GVL at 0.5 MPa. Analysis by XRD indicated the formation of phase pure alloy and surface site was titrated with CO uptake and Fourier transform infrared (FTIR) was used to distinguish adsorption on Ni and Mo sites. It was found that surface Ni atoms controlled the reactivity, but that Mo atoms influenced the selectivity.

Chapter 4 describes a kinetic analysis of the reaction network of GVL on $\text{Ni}_2\text{P}/\text{MCM-41}$ by contact time measurements, and to investigate the effects of GVL and H_2 partial pressures. Furthermore, the adsorbed species on the catalyst surface and the working state of Ni species during the reaction were monitored by in situ infrared spectroscopy and in situ quick x-ray adsorption fine structure measurement to support the proposed reaction sequence. These measurements and analyses are important to obtain basic information about the manner of oxygen removal using $\text{Ni}_2\text{P}/\text{MCM-41}$.

References

- [1] U.S.E.I. Administration, International Energy Outlook 2016, in, 2016.
- [2] B. stats, BP Statistical Review of World Energy June 2016, in, 2016.
- [3] S. Kassaye, K.K. Pant, S. Jain, Hydrolysis of cellulosic bamboo biomass into reducing sugars via a combined alkaline solution and ionic liquid pretreatment steps, *Renew Energ* 104 (2017) 177-184.
- [4] H. Kobayashi, H. Kaiki, A. Shrotri, K. Techikawara, A. Fukuoka, Hydrolysis of woody biomass by a biomass-derived reusable heterogeneous catalyst, *Chem Sci* 7 (2016) 692-696.
- [5] D. Pieprzyk-Kokocha, A. Wawro, J. Batog, Hydrolysis Process of Sorghum and Miscanthus Biomass Using Cellulolytic Enzymes for Ethanol Production, *Cellul. Chem. Technol.* 50 (2016) 401-404.
- [6] S.K. Sansaniwal, K. Pal, M.A. Rosen, S.K. Tyagi, Recent advances in the development of biomass gasification technology: A comprehensive review, *Renewable and Sustainable Energy Reviews* 72 (2017) 363-384.
- [7] M. La Villetta, M. Costa, N. Massarotti, Modelling approaches to biomass gasification: A review with emphasis on the stoichiometric method, *Renewable and Sustainable Energy Reviews* 74 (2017) 71-88.
- [8] E.J. Leijenhorst, W. Wolters, B. van de Beld, W. Prins, Staged Biomass Gasification by Autothermal Catalytic Reforming of Fast Pyrolysis Vapors, *Energy Fuels* 29 (2015) 7395-7407.
- [9] Z.Q. Wang, T. He, J.G. Qin, J.L. Wu, J.Q. Li, Z.Y. Zi, G.B. Liu, J.H. Wu, L. Sun, Gasification of biomass with oxygen-enriched air in a pilot scale two-stage gasifier, *Fuel* 150 (2015) 386-393.
- [10] A.V. Bridgwater, Review of fast pyrolysis of biomass and product upgrading, *Biomass Bioenergy* 38 (2012) 68-94.
- [11] S.S.M.D. Tavva, A. Deshpande, S.R. Durbha, V.A.R. Palakollu, A.U. Goparaju, V.R. Yechuri, V.R. Bandaru, V.S.R. Muktinutalapati, Bioethanol production through separate hydrolysis and fermentation of *Parthenium hysterophorus* biomass, *Renew Energ* 86 (2016) 1317-1323.

- [12] R.H. Yeh, Y.S. Lin, T.H. Wang, W.C. Kuan, W.C. Lee, Bioethanol production from pretreated *Miscanthus floridulus* biomass by simultaneous saccharification and fermentation, *Biomass Bioenerg* 94 (2016) 110-116.
- [13] D.C. Elliott, P. Biller, A.B. Ross, A.J. Schmidt, S.B. Jones, Hydrothermal liquefaction of biomass: developments from batch to continuous process, *Bioresour. Technol.* 178 (2015) 147-156.
- [14] B. Patel, P. Arcelus-Arrillaga, A. Izadpanah, K. Hellgardt, Catalytic Hydrotreatment of algal biocrude from fast Hydrothermal Liquefaction, *Renew Energ* 101 (2017) 1094-1101.
- [15] Y.M. Li, B.Z. Li, F.L. Du, Y. Wang, L.X. Pan, D. Chen, Microwave-assisted hydrothermal liquefaction of lignin for the preparation of phenolic formaldehyde adhesive, *J. Appl. Polym. Sci.* 134 (2017).
- [16] K.Q. Tran, Fast hydrothermal liquefaction for production of chemicals and biofuels from wet biomass - The need to develop a plug-flow reactor, *Bioresour. Technol.* 213 (2016) 327-332.
- [17] H.M. Wang, J. Male, Y. Wang, Recent advances in hydrotreating of pyrolysis bio-oil and its oxygen-containing model compounds, *ACS Catal.* 3 (2013) 1047-1070.
- [18] G.W. Huber, S. Iborra, A. Corma, Synthesis of transportation fuels from biomass: Chemistry, catalysts, and engineering, *Chem. Rev.* 106 (2006) 4044-4098.
- [19] Y. Xue, S. Zhou, R.C. Brown, A. Kelkar, X.L. Bai, Fast pyrolysis of biomass and waste plastic in a fluidized bed reactor, *Fuel* 156 (2015) 40-46.
- [20] S. Czernik, A.V. Bridgwater, Overview of applications of biomass fast pyrolysis oil, *Energy Fuels* 18 (2004) 590-598.
- [21] R.P. Anex, A. Aden, F.K. Kazi, J. Fortman, R.M. Swanson, M.M. Wright, J.A. Satrio, R.C. Brown, D.E. Daugaard, A. Platon, G. Kothandaraman, D.D. Hsu, A. Dutta, Techno-economic comparison of biomass-to-transportation fuels via pyrolysis, gasification, and biochemical pathways, *Fuel* 89 (2010) S29-S35.
- [22] C.J. Liu, H.M. Wang, A.M. Karim, J.M. Sun, Y. Wang, Catalytic fast pyrolysis of lignocellulosic biomass, *Chem. Soc. Rev.* 43 (2014) 7594-7623.
- [23] T. Dickerson, J. Soria, Catalytic Fast Pyrolysis: A Review, *Energies* 6 (2013) 514-538.

- [24] D. Mohan, C.U. Pittman, P.H. Steele, Pyrolysis of wood/biomass for bio-oil: A critical review, *Energy Fuels* 20 (2006) 848-889.
- [25] Z.Q. Hu, L.Z. Zhang, Z.Y. Liu, B. Xiao, S.M. Liu, Experimental study on bio-oil production from pyrolysis of biomass micron fuel (BMF) in a free-fall reactor, *Fuel* 106 (2013) 552-557.
- [26] Y. Yu, Y.W. Chua, H.W. Wu, Characterization of Pyrolytic Sugars in Bio-Oil Produced from Biomass Fast Pyrolysis, *Energy Fuels* 30 (2016) 4145-4149.
- [27] E.F. Iliopoulou, S.D. Stefanidis, K.G. Kalogiannis, A. Delimitis, A.A. Lappas, K.S. Triantafyllidis, Catalytic upgrading of biomass pyrolysis vapors using transition metal-modified ZSM-5 zeolite, *Appl. Catal. B: Environ.* 127 (2012) 281-290.
- [28] Y. Elkasabi, C.A. Mullen, A.L.M.T. Pighinelli, A.A. Boateng, Hydrodeoxygenation of fast-pyrolysis bio-oils from various feedstocks using carbon-supported catalysts, *Fuel Process. Technol.* 123 (2014) 11-18.
- [29] H. Lee, H. Kim, M.J. Yu, C.H. Ko, J.K. Jeon, J. Jae, S.H. Park, S.C. Jung, Y.K. Park, Catalytic Hydrodeoxygenation of Bio-oil Model Compounds over Pt/HY Catalyst, *Sci Rep-Uk* 6 (2016).
- [30] X.L. Wang, Z. Zhao, P. Zheng, Z.T. Chen, A.J. Duan, C.M. Xu, J.Q. Jiao, H.L. Zhang, Z.K. Cao, B.H. Ge, Synthesis of NiMo catalysts supported on mesoporous Al₂O₃ with different crystal forms and superior catalytic performance for the hydrodesulfurization of dibenzothiophene and 4,6-dimethyldibenzothiophene, *J. Catal.* 344 (2016) 680-691.
- [31] L. Zhang, W.Q. Fu, Q.Y. Yu, T.D. Tang, Y.C. Zhao, H.W. Zhao, Y.D. Li, Ni₂P clusters on zeolite nanosheet assemblies with high activity and good stability in the hydrodesulfurization of 4,6-dimethyldibenzothiophene, *J. Catal.* 338 (2016) 210-221.
- [32] L. Yang, X. Li, A.J. Wang, R. Prins, Y.Y. Chen, X.P. Duan, Hydrodesulfurization of dibenzothiophene, 4,6-dimethyldibenzothiophene, and their hydrogenated intermediates over bulk tungsten phosphide, *J. Catal.* 330 (2015) 330-343.
- [33] M. Zdražil, The Chemistry of the Hydrodesulfurization Process (Review), *Appl Catal* 4 (1982) 107-125.

- [34] G.C.A. Schuit, B.C. Gates, Chemistry and Engineering of Catalytic Hydrodesulfurization, *AIChE J.* 19 (1973) 417-438.
- [35] V. Zuzaniuk, R. Prins, Synthesis and characterization of silica-supported transition-metal phosphides as HDN catalysts, *J. Catal.* 219 (2003) 85-96.
- [36] R.H. Fish, A.D. Thormodsen, R.S. Moore, D.L. Perry, H. Heinemann, Hydrodenitrogenation Chemistry .1. Cleavage of Alkylcarbon-Nitrogen Bonds, Methane and Ammonia Formation in the Hdn Reaction of 1,2,3,4-Tetrahydroquinoline with a Nickel-Oxide Catalyst Supported on Silica-Alumina, *J. Catal.* 102 (1986) 270-273.
- [37] W.B. Chen, H. Nie, D.D. Li, X.Y. Long, J. van Gestel, F. Mauge, Effect of Mg addition on the structure and performance of sulfide Mo/Al₂O₃ in HDS and HDN reaction, *J. Catal.* 344 (2016) 420-433.
- [38] C. Peng, X.C. Fang, R.H. Zeng, R. Guo, W.Y. Hao, Commercial analysis of catalytic hydroprocessing technologies in producing diesel and gasoline by light cycle oil, *Catal. Today* 276 (2016) 11-18.
- [39] B. Thinnes, KBR and Shell Global Solutions plan to expand their hydroprocessing technology alliance. In addition to, *Hydrocarb Process* 91 (2012) 7-7.
- [40] S.T. Oyama, T. Gott, H.Y. Zhao, Y.K. Lee, Transition metal phosphide hydroprocessing catalysts: A review, *Catal. Today* 143 (2009) 94-107.
- [41] E. Furimsky, Catalytic hydrodeoxygenation, *Appl. Catal. A: Gen.* 199 (2000) 147-190.
- [42] M. Toba, Y. Abe, H. Kuramochi, M. Osako, T. Mochizuki, Y. Yoshimura, Hydrodeoxygenation of waste vegetable oil over sulfide catalysts, *Catal. Today* 164 (2011) 533-537.
- [43] M. Badawi, J.F. Paul, E. Payen, Y. Romero, F. Richard, S. Brunet, A. Popov, E. Kondratieva, J.P. Gilson, L. Mariey, A. Travert, F. Mauge, Hydrodeoxygenation of Phenolic Compounds by Sulfided (Co)Mo/Al₂O₃ Catalysts, a Combined Experimental and Theoretical Study, *Oil Gas Sci Technol* 68 (2013) 829-840.
- [44] H.Y. Zhao, D. Li, P. Bui, S.T. Oyama, Hydrodeoxygenation of guaiacol as model compound for pyrolysis oil on transition metal phosphide hydroprocessing catalysts, *Appl. Catal. A: Gen.* 391 (2011) 305-310.

- [45] E.M. Ryymin, M.L. Honkela, T.R. Viljava, A.O.I. Krause, Insight to sulfur species in the hydrodeoxygenation of aliphatic esters over sulfided NiMo/ γ -Al₂O₃ catalyst, *Appl. Catal. A: Gen.* 358 (2009) 42-48.
- [46] A. Infantes-Molina, E. Gralberg, J.A. Cecilia, E. Finocchio, E. Rodriguez-Castellon, Nickel and cobalt phosphides as effective catalysts for oxygen removal of dibenzofuran: role of contact time, hydrogen pressure and hydrogen/feed molar ratio, *Catal. Sci. Technol.* 5 (2015) 3403-3415.
- [47] J.A. Cecilia, A. Infantes-Molina, E. Rodriguez-Castellon, A. Jimenez-Lopez, S.T. Oyama, Oxygen-removal of dibenzofuran as a model compound in biomass derived bio-oil on nickel phosphide catalysts: Role of phosphorus, *Appl. Catal. B: Environ.* 136 (2013) 140-149.
- [48] J.A. Cecilia, A. Infantes-Molina, J. Sanmartin-Donoso, E. Rodriguez-Aguado, D. Ballesteros-Plata, E. Rodriguez-Castellon, Enhanced HDO activity of Ni₂P promoted with noble metals, *Catal. Sci. Technol.* 6 (2016) 7323-7333.
- [49] A. Cho, H. Kim, A. Iino, A. Takagaki, S.T. Oyama, Kinetic and FTIR studies of 2-methyltetrahydrofuran hydrodeoxygenation on Ni₂P/SiO₂, *J. Catal.* 318 (2014) 151-161.
- [50] P. Bui, A. Takagaki, R. Kikuchi, S.T. Oyama, Kinetic and Infrared Spectroscopy Study of Hydrodeoxygenation of 2-Methyltetrahydrofuran on a Nickel Phosphide Catalyst at Atmospheric Pressure, *ACS Catal.* 6 (2016) 7701-7709.
- [51] A. Iino, A. Cho, A. Takagaki, R. Kikuchi, S.T. Oyama, Kinetic studies of hydrodeoxygenation of 2-methyltetrahydrofuran on a Ni₂P/SiO₂ catalyst at medium pressure, *J. Catal.* 311 (2014) 17-27.
- [52] S. Boullousa-Eiras, R. Lodeng, H. Bergem, M. Stocker, L. Hannevold, E.A. Blekkana, Catalytic hydrodeoxygenation (HDO) of phenol over supported molybdenum carbide, nitride, phosphide and oxide catalysts, *Catal. Today* 223 (2014) 44-53.
- [53] K.Q. Yan, Y.H. Li, X. Zhang, X. Yang, N.W. Zhang, J.B. Zheng, B.H. Chen, K.J. Smith, Effect of preparation method on Ni₂P/SiO₂ catalytic activity for NaBH₄ methanolysis and phenol hydrodeoxygenation, *Int. J. Hydrogen Energy* 40 (2015) 16137-16146.

- [54] V.M.L. Whiffen, K.J. Smith, S.K. Straus, The influence of citric acid on the synthesis and activity of high surface area MoP for the hydrodeoxygenation of 4-methylphenol, *Appl. Catal. A: Gen.* 419 (2012) 111-125.
- [55] J.S. Moon, E.G. Kim, Y.K. Lee, Active sites of Ni₂P/SiO₂ catalyst for hydrodeoxygenation of guaiacol: A joint XAFS and DFT study, *J. Catal.* 311 (2014) 144-152.
- [56] M.B. Griffin, F.G. Baddour, S.E. Habas, D.A. Ruddy, J.A. Schaidle, Evaluation of Silica-Supported Metal and Metal Phosphide Nanoparticle Catalysts for the Hydrodeoxygenation of Guaiacol Under Ex Situ Catalytic Fast Pyrolysis Conditions, *Top. Catal.* 59 (2016) 124-137.
- [57] T.A. Le, H.V. Ly, J. Kim, S.S. Kim, J.H. Choi, H.C. Woo, M.R. Othman, Hydrodeoxygenation of 2-furyl methyl ketone as a model compound in bio-oil from pyrolysis of *Saccharina Japonica* Alga in fixed-bed reactor, *Chem. Eng. J.* 250 (2014) 157-163.
- [58] R. Zarchin, M. Rabaev, R. Vidruk-Nehemya, M.V. Landau, M. Herskowitz, Hydroprocessing of soybean oil on nickel-phosphide supported catalysts, *Fuel* 139 (2015) 684-691.
- [59] Q.X. Guan, F.F. Wan, F. Han, Z.H. Liu, W. Li, Hydrodeoxygenation of methyl palmitate over MCM-41 supported nickel phosphide catalysts, *Catal. Today* 259 (2016) 467-473.
- [60] N. Koike, S. Hosokai, A. Takagaki, S. Nishimura, R. Kikuchi, K. Ebitani, Y. Suzuki, S.T. Oyama, Upgrading of pyrolysis bio-oil using nickel phosphide catalysts, *J. Catal.* 333 (2016) 115-126.
- [61] K.L. Li, R.J. Wang, J.X. Chen, Hydrodeoxygenation of Anisole over Silica-Supported Ni₂P, MoP, and NiMoP Catalysts, *Energy Fuels* 25 (2011) 854-863.
- [62] P. Bui, J.A. Cecilia, S.T. Oyama, A. Takagaki, A. Infantes-Molina, H.Y. Zhao, D. Li, E. Rodriguez-Castellon, A.J. Lopez, Studies of the synthesis of transition metal phosphides and their activity in the hydrodeoxygenation of a biofuel model compound, *J. Catal.* 294 (2012) 184-198.
- [63] A. Cho, J. Shin, A. Takagaki, R. Kikuchi, S.T. Oyama, Ligand and Ensemble Effects in Bimetallic NiFe Phosphide Catalysts for the Hydrodeoxygenation of 2-Methyltetrahydrofuran, *Top. Catal.* 55 (2012) 969-980.

- [64] W.Y. Wang, K. Zhang, H. Liu, Z.Q. Qiao, Y.Q. Yang, K. Ren, Hydrodeoxygenation of p-cresol on unsupported Ni-P catalysts prepared by thermal decomposition method, *Catal. Commun.* 41 (2013) 41-46.
- [65] S.K. Wu, P.C. Lai, Y.C. Lin, H.P. Wan, H.T. Lee, Y.H. Chang, Atmospheric Hydrodeoxygenation of Guaiacol over Alumina-, Zirconia-, and Silica-Supported Nickel Phosphide Catalysts, *ACS Sustain. Chem. Eng.* 1 (2013) 349-358.
- [66] F. Han, Q.X. Guan, W. Li, Deoxygenation of methyl palmitate over SiO₂-supported nickel phosphide catalysts: effects of pressure and kinetic investigation, *Rsc Adv* 5 (2015) 107533-107539.
- [67] A. Cho, A. Takagaki, R. Kikuchi, S.T. Oyama, Active Sites in Ni₂P/USY Catalysts for the Hydrodeoxygenation of 2-Methyltetrahydrofuran, *Top. Catal.* 58 (2015) 219-231.
- [68] S.Y. Liu, Q.Q. Zhu, Q.X. Guan, L.N. He, W. Li, Bio-aviation fuel production from hydroprocessing castor oil promoted by the nickel-based bifunctional catalysts, *Bioresour. Technol.* 183 (2015) 93-100.
- [69] S.T. Oyama, T. Onkawa, A. Takagaki, R. Kikuchi, S. Hosokai, Y. Suzuki, K.K. Bando, Production of Phenol and Cresol from Guaiacol on Nickel Phosphide Catalysts Supported on Acidic Supports, *Top. Catal.* 58 (2015) 201-210.
- [70] H. Song, J. Gong, H.L. Song, F. Li, A novel surface modification approach for synthesizing supported nickel phosphide catalysts with high activity for hydrodeoxygenation of benzofuran, *Appl. Catal. A: Gen.* 505 (2015) 267-275.
- [71] Y.X. Yang, C. Ochoa-Hernandez, V.A.D. O'Shea, P. Pizarro, J.M. Coronado, D.P. Serrano, Transition Metal Phosphide Nanoparticles Supported on SBA-15 as Highly Selective Hydrodeoxygenation Catalysts for the Production of Advanced Biofuels, *J Nanosci Nanotechnol* 15 (2015) 6642-6650.
- [72] A. Berenguer, T.M. Sankaranarayanan, G. Gomez, I. Moreno, J.M. Coronado, P. Pizarro, D.P. Serrano, Evaluation of transition metal phosphides supported on ordered mesoporous materials as catalysts for phenol hydrodeoxygenation, *Green Chemistry* 18 (2016) 1938-1951.
- [73] M.Y. Lu, L.R. Zheng, R.G. Li, Q.X. Guan, W. Li, Efficient hydrogenation performance improvement of MoP and Ni₂P catalysts by adjusting the electron distribution around Mo and Ni atoms, *Rsc Adv* 6 (2016) 65081-65088.

- [74] M. Peroni, G. Mancino, E. Barath, O.Y. Gutierrez, J.A. Lercher, Bulk and gamma-Al₂O₃-supported Ni₂P and MoP for hydrodeoxygenation of palmitic acid, *Appl. Catal. B: Environ.* 180 (2016) 301-311.
- [75] D.J. Rensel, J. Kim, Y. Bonita, J.C. Hicks, Investigating the multifunctional nature of bimetallic FeMoP catalysts using dehydration and hydrogenolysis reactions, *Appl. Catal. A: Gen.* 524 (2016) 85-93.
- [76] H. Song, J. Gong, H.L. Song, F. Li, J. Zhang, Y.G. Chen, Preparation of core-shell structured Ni₂P/Al₂O₃@TiO₂ and its hydrodeoxygenation performance for benzofuran, *Catal. Commun.* 85 (2016) 1-4.
- [77] V.O.O. Goncalves, P.M. de Souza, V.T. da Silva, F.B. Noronha, F. Richard, Kinetics of the hydrodeoxygenation of cresol isomers over Ni₂P/SiO₂: Proposals of nature of deoxygenation active sites based on an experimental study, *Appl. Catal. B: Environ.* 205 (2017) 357-367.
- [78] G.N. Yun, A. Takagaki, R. Kikuchi, S.T. Oyama, Hydrodeoxygenation of gamma-valerolactone on transition metal phosphide catalysts, *Catal. Sci. Technol.* 7 (2017) 281-292.

Chapter 2

Hydrodeoxygenation of γ -Valerolactone on Transition Metal Phosphide Catalysts

2.1 Introduction

Biomass has been recently studied as an alternative feedstock for chemicals and fuels to overcome environmental problems resulting from excessive use of fossil fuels [1, 2]. Several technologies such as hydrothermal liquefaction of woody biomass [3, 4], pyrolysis upgrading of cedar chips and cellulose [5, 6] and aqueous phase catalytic transformation of sugars and polyols [7] have been developed for converting biomass into liquid fuels. Among them, fast pyrolysis gives high yields of liquids (pyrolysis bio-oil) of up to 75 wt.% at moderate temperatures of around 500 °C and short hot vapor residence times of around 1 s [8]. However the bio-oil cannot be directly used as a fuel because it has high oxygen content (35-40 wt.%) with 15-30 wt.% of water, which results in low heating value, immiscibility with hydrocarbon fuels, high acidity, and chemical and thermal instability [9, 10]. Therefore, the oxygen in the bio-oil needs to be removed to obtain a liquid fuel of required quality.

Catalytic hydrodeoxygenation (HDO) is one of the promising processes that aim at the production of useable liquid fuels by removal of oxygen in the presence of H₂ [11, 12]. Transition metal sulfide catalysts (CoMoS and NiMoS) have been widely tried as candidates due to their hydrogenation ability in commercial hydrodesulfurization (HDS) and hydrodenitrogenation (HDN) processes, which are closely related to HDO processes in the removal of a heteroatom with direct bonding to carbon. However, a major

problem of the sulfides is that they are deactivated in the absence of sulfur, which is not normally present in the bio-oil [13, 14]. Noble metals have also been tried as they are active in hydrogenation reactions at mild conditions [15, 16]. It has been found that Pd, Pt, Rh and Ru catalysts have high activity in the HDO of bio-oil model compounds such as dibenzofuran [17], phenol [18, 19], guaiacol [16, 20], and propanoic acid [21, 22]. However, their high cost and poor tolerance for sulfur and nitrogen are still problems [23, 24].

Recently, a number of studies of transition metal phosphide catalysts have reported that they are active for HDO processes [25, 26, 27] as well as HDS and HDN [28, 29]. In a previous study, the HDO activity for 2-methyl tetrahydrofuran (2-MTHF) was examined on a series of silica-supported transition metal phosphide catalysts and the activity order was found to be $\text{Ni}_2\text{P} > \text{WP} > \text{MoP} > \text{CoP} > \text{FeP} > \text{Pd}/\text{Al}_2\text{O}_3$ [30]. Furthermore, the Ni_2P phosphide catalyst showed higher activity for 2-MTHF HDO than $\text{Pd}/\text{Al}_2\text{O}_3$ at 300 °C and 1 atm. The catalytic performance of transition metal phosphide catalysts in the deoxygenation of methyl laurate was investigated, and the activity order followed the sequence: $\text{Ni}_2\text{P} > \text{MoP} > \text{CoP-Co}_2\text{P} > \text{WP} > \text{Fe}_2\text{P-FeP}$; $\text{Ni}_2\text{P} > \text{Ni}_{12}\text{P}_5 > \text{Ni}_3\text{P}$. Various factors, including surface metal site density, the electron density of metal sites and Brønsted acidity, give rise to the differences in catalytic activity [31].

The compound GVL is found in bio-oil, and indeed, it is a so-called platform chemical because it is formed in large amounts in the degradation of cellulose and has potential use as a liquid fuel, an intermediate for fine chemicals, and a solvent [32, 33]. Thus, many approaches aiming to upgrade GVL to valuable chemicals have been reported. The production of C12 jet fuel from GVL was proposed in a dual reactor

system involving the production of butene isomers via ring-opening and decarboxylation on $\text{SiO}_2/\text{Al}_2\text{O}_3$ at 36 bar H_2 with subsequent oligomerization of butene isomers on Amberlyst70. It was found that the yield of higher liquid alkenes reached 75% [34]. Similarly, the conversion of GVL to 5-nonanone, a precursor to hydrocarbon fuels, was reported in a double-bed arrangement of $\text{Pd}(5\%)/\text{Nb}_2\text{O}_5$ + ceria-zirconia in a single reactor. It was shown that $\text{Pd}(5\%)/\text{Nb}_2\text{O}_5$ is responsible for ring opening and ceria-zirconia for further hydrogenation and subsequent ketonization [35]. Also the formation of valerate esters from GVL was deemed to be promising since their energy density, polarity and volatility are compatible with either gasoline or diesel [36]. The transformation required a bifunctional catalyst and it was found that 64% ethyl valerate would be formed on $\text{Co}/\text{HZSM-5}$ [37].

In this work, a series of transition metal phosphide catalysts (Ni_2P , CoP , MoP , and WP) supported on MCM-41 is synthesized and characterized to investigate its activity in the HDO of GVL. This is the first time such a series has been prepared using the high surface area MCM-41 support, and the resulting materials are highly dispersed. The performance, including catalytic activity and product selectivity, are compared at various temperatures with those of a commercial $\text{Pd}/\text{Al}_2\text{O}_3$ catalyst, which has shown superior activity in HDO. Furthermore, based on the results of product selectivity, a possible reaction pathway for the HDO of GVL is proposed.

2.2 Experimental

2.2.1 Preparation of supported transition metal phosphide catalysts

A commercial MCM-41 support (Aldrich) was used as received. The supported catalysts were prepared by incipient wetness impregnation of aqueous metal phosphite precursors, followed by temperature-programmed reduction (TPR) under hydrogen flow. A mixed solution was made by adding a certain amount of a desired metal salt into a phosphorus-containing solution [38, 39]. The amount of metal was $1.0 \text{ mmol/g}_{\text{support}}$ and the initial ratio of metal/P was fixed at 1/2. The quantities of materials are summarized in Table 2.1. The mixed solution was used to impregnate the MCM-41 support by the incipient wetness technique. The obtained phosphite precursor was dried in air at $120 \text{ }^\circ\text{C}$ overnight, and then pelletized and sieved to a size of $650\text{-}1180 \text{ }\mu\text{m}$. The resulting precursor was reduced to the corresponding phosphides by TPR from room temperature to the reduction temperature at $3 \text{ }^\circ\text{C min}^{-1}$ in a quartz reactor under a hydrogen flow of $1000 \text{ cm}^3 \text{ min}^{-1} \text{ g}_{\text{catalyst}}^{-1}$. After reduction, the sample was cooled to room temperature under helium flow and then was passivated under $0.2 \text{ \% O}_2/\text{He}$ flow ($100 \text{ cm}^3 \text{ min}^{-1}$) for 4h to prevent uncontrolled oxidation. For comparison a 5 wt. % Pd/Al₂O₃ commercial catalyst supplied by BASF Catalysts, Inc. was used.

Table 2.1. Quantities of materials used in catalyst preparation

Sample	Metal source /mmol		Metal phosphide /wt. %
PO _x /MCM-41	-		-
Ni ₂ P/MCM-41	Ni(OH) ₂	5.0	6.9
CoP/MCM-41	Co(OH) ₂	5.0	8.2
MoP/MCM-41	(NH ₄) ₆ Mo ₇ O ₂₄ ·4H ₂ O	0.7	11
WP/MCM-41	(NH ₄) ₆ W ₁₂ O ₃ ·9H ₂ O	0.4	18

Metal loading level: $1.0 \text{ mmol}_{\text{metal}} \text{ g}_{\text{support}}^{-1}$

MCM-41: 5 g

H₃PO₃: 0.828 g (10 mmol)

2.2.2 Characterization of prepared catalyst samples

The temperature-programmed reduction (TPR) method was used to determine the reduction characteristics of the material. First, 0.1 g of sample was loaded in a quartz reactor and then pretreated at 120 °C under helium flow. After that, it was heated from 50 to 800 °C under H₂ flow of 100 cm³ min⁻¹ while the effluent was monitored by a quadruple mass spectrometer. Chemisorption uptakes of CO were measured on a sample re-reduced in a H₂ flow at 550 °C for 3 h. Pulses of CO were passed at 50 °C over the sample to measure the total dynamic gas uptake. A BELSORP mini II micropore size analyzer was used to measure the specific surface area of the samples using N₂ adsorption at 77 K from the linear portion of BET plots ($P/P_0 = 0.01 - 0.20$). Before the measurements, the samples were degassed at 120 °C overnight to remove the adsorbed species from the sample. X-Ray diffraction (XRD) patterns of fresh and spent samples were measured on a diffractometer (Rigaku RINT 2400) operated at 40 kV and 100 mA, using a Cu-K α monochromatic x-ray source. Data were collected over a Bragg angle (2θ) range of 20-80° with a step size of 0.02°. X-ray absorption fine-structure (XAFS) spectra at the Ni K-edge (8.333keV) were recorded at beam line 9C (BL9C) of the Photon Factory in the Institute of Materials Structure Science, High-Energy Accelerator Research Organization (KEK-IMSS-PF). The X-ray ring was operated at 2.5 GeV with a beam current of 450 mA. The XAFS spectra were taken in transmission mode using ionization chambers for the detection of the incident X-ray beam (I_0 , 100% N₂) and transmitted beam (I_T , 25 % Ar in N₂). The passivated disk sample with 40 mg was placed in the center of an in situ cell equipped with Kapton windows, and reduced at 550 °C for 2 h under H₂ flow in the same manner as for the activity tests. The EXAFS data were analyzed by Winxas3.1. Phase shift and amplitude functions of Ni₂P were

calculated by FEFF8. Curve fitting was carried out using the three dominant shells (2 Ni-P at 0.226 nm, 4 Ni-P at 0.2457 nm, 4 Ni-Ni at 0.2678 nm) and the reducing factor (S_0^2) was fixed at 0.9, which was obtained from the Ni-Ni contribution of a Ni foil.

2.2.3 Activity test for HDO of GVL

The catalytic tests of HDO for GVL were carried out in a continuous-flow reactor operated at 0.5MPa and a temperature range of 250-350 °C. Quantities of catalyst corresponding to 10 μmol of sites as titrated by CO chemisorption were used. The catalyst was loaded in a section about 2 cm long in the middle of the reactor with quartz sand of the same particle size to disperse the catalyst. Before injecting the liquid feed, the phosphide catalyst was pretreated under a H_2 flow of $100 \text{ cm}^3 \text{ min}^{-1} \text{ g}_{\text{catalyst}}^{-1}$ at 550 °C for 4 h. The reactant was introduced into the reactor with a liquid pump. A mixture of 98 wt. % of GVL and 2 wt. % of toluene as an internal standard was vaporized at 300 °C and mixed with a H_2 gas stream to give a reactant stream of 2 mol% GVL in H_2 . The total pressure was fixed at 0.5 MPa using a back-pressure regulator. For stabilization, the catalysts were first maintained at 350 °C and 0.5 MPa for 12 h after introducing the reactant and then the temperature was varied downward and upward in the order: 350, 300, 250, 275, and 325 °C with each temperature maintained for 2 or 3 h. An on-line gas chromatograph (Shimadzu GC-14A, DB-624 UI, 60 m x 0.25 mm x 1.40 μm) equipped with a flame ionization detector (FID) and a thermal conductivity detector (TCD) was used for analyzing the products at 1 h intervals. In order to maintain product in the gas phase, all of the lines were heated to 250 °C with ribbon heaters. Qualitative analysis of unknown products was carried out by gas chromatography-mass spectrometry (Shimadzu GCMS-QP2010 Ultra) by injecting the gas products which

were collected from the outlet gas stream. A similar procedure was applied for a stability test of Ni₂P/MCM-41. After reaction, all the catalysts were treated under N₂ flow for 2 h and then collected for characterizations by XRD, CO chemisorption and N₂ physisorption.

The conversion of GVL, deoxygenation degree, product distribution and selectivity were calculated by the following equations:

$$GVL \text{ conversion} = \left(1 - \frac{n_{GVL,e}}{n_{GVL,f}} \right) \times 100\%$$

$$Deoxygenation \text{ degree} = \left(\frac{n_{hydrocarbons,p}}{n_{GVL,p}} \right) \times 100\%$$

$$Product \text{ distribution}, P_i = \left(\frac{carbon \ number \times n_i}{sum \ of \ carbon \ number \times n_i} \right)$$

$$Selectivity, S_i = \left(\frac{n_i}{\sum n_i} \right)$$

Where $n_{GVL,f}$ and $n_{GVL,e}$ describe the moles of GVL in the feed and exit, respectively, and n_i is the moles of product i. The deoxygenation degree shows how much GVL is converted into hydrocarbons such as butane, n-butenes, pentane, n-pentenes, and n-pentadienes.

2.3 Results and discussion

2.3.1 Characterizations of the prepared catalysts

Table 2.2. Characterization of fresh and spent catalysts

Sample	Condition	CO uptake ^b / $\mu\text{mol g}^{-1}$	Reduction temperature / $^{\circ}\text{C}$	BET surface area / $\text{m}^2 \text{g}^{-1}$
MCM-41	As received	-	-	997
Ni ₂ P/MCM-41	fresh	70	570	663
	spent ^a	67	-	651
CoP/MCM-41	fresh	59	705	582
	spent ^a	55	-	578
MoP/MCM-41	fresh	74	597	539
	spent ^a	71	-	521
WP/MCM-41	fresh	30	610	509
	spent ^a	27	-	499
Pd/Al ₂ O ₃	As received	80	-	82

^a After activity test at 250 – 350 °C and 0.5 MPa for 24 h

^b After in situ reduction at 550 °C for 2 h

Table 2.2 shows the reduction temperatures, surface areas and CO-uptakes of the fresh and spent catalysts. The reduction temperature will be discussed in the following paragraph. The surface areas of the fresh catalysts ranged from 500 to 663 m² g⁻¹. After loading the metal, all the samples presented a decrease of surface area due to a reduction of pore volume due to the presence of metal phosphide and excess phosphorous on the support. The spent catalysts exhibited a similar surface area with the fresh catalysts. The CO uptakes for fresh catalysts were between 30 and 74 $\mu\text{mol/g}$ and, for the spent catalysts did not change significantly. These results indicated that the structure of catalysts was maintained during reaction. The amounts of catalyst loaded in the reactor for catalytic testing corresponded to 10 μmol of sites, counted by CO adsorption.

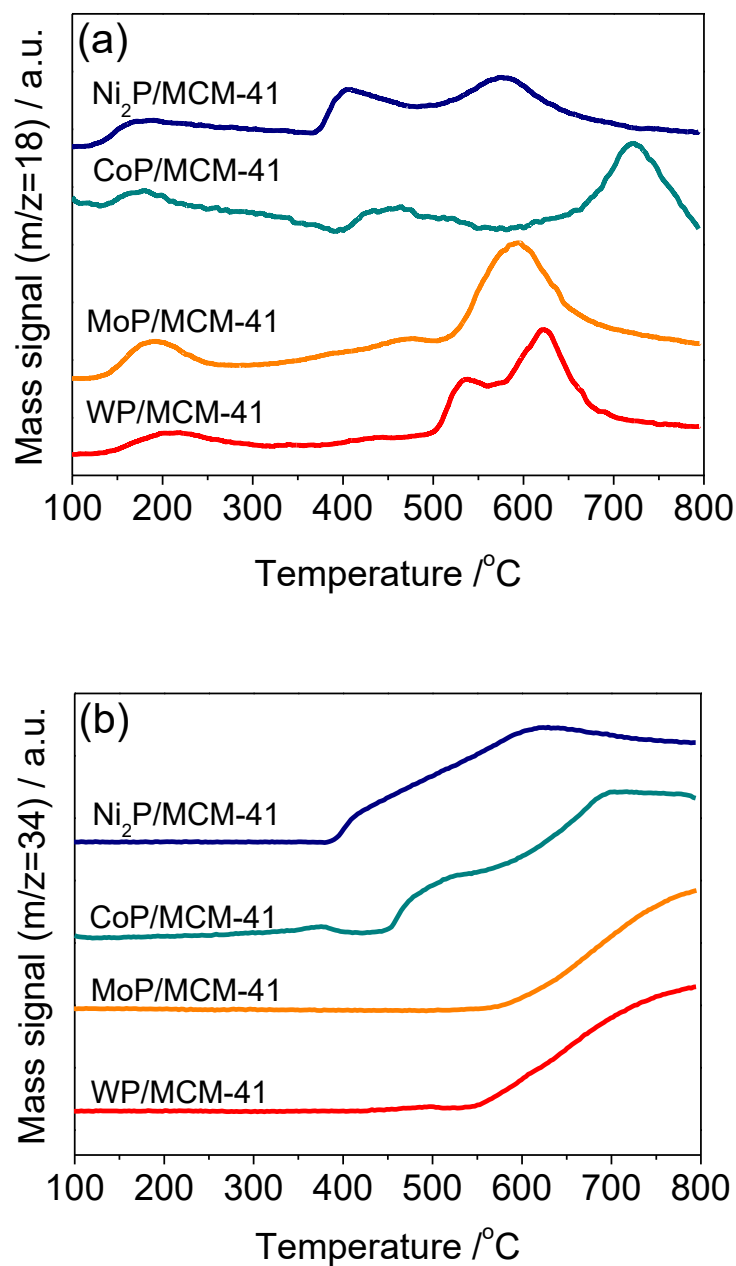


Figure 2.1. TPR profiles for the precursors of phosphide catalysts (a) Mass 18 signal and (b) Mass 34 signal

Fig. 2.1 shows the TPR profiles of the precursors of the Ni₂P/MCM-41, CoP/MCM-41, MoP/MCM-41, and WP/MCM-41 catalysts. The H₂O signal (m/z = 18) shown in Fig.2-1(a) displays broad features between 150-210 °C due to desorption of

strongly held water and dehydroxylation, and distinct features above 400 °C for reduction of the phosphite [30]. The maximum peak temperature was chosen as the reduction temperature for large scale syntheses. The Ni₂P catalyst precursor gave two main peaks at 400 and 570 °C to different stages in the reduction of Ni phosphite to Ni phosphide. In a previous study [40], it was suggested that the peak at lower temperatures (375-450 °C) is related to the formation of the Ni₂P phase by the reaction between PH₃ and metallic nickel, and the higher temperature peak (> 400 °C) is related to the reduction of HPO₃H⁻ and nickel ions that interact strongly with the support. The CoP precursor showed peaks at 450 °C and 705 °C also corresponding to different steps in the reduction. It was reported that formation of CoP occurred sequentially, where one of the intermediates was Co₂P which reacts with PH₃ to subsequently form CoP [39]. The MoP catalyst presented a broad unresolved reduction peak at around 597 °C while the WP precursor showed a small peak at 530 °C and a major peak at 610 °C indicating that the stages for these group 6 metals occurred close to each other. The PH₃ signal shown in Fig. 2.1 (b) shows similar features as the H₂O signal, indicating that both H₂O and PH₃ were formed simultaneously in the same reduction process. The PH₃ signal was broader and occurred at higher temperature for the Mo and W samples indicating that metal reduction occurred before phosphite reduction. After reduction, phosphine kept being produced because of the use of excess phosphorous in the preparation method. All the trends are consistent with previous results, but in all cases the reduction temperatures are slightly higher than in the previous study with a silica support [30]. This is because the present study uses a high surface area support, MCM-41, which enhances the dispersion of the metal precursors and leads to stronger interactions with the support so that the reduction temperatures are increased [41, 42].

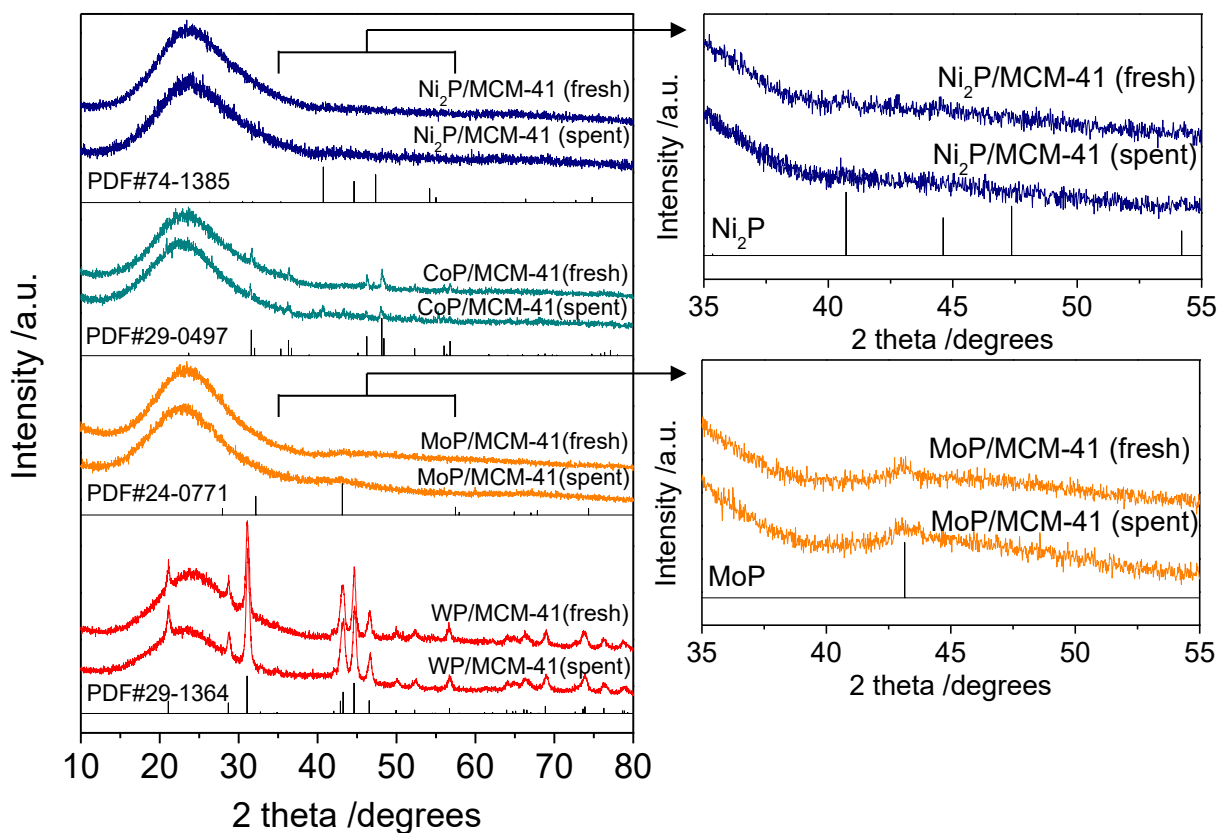


Figure 2.2. XRD profiles for fresh and spent catalysts

Fig. 2.2 shows the powder XRD patterns for the fresh and spent catalysts. The broad line centered at $2\theta = 23^\circ$ is typical for amorphous silica, which is observed in all catalysts. The $\text{Ni}_2\text{P}/\text{MCM-41}$ shows broad peaks at $2\theta = 40.7^\circ$, 44.6° , 47.4° , and 54.2° (PDF#74-1385) due to highly dispersed Ni_2P particles on the MCM-41. The $\text{CoP}/\text{MCM-41}$ shows three main peaks at $2\theta = 31.6^\circ$, 46.2° , and 48.1° (PDF#29-0497), corresponding to the characteristic XRD peaks of the CoP reference. The MoP presents a broad peak at $2\theta = 43.1^\circ$ (PDF#24-0771), indicating low crystallinity and small particle size. The $\text{WP}/\text{MCM-41}$ displays strong sharp peaks at $2\theta = 31.1^\circ$, 43.2° , 44.6° ,

and 46.5° (PDF#29-1364), which are well matched with the WP reference. After reaction, the XRD patterns of the all samples show a partial decrease of intensity, but the peaks of the phosphide phases are still visible indicating that the catalysts are stable at these reaction conditions. The crystallite size of Ni_2P is below the detection limit for XRD (roughly 3 nm), so EXAFS measurements were adopted to confirm the presence of the Ni_2P phase under reduction condition (H_2 flow and 550°C). Fig. 2.3 (a) and (b) show the Ni K-edge EXAFS spectra for reduced $\text{Ni}_2\text{P}/\text{MCM-41}$ sample. Although the experimental curve is not well resolved, there are two main peaks in the Fourier transforms located at 0.180 nm and 0.228 nm, corresponding to Ni-P and Ni-Ni, respectively [43]. A three-shell curve-fitting analysis of the Fourier transform spectra was conducted as shown in Table 3 [44]. The distances for Ni-P(I), Ni-P(II), and Ni-Ni bonds were 0.2207, 0.2344, and 0.2551 nm, respectively, and corresponding coordination numbers were 1.8, 2.8, 2.0. These values were similar with previous results showed that smaller Ni_2P crystallites have larger coordination numbers in the Ni-P(II) and lower coordination number in the Ni-Ni [27]. This indicates that Ni_2P phase is present on the MCM-41 support.

Table 2.3. Curve-fitting result for $\text{Ni}_2\text{P}/\text{MCM-41}$

	Ni-P(I)	Ni-P(II)	Ni-Ni	R-factor /%
CN	2	4	4	
R /nm	0.227	0.246	0.268	
$\text{Ni}_2\text{P}/\text{MCM-41}$				
CN	1.822	2.844	2.048	1.4
R /nm	0.221	0.234	0.255	
$\sigma^2 / 10^{-5}\text{nm}^2$	0.975	2.334	1.351	
$\Delta E / \text{eV}$	-8.119	5.486	-1.669	

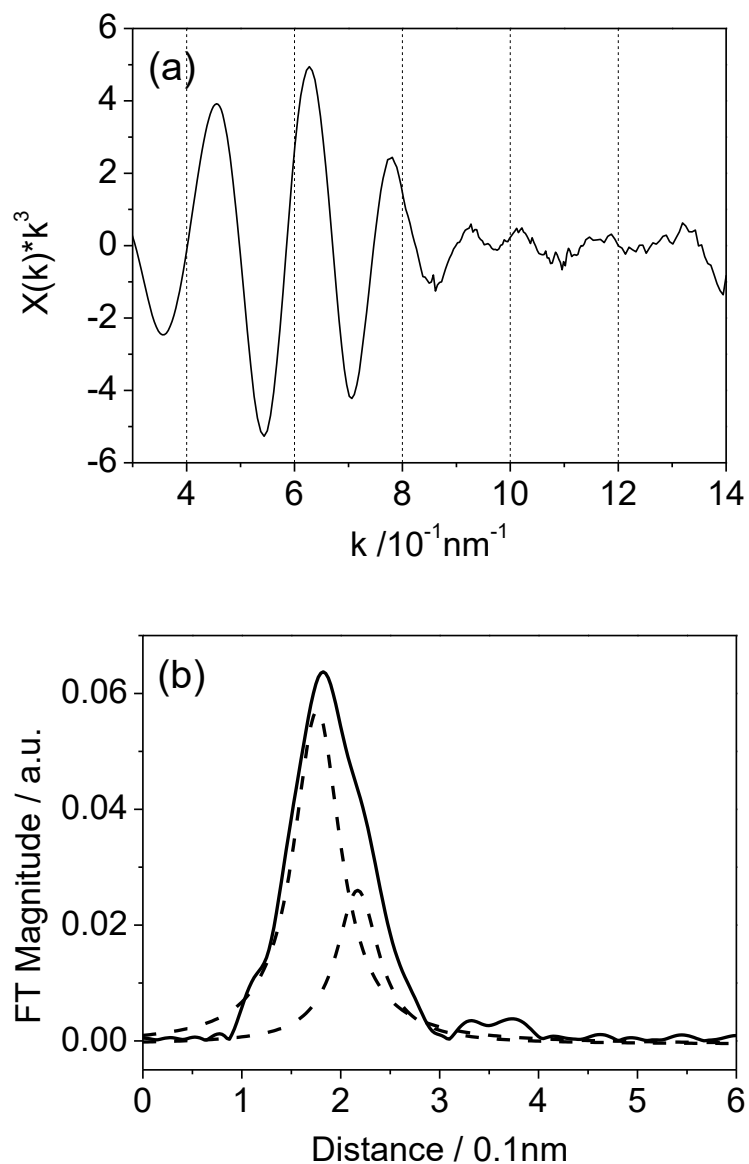


Figure 2.3. Ni K-edge (a) EXAFS spectra and (b) Fourier transform of Ni₂P/MCM-41

2.3.2 Catalyst stability test

Fig. 2.4 shows GVL conversion and product distributions over Ni₂P/MCM-41 as a function of time on stream. A stability test was conducted at 300 °C and 0.5 MPa with 4% GVL in H₂ for 50 h on stream. The main products were pentanoic acid (39 %), 2-MTHF (0.7 %), 1-pentanol (0.4 %), pentanal (0.2 %), 2-pentanone (0.2 %), pentane

(1 %), butane (40 %), n-butene (5 %), and CO (10 %). The conversion slightly decreased from 61% to 55 % and then stabilized after 20 h, while the product distributions were not significantly changed. This result indicated that the Ni₂P/MCM-41 catalyst was stable at the applied reaction conditions.

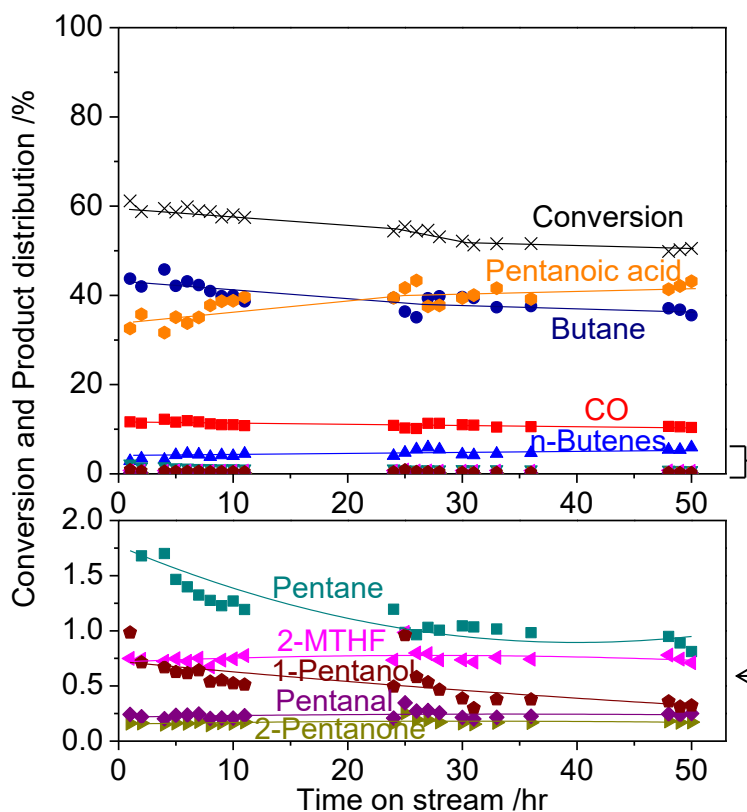


Figure 2.4. GVL conversion and product distributions over Ni₂P/MCM-41 as a function of time on stream at 300 oC and 0.5 MPa with 4% GVL in H₂

2.3.3 Reactivity as a function of temperature over transition metal phosphide catalysts

Fig. 2.5 shows the GVL conversion, deoxygenation degree and turnover frequency (TOF) at 0.5 MPa as a function of temperature on Ni₂P/MCM-41, CoP/MCM-41, MoP/MCM-41, WP/MCM-41, Pd/Al₂O₃, PO_x/MCM-41 and MCM-41. The TOF tracks the conversion because amount of catalysts corresponding to equal quantities of sites were used in the measurements. The GVL conversion gives

information about the amount of GVL that is converted into products, including both hydrocarbons and oxygen-containing compounds, while deoxygenation degree (Deox) indicates how much GVL is transformed into hydrocarbons. Comparison of GVL conversion and deoxygenation degree clarifies the type of reaction that occurs. In all cases, GVL conversion was higher than the deoxygenation degree because some products were oxygenates. In addition to the catalyst activity tests, blank tests were conducted with the support and phosphorous-loaded support. In the catalyst preparation, excess phosphorous was used so that some phosphorous likely was retained on the support, even though some was volatilized. Amounts of 1.0 g of PO_x/MCM-41 and MCM-41 were evaluated at 0.5 MPa at various temperatures (250-350 °C). The MCM-41 exhibited a low activity for both GVL conversion (0.15 %) and deoxygenation degree (0.1 %) even at 350 °C. The PO_x/MCM-41 displayed a higher GVL conversion (6.9 %) and deoxygenation degree (1.6 %) at 350 °C, but these were still low. Therefore, the effects of support and phosphorous were negligible in the removal of oxygen at the conditions of study. Amounts of 0.14 g of Ni₂P/MCM-41, 0.17 g of CoP/MCM-41, 0.14 g of MoP/MCM-41, 0.33 g of WP/MCM-41 and 0.13 g of Pd/Al₂O₃ catalysts corresponding to 10 μmol of CO uptake sites were loaded and tested at a constant reactant flowrate of 1.6 μmols⁻¹. Thus the temperature variation results are considered to give the intrinsic catalytic activity of the catalysts. All samples had higher conversion and deoxygenation degree at higher temperatures as expected. At all temperatures, the GVL conversion and deoxygenation degree followed the same order: Ni₂P/MCM-41 >> CoP/MCM-41 >> Pd/Al₂O₃ ≈ MoP/MCM-41 > WP/MCM-41, indicating that the catalytic activity of the phosphide catalysts was higher or close to that of Pd/Al₂O₃. In particular, Ni₂P/MCM-41 presented remarkable activity attaining full conversion and

deoxygenation degree at 350 °C, while MoP/MCM-41 and WP/MCM-41 were considerably less active, especially in the removal of oxygen. Interestingly, it was found that the iron group phosphides (Ni₂P, CoP) were more active than the group 6 metal phosphides (MoP, WP). This might be related to the nature of the metal in phosphide catalysts, especially its electron density. In previous work on deoxygenation of methyl laurate over transition metal phosphides, it was suggested that Ni, Co and Fe sites have higher electron density than Mo and W sites and so can favorably protonate O compounds, which leads to enhanced conversion [31]. The right scale of Fig. 2.5 shows the turnover frequency (TOF) for the GVL reaction and the deoxygenation degree as a function of temperature on the transition metal phosphide catalysts and the commercial Pd/Al₂O₃ catalyst. The TOF value was calculated by the following equation:

$$TOF(s^{-1}) = \frac{\text{Conversion} \times \text{Flow rate of GVL} (\mu\text{mol s}^{-1})}{\text{Catalyst weight}(g) \times \text{Quantity of CO uptake site} (\mu\text{mol}/g)}$$

With equal number of sites the TOF is proportionated to conversion so the same curve applies with a different scale. The Ni₂P/MCM-41 showed the highest activity with a TOF of 0.17 s⁻¹ at 300 °C. In Ni₂P/MCM-41, the conversion and TOF curves maintained at in the temperature range of 325-350 °C. This was due to mass transfer limitations in the high conversion region (> 70 %). The Weisz-Prater criterion C_{WP} is a method used to determine that internal diffusion is limiting the reaction. This value was calculated by the following equation [45, 46]:

$$C_{WP} = \frac{\text{Actual reaction rate}}{\text{A diffusion rate}} = \frac{-r'_{A(obs)} \rho_c R^2}{D_e C_{As}}$$

Internal mass transfer effects can be neglected if the value of C_{WP} is less than 0.3 [47]. The parameters used for the criterion are summarized in Table 4.1. The observed rates $-r'_{A(obs)}$ and the calculated C_{WP} values are listed in Table 4.2. The values of C_{WP} are less than 0.3 except for the Ni₂P/MCM-41 sample at over 300 °C and the CoP/MCM-41 sample at 350 °C, which are exactly as expected from the shapes of the conversion curves, with mass transfer becoming important past the inflexion points in the curves. For the other samples, there are no diffusion limitations at all the reaction conditions. Also the Mears criterion for external diffusion was below 0.15 (see Supplementary Information) $\frac{-r'_a \rho_b R n}{k_c C_{Ab}} < 0.15$ indicating that mass transfer from the bulk gas phase to the catalyst surface can be neglected [45,48].

Table 2.4.1. Parameters in the Weisz-Prater Criterion

R	Catalyst particle radius / cm	0.09
$\rho_c(\text{Ni}_2\text{P,CoP, Pd})$	Solid catalyst density / $\text{g}\cdot\text{cm}^{-3}$	0.3
$\rho_c(\text{MoP, WP})$	Solid catalyst density / $\text{g}\cdot\text{cm}^{-3}$	0.4
$C_{As}(300\text{ }^\circ\text{C})$	Gas concentration at the catalyst surface / $\text{mol}\cdot\text{cm}^{-3}$	4.11E-07
D_e	Effective diffusivity/ $\text{cm}^2\cdot\text{s}^{-1}$	0.1

Table 2.4.2. Observed reaction rates and calculated Weisz-Prater criterion

	Ni ₂ P	CoP	MoP	WP	Pd
Temperature /°C	Observed reaction rate / $\text{molg}^{-1}\text{s}^{-1}$				
250	2.06E-06	3.98E-07	3.43E-07	3.15E-08	4.72E-07
275	4.58E-06	9.13E-07	4.60E-07	7.02E-08	7.04E-07
300	8.80E-06	2.08E-06	8.40E-07	1.53E-07	1.14E-06
325	1.12E-05	3.92E-06	1.44E-06	3.00E-07	1.99E-06
350	1.14E-05	6.73E-06	2.58E-06	5.64E-07	3.07E-06
Temperature /°C	Weisz-Prater criterion				
250	0.12	0.02	0.03	0.00	0.03
275	0.27	0.05	0.04	0.01	0.04
300	0.52	0.12	0.07	0.01	0.07
325	0.66	0.23	0.11	0.02	0.12
350	0.68	0.40	0.20	0.04	0.18

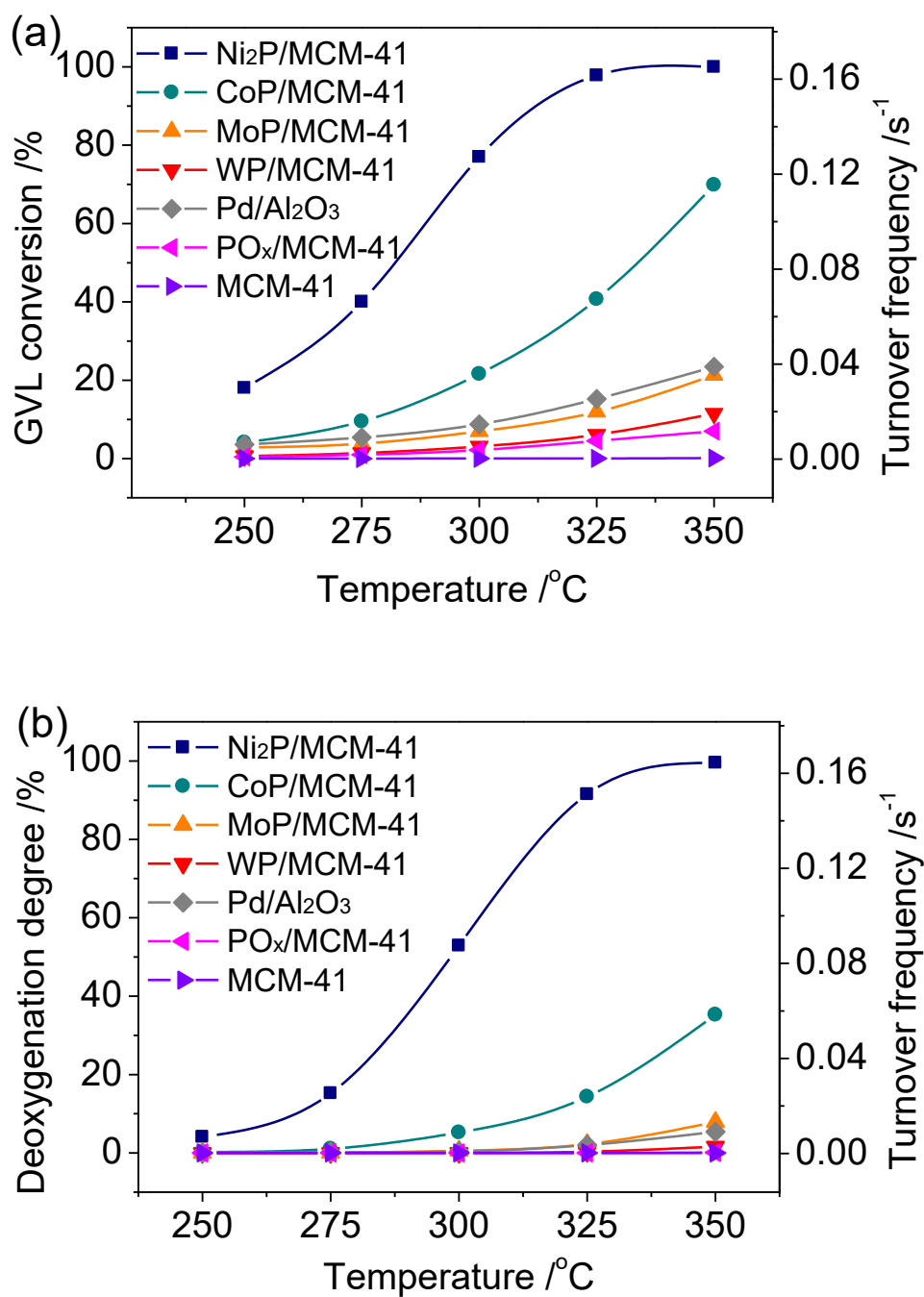


Figure 2.5. GVL conversion (a), deoxygenation degree (b) and turnover frequency (right scale) as a function of temperature at 0.5 MPa

Table 2.5. GVL conversion, deoxygenation degree, product distribution and carbon balance at 250 °C and 350 °C at 0.5 MPa

Temp. /°C	Sample	Conv. /%	DEOX /%	TOF /s ⁻¹	Product distribution /%					CB ^a /%
					CO	C4	C5	C5O	C5-O2	
250	Ni ₂ P/MCM-41	18.0	4.1	0.030	3.7	17.5	1.0	3.9	73.3	103
	CoP/MCM-41	4.1	0.2	0.007	0.9	4.3	0.5	8.3	85.9	99
	MoP/MCM-41	1.2	0.0	0.002	0.0	0.0	0.0	2.4	97.6	99
	WP/MCM-41	0.6	0.0	0.001	0.0	0.0	0.0	0.0	100	101
	Pd/Al ₂ O ₃	3.6	0.04	0.006	0.2	0.9	0.0	19.9	79.1	97
350	Ni ₂ P/MCM-41	100	99.5	0.166	16.8	81.3	1.4	0.3	0.1	101
	CoP/MCM-41	69.9	35.8	0.115	8.2	40.7	0.9	2.0	47.4	98
	MoP/MCM-41	21.3	7.9	0.036	3.0	14.1	19.5	17.2	46.1	97
	WP/MCM-41	11.6	1.6	0.019	1.3	5.9	6.6	6.4	79.8	103
	Pd/Al ₂ O ₃	23.5	5.4	0.039	3.7	18.1	0.6	1.6	75.7	96

^a Carbon balance (CB) calculated by $\left(\frac{\sum(\text{carbon number} \times n_{\text{product}})}{5 \times n_{\text{GVL}}}\right)$

The GVL conversion, deoxygenation degree, product distribution and carbon balance at 250 and 350 °C are summarized in Table 5. The products were classified into five groups: C4 (n-butenes, butane), C5 (n-pentadienes, n-pentenenes, pentane), C5-O (2-methyltetrahydrofutan, pentanal, 1-pentanol, 2-pentanone), C5-O2 (pentanoic acid, n-pentenoic acids), and finally CO. At 250 °C, the GVL conversion was below 5 % except for Ni₂P/MCM-41 and followed the order Ni₂P/MCM-41 (18 %) > CoP/MCM-41 (4.1 %) > Pd/Al₂O₃ (3.6 %) > MoP/MCM-41 (1.2 %) > WP/MCM-41 (0.6 %). This order was the same as that of the deoxygenation degree, although deoxygenation was 0 % for MoP/MCM-41 and WP/MCM-41 because no hydrocarbons were produced. At 250 °C, the main product was C5-O2 on all catalysts. At 350 °C, on the other hand, a different product distribution was observed. Among the hydrocarbons, the main product was C4 hydrocarbons on Ni₂P/MCM-41, CoP/MCM-41 and Pd/Al₂O₃ and C5 hydrocarbons on MoP/MCM-41 and WP/MCM-41, indicating that cleavage of C-C

bonds was favored on iron group phosphides and Pd/Al₂O₃. On Pd/Al₂O₃, a small amount of propane was produced by a cracking reaction, but its selectivity was below 0.5 %, so it was excluded from the calculation of the product distribution. The carbon balance was within the error range (100 % ± 5 %) on all catalysts at 250 °C and 350 °C, indicating that carbon deposition on the applied catalysts or polymerization didn't occur significantly.

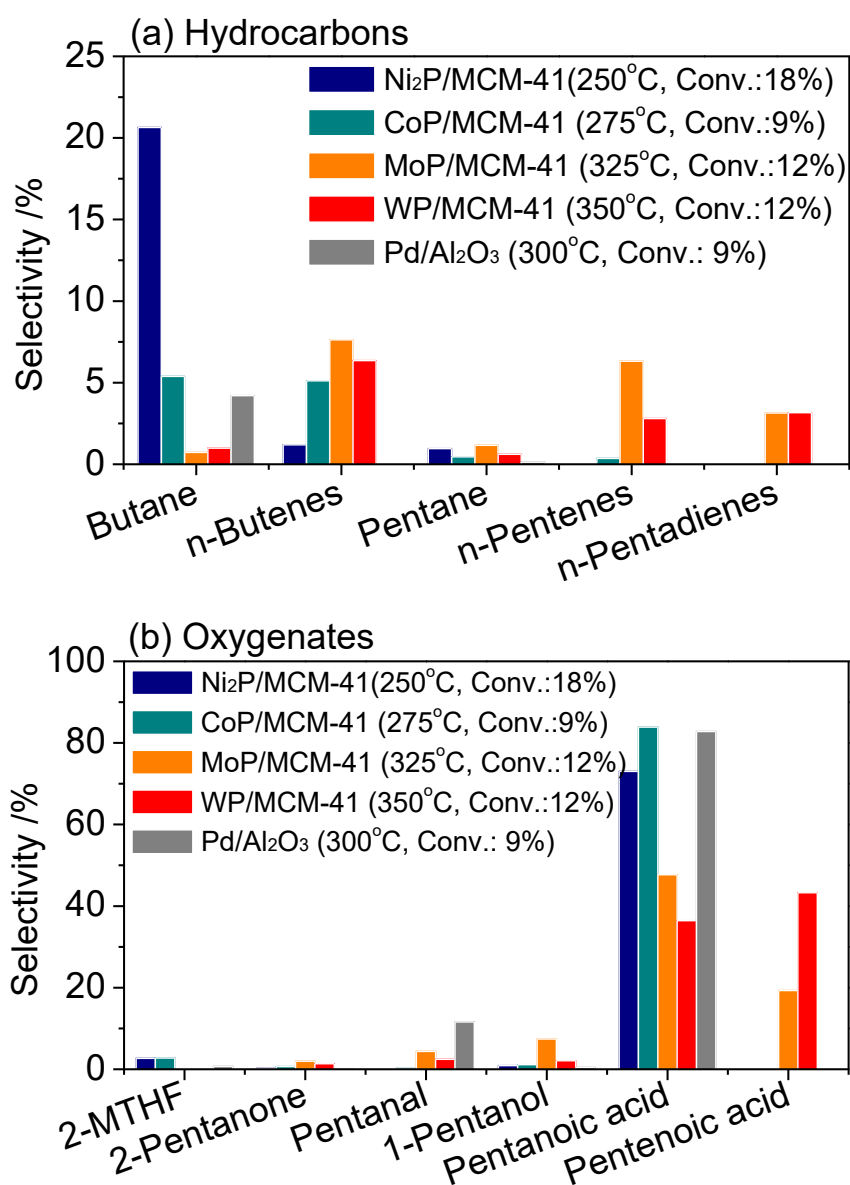


Figure 2.6. Product selectivity for HDO of GVL at around 10 % of GVL conversion

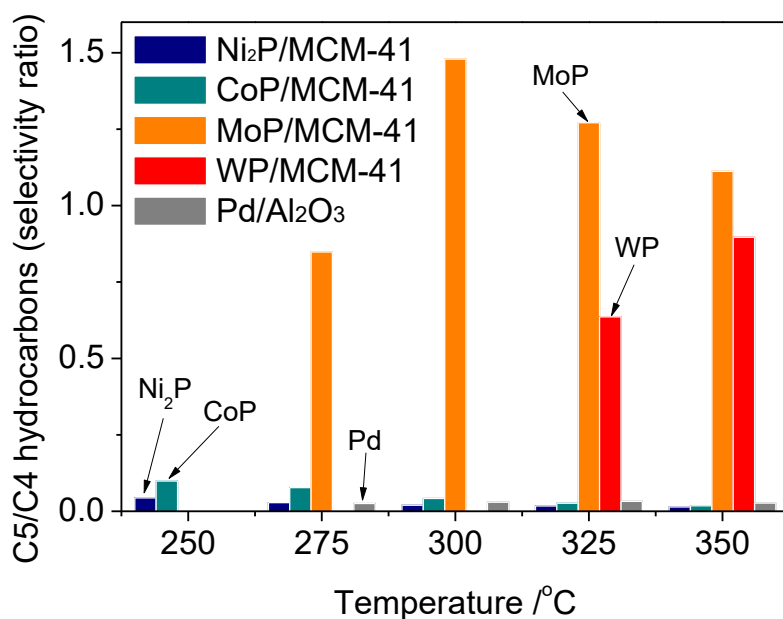


Figure 2.7. C5/C4 hydrocarbons (selectivity ratio) as a function of temperature

Fig. 2.6 shows the product selectivity at around 10 % of GVL conversion (18% at 250 °C on Ni₂P/MCM-41, 9 % at 275 °C on CoP/MCM-41, 12 % at 325 °C on MoP/MCM-41, 12 % at 350 °C on WP/MCM-41, 9 % at 300 °C on Pd/Al₂O₃). The products were categorized into two groups: hydrocarbons (butane, n-butenes, pentane, n-pentenes and n-pentadienes) and oxygenates (2-MTHF, 2-pentanone, pentanal, 1-pentanol, pentanoic acid and pentenoic acid). All phosphides had a strong preference for either pentanoic acid or n-pentenoic acids among the oxygenates, which were produced via ring opening from GVL. The Ni₂P/MCM-41, CoP/MCM-41 and Pd/Al₂O₃ catalysts followed a similar trend with a high affinity for the production of butane and pentanoic acid. The main products on Ni₂P/MCM-41 were butane (21 %), pentanoic acid (73 %), with very little n-butenes (1 %), pentane (1 %) and 2-MTHF (3 %) while CoP produced more alkenes and less alkanes. Furthermore, Pd/Al₂O₃ produced mainly butane (4 %) and very little pentane (0.1 %) among the hydrocarbon products. Unlike the iron group

phosphides, MoP/MCM-41 and WP/MCM-41 gave more C5 hydrocarbons in the hydrocarbon products, especially MoP/MCM-41. The main products on MoP/MCM-41 were n-butenes (8 %), n-pentenes (6 %), n-pentadienes (3 %), pentanoic acid (47 %) and pentenoic acid (19 %), while WP/MCM-41 gave less C5 hydrocarbons and more pentenoic acid (43 %). To summarize, the major differences in selectivity to hydrocarbons was that the iron-group catalysts (Ni₂P/MCM-41 and CoP/MCM-41) and Pd/Al₂O₃ produced mainly C4 hydrocarbons, while group 6 phosphides catalysts (MoP/MCM-41 and WP/MCM-41) formed more unsaturated C5 hydrocarbons such as n-pentenes and n-pentadienes. This is also shown in Fig. 2.7 which shows the C5/C4 hydrocarbon ratio based on the product selectivity at various temperatures. For the metal phosphides, the Mo and W sites may prefer to adsorb the O atom of the C=O group than the Ni and Co sites because of their larger electrophilicity, thus the C=O group was more easily hydrogenated to produce the C5 hydrocarbons [31]. Considering the energy content of the produced oil, the desired products are saturated hydrocarbon such as butane and pentane. Butane represents an undesired carbon loss, but this is offset by a decrease in required hydrogen amounts and the production of the reductant CO. This indicates that Ni₂P/MCM-41 and CoP/MCM-41 catalysts present a noteworthy activity in terms of GVL conversion and deoxygenation degree to produce butane. Table 2.6 shows the mole ratio (C₄H₁₀+C₄H₈)/CO at different temperatures for Ni₂P/MCM-41, CoP/MCM-41 and Pd/Al₂O₃. As can be seen, the ratio is slightly above 1. This indicates that decarbonylation is a main side reaction that forms butane or n-butenes. The value of the ratio above 1 indicates that some decarboxylation could also be occurring, but this should be minor compared to decarbonylation, and very little CO₂ was observed. A possible scheme is shown in Fig. 2.11.

Table 2.6. Mole ratio (C₄H₁₀+C₄H₈)/CO at different temperatures for Ni₂P/MCM-41, CoP/MCM-41 and Pd/Al₂O₃

Temperature /°C	Mole ratio (C ₄ H ₁₀ +C ₄ H ₈)/CO		
	Ni ₂ P/MCM-41	CoP/MCM-41	Pd/Al ₂ O ₃
250	1.18	-	-
275	1.12	-	-
300	1.09	1.09	-
325	1.02	1.23	1.08
350	1.21	1.24	1.22

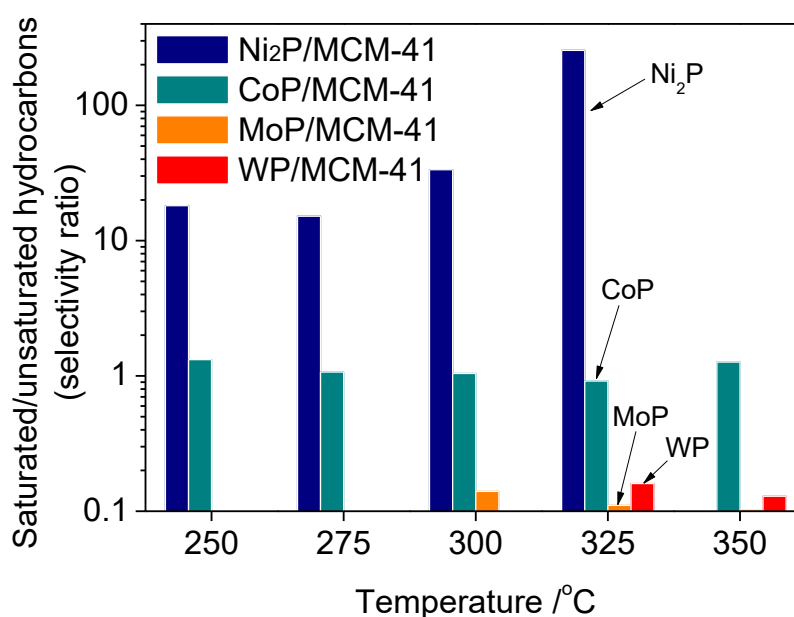


Figure 2.8. Saturated/unsaturated hydrocarbons (selectivity ratio) as a function of temperature at 0.5 MPa

Fig. 2.8 presents the saturated hydrocarbons/unsaturated hydrocarbons selectivity ratio as a function of temperature on the prepared catalysts. The saturated hydrocarbons include the alkanes such as butane and pentane and the unsaturated hydrocarbons include n-alkenes such as 1-butene, cis-2-butene, trans-2-butene, 1-pentene, cis-2-pentene, trans-2-pentene and 1.3-pentadiene. Thus, this ratio indicates the hydrogenation ability of the catalysts. On Pd/Al₂O₃, only saturated hydrocarbons

(butane and pentane) were observed at all temperatures, thus this ratio cannot be calculated. In the case of Ni₂P/MCM-41, saturated hydrocarbons were only produced at 350 °C. The MoP/MCM-41 and WP/MCM-41 did not produce saturated hydrocarbons. Apart from the C5/C4 ratio in Fig 2.6, the saturated/unsaturated hydrocarbons ratio was high for Ni₂P/MCM-41 and CoP/MCM-41, and was low ratio for MoP/MCM-41 and WP/MCM-41. In particular, Ni₂P presented extremely high hydrogenation ability compared to CoP/MCM-41, MoP/MCM-41 and WP/MCM-41 with a saturated/unsaturated hydrocarbons ratio over 10.

2.3.4 Reaction network for HDO of GVL on phosphide catalysts and Pd/Al₂O₃

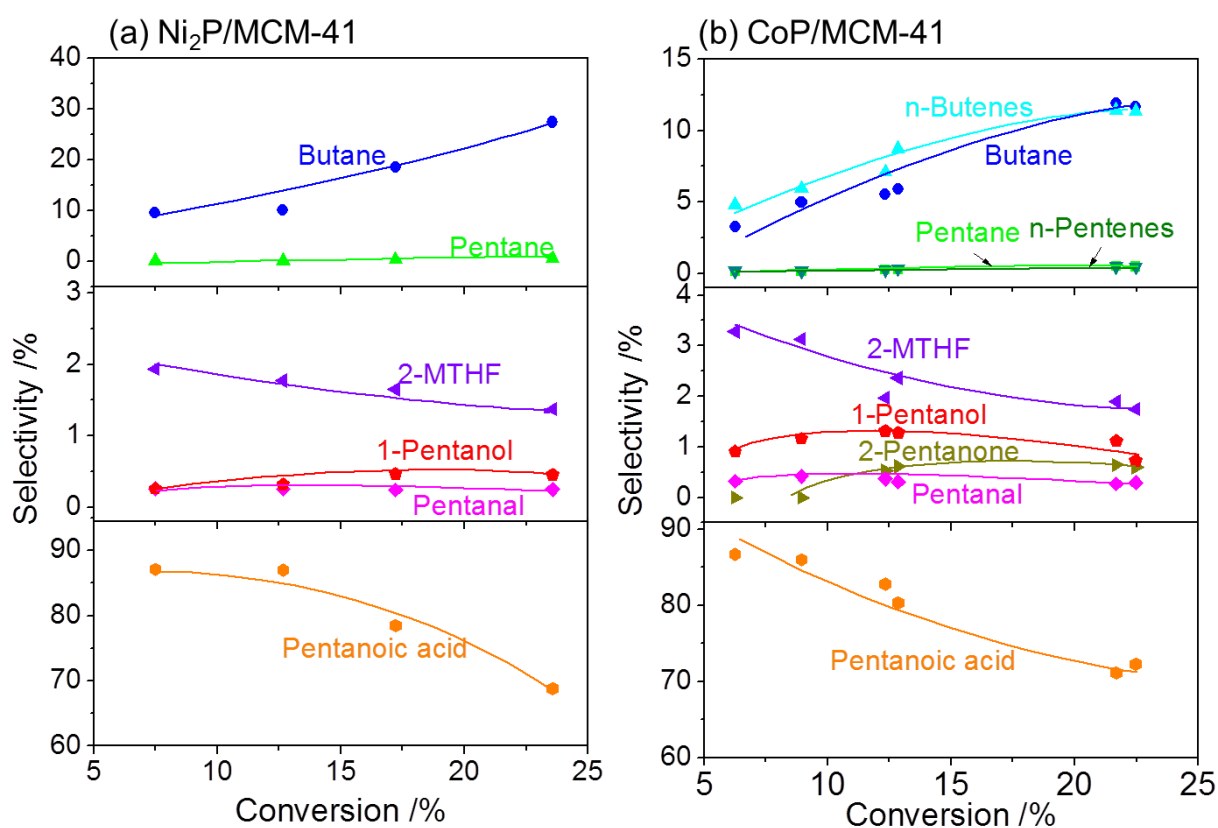


Figure 2.9. Product selectivity as a function of GVL conversion at 300 °C and 0.5 MPa on (a) Ni₂P/MCM-41 and (b) CoP/MCM-41

Fig. 2.9 shows the product selectivity as a function of GVL conversion at 300 °C and 0.5 MPa on (a) Ni₂P/MCM-41 and (b) CoP/MCM-41. These catalysts were the most active in this reaction as shown in Fig. 2.5. The results were obtained by varying the feed flowrate of the 2 mol% GVL in H₂. The selectivities to C4 hydrocarbons (butane and n-butenes) and C5 hydrocarbons (pentane and n-pentenenes) increased with the conversion, while the selectivities to 2-MTHF and pentanoic acid decreased. These results indicate that the C4 and C5 hydrocarbons were final products and that the 2-MTHF and pentanoic acid were primary products. The selectivities to 1-pentanol, pentanal and 2-pentanone went through maxima and then decreased as the conversion increased indicating that these products were intermediates.

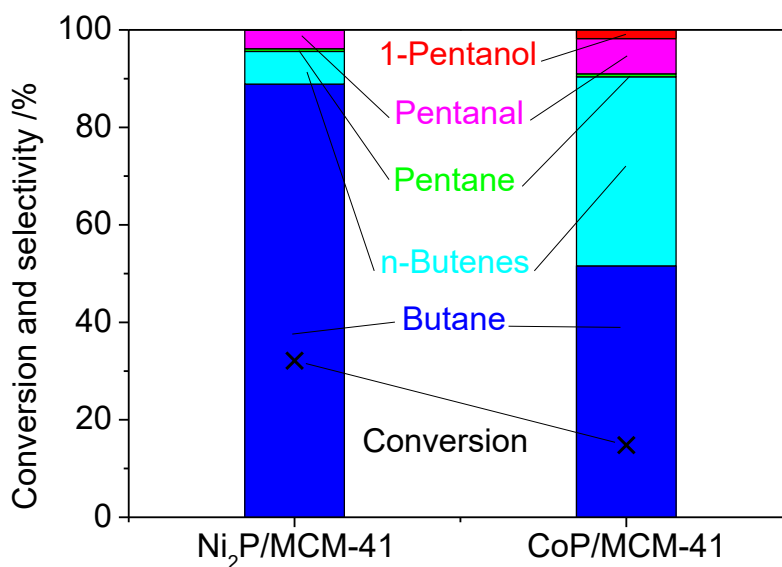


Figure 2.10. Pentanoic acid HDO on Ni₂P/MCM-41 and CoP/MCM-41 at 300 °C

Furthermore, the major product, pentanoic acid, was used as a reactant in catalytic activity tests of Ni₂P/MCM-41 and CoP/MCM-41 conducted at 0.5 MPa and 300 °C (Fig. 2.10). The main products on Ni₂P/MCM-41 were butane (89 %), n-butenes

(7 %), pentane (0.6 %), pentanal (4 %), and 1-pentanol (0.1 %), while CoP/MCM-41 produced more n-butenes (39%). These results indicated that the main reaction of pentanoic acid on Ni₂P and CoP was decarbonylation of pentanal to produce C₄ hydrocarbons while a minor route proceeded by pentanal hydrogenation to 1-pentanol and subsequent formation of pentane. Although corresponding studies of MoP and WP were not carried out, it can be surmised that they have less decarbonylation and more hydrogenation.

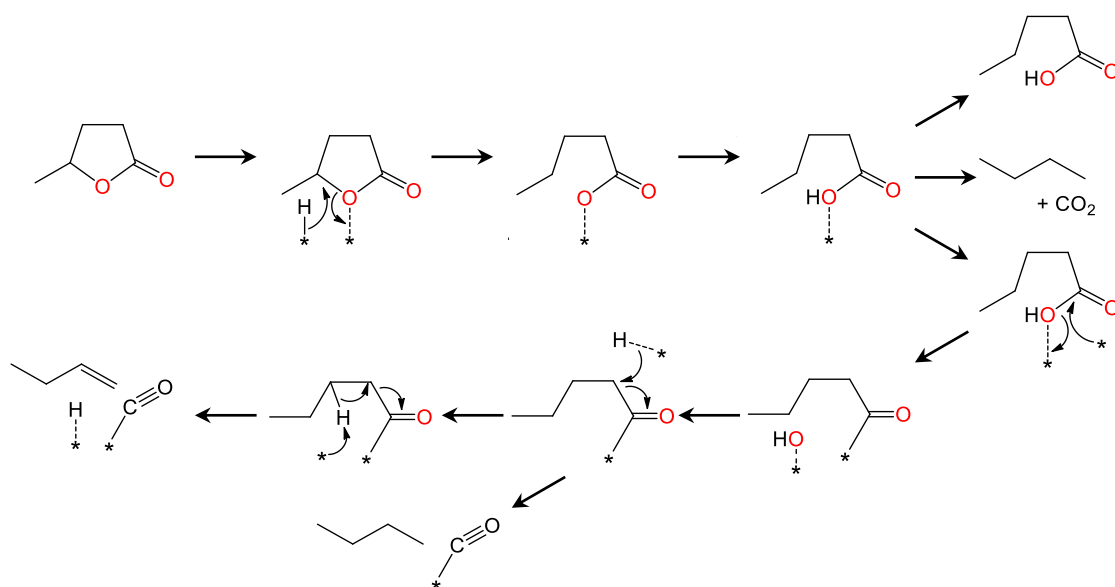


Figure 2.11. Decarbonylation route to butane and butene

A possible reaction network for the HDO of GVL is proposed (Fig. 2.12). Based on the results in Fig. 2.6, Table 2.5, Fig. 2.9, and Fig. 2.10 it can be deduced that Ni₂P/MCM-41, CoP/MCM-41 and Pd/Al₂O₃ catalysts follow the same reaction route, while MoP/MCM-41 and WP/MCM-41 involve a different reaction pathway. To begin GVL produces either 2-MTHF by hydrodeoxygenation of the C=O or pentanoic acid by ring-opening. In all catalysts, selectivity to pentanoic acid is always higher than that of

2-MTHF and the formation of 2-pentanone, which can be formed from 2-MTHF, is extremely low. Therefore, all catalysts follow a similar reaction route from GVL to pentanoic acid, involving a ring opening reaction and further hydrogenation to produce pentanal. On Ni₂P/MCM-41, CoP/MCM-41, and Pd/Al₂O₃ the formation of pentanal is followed by decarbonylation to produce butane or n-butenes plus CO. In summary all applied catalysts followed a similar initial reaction sequence from GVL to pentanal involving ring-opening and hydrogenation. After formation of pentanal the main reaction was decarbonylation on Ni₂P/MCM-41, CoP/MCM-41 and Pd/Al₂O₃ and was hydrodeoxygenation on MoP/MCM-41 and WP/MCM-41.

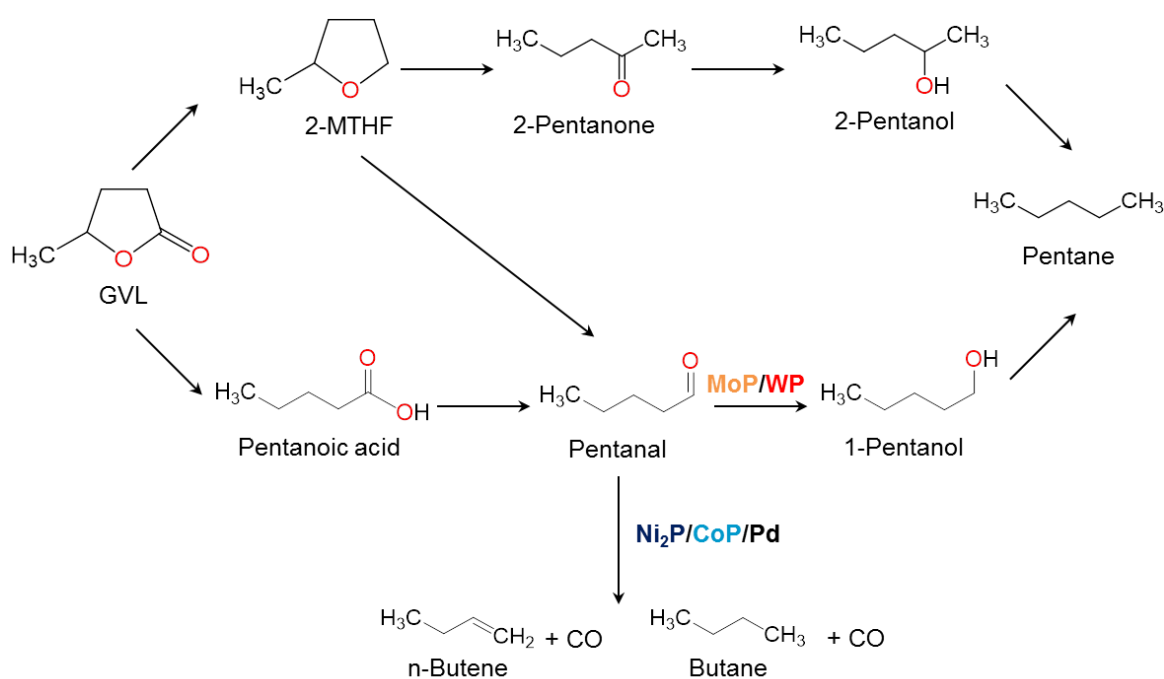


Figure 2.12. A possible reaction network for HDO of GVL

2.4 Conclusions

A series of transition metal phosphides supported on MCM-41 was prepared by temperature-programmed reduction and tested for the hydrodeoxygenation (HDO) of gamma-valerolactone (GVL). Highly dispersed phosphide catalysts were successfully synthesized, which were characterized by Brunauer-Emmett-Teller, X-Ray diffraction, X-ray absorption fine-structure and CO-chemisorption measurements. The activity for GVL conversion and deoxygenation degree followed the order: Ni₂P/MCM-41 >>CoP/MCM-41 >>Pd/Al₂O₃≈MoP/MCM-41 > WP/MCM-41. The product distribution on the iron-group phosphides (Ni₂P/MCM-41 and CoP/MCM-41) and Pd/Al₂O₃ differed from that on group 6 metal phosphides (MoP/MCM-41 and WP/MCM-41), especially in the selectivity to hydrocarbons. The main hydrocarbon product was butane on Ni₂P/MCM-41, CoP/MCM-41, and Pd/Al₂O₃ and was n-pentenes on MoP/MCM-41 and WP/MCM-41. This indicates that iron group phosphide catalysts and Pd/Al₂O₃ follow a decarbonylation pathway whereas group 6 phosphides follow an HDO pathway in the removal of oxygen. The iron group phosphides and Pd/Al₂O₃ showed high hydrogenation ability to form saturated hydrocarbons. Based on the product selectivity, there are two initial reaction routes, ring-opening and direct deoxygenation, both of which form pentanoic acid on all catalysts. Following that, pentanal is formed by hydrogenation of pentanoic acid and then as a final step decarbonylation occurs on Ni₂P/MCM-41, CoP/MCM-41 and Pd/Al₂O₃.

2.5 Supplemental information

If $\frac{-r'_a \rho_b R n}{k_c C_{Ab}} < 0.15$, then external mass transfer effects can be neglected.

Table S2.1. Parameters in the Mears criterion

R	Catalyst particle radius / cm	0.09
N	reaction order	1
$\rho_b(\text{Ni}_2\text{P, CoP, Pd})$	bulk density of catalyst bed, g/cm ³	6.E-03
$\rho_b(\text{MoP, WP})$	bulk density of catalyst bed, g/cm ³	8.E-03
C_{Ab}	bulk gas concentration of A at 300 °C, mol/cm ³	4.2E-07
k_c	mass transfer coefficient, cm/s	102

Table S2.2. Observed reaction rates and calculated Mears criterion

	Ni ₂ P	CoP	MoP	WP	Pd
Temperature /°C	Observed reaction rate /molg ⁻¹ s ⁻¹				
250	2.06E-06	3.98E-07	3.43E-07	3.15E-08	4.72E-07
275	4.58E-06	9.13E-07	4.60E-07	7.02E-08	7.04E-07
300	8.80E-06	2.08E-06	8.40E-07	1.53E-07	1.14E-06
325	1.12E-05	3.92E-06	1.44E-06	3.00E-07	1.99E-06
350	1.14E-05	6.73E-06	2.58E-06	5.64E-07	3.07E-06
Temperature /°C	Mears criterion				
250	2.37E-05	4.58E-06	5.26E-06	4.83E-07	5.43E-06
275	5.52E-05	1.10E-05	7.40E-06	1.13E-06	8.49E-06
300	1.11E-04	2.63E-05	1.41E-05	2.58E-06	1.44E-05
325	1.47E-04	5.16E-05	2.53E-05	5.26E-06	2.62E-05
350	1.57E-04	9.23E-05	4.72E-05	1.03E-05	4.20E-05

2.6 Appendix

Hydrodeoxygenation of γ -valerolactone on Ni supported on MCM-41

2.6.1 Ni/MCM-41 catalyst preparation

As a comparison, Ni/MCM-41 catalyst was synthesized by temperature-programmed reduction (TPR) method. An aqueous solution containing $\text{Ni}(\text{NO}_3)_2 \cdot 6\text{H}_2\text{O}$ was impregnated on MCM-41 support ($1.0 \text{ mmol}_{\text{Ni}}/\text{g}_{\text{support}}$). The resulting precursor was dried at $120 \text{ }^\circ\text{C}$ for 12 h and then calcined at $550 \text{ }^\circ\text{C}$ for 4 h. After the calcination, the precursor was pelletized and sieved to a size of $650\text{--}1180 \text{ }\mu\text{m}$. The calcined precursor was reduced at $450 \text{ }^\circ\text{C}$ for 2 h under H_2 flow ($1000 \text{ ml/min g}_{\text{sample}}$) and then passivated at room temperature for 4 h under $0.5 \text{ \% O}_2/\text{N}_2$.

2.6.2 Characterization

The prepared Ni/MCM-41 sample was characterized by BET, TPR, CO uptake, and XRD measurements with same manner in metal phosphide catalysts (See 2.2.2 Characterization of prepared catalyst samples).

2.6.3. Activity test for HDO of GVL

The catalytic tests of HDO for GVL on Ni/MCM-41 were carried out in a continuous-flow reactor operated at 0.5 MPa and a temperature range of $150\text{--}350 \text{ }^\circ\text{C}$. Quantities of catalyst corresponding to $10 \text{ }\mu\text{mol}$ of sites (0.3 g) as titrated by CO chemisorption were used. Before injecting the liquid feed, the Ni/MCM-41 catalyst was pretreated under a H_2 flow of $100 \text{ cm}^3 \text{ min}^{-1} \text{ g}_{\text{catalyst}}^{-1}$ at $400 \text{ }^\circ\text{C}$ for 2 h. The reactant was introduced into the reactor with a liquid pump. A mixture of 98 wt. \% of GVL and 2 wt. \% of toluene as an internal standard was vaporized at $300 \text{ }^\circ\text{C}$ and mixed with a H_2 gas stream to give a reactant stream of 4 mol\% GVL in H_2 . The total pressure was fixed at 0.5 MPa using a back-pressure regulator. For stabilization, the catalysts were first

maintained at 350 °C and 0.5 MPa for 12 h after introducing the reactant and then the temperature was varied downward and upward in the order: 350, 300, 250, 200, 150, 175, 225, 275, and 325 °C with each temperature maintained for 2 or 3 h.

4. Results and discussion

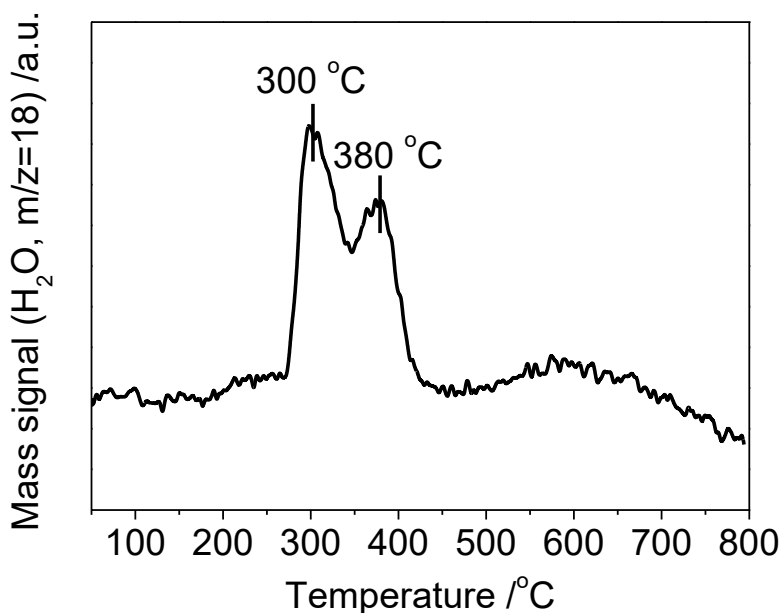


Figure A1. TPR profile for precursor of Ni/MCM-41

Fig. A1 shows the TPR profile for Ni/MCM-41 precursor. There are two H₂ consumption peaks centered at 300 °C and 380 °C. The first peak at low temperature is due to the reduction of NiO to Ni⁰ weakly interacting with the support and the second peak is because of NiO species and Ni²⁺ ions strongly interacting with the support.

Fig. A2 shows the XRD patterns for Ni/MCM and Ni₂P/MCM-41. The Ni₂P/MCM-41 shows broad peaks at $2\theta = 40.7^\circ$, 44.6° , 47.4° , and 54.2° , which are corresponding to reference Ni₂P sample. On the other hand, Ni/MCM-41 shows distinct peaks at $2\theta = 44.5^\circ$ and 51.8° , which are corresponding to reference Ni sample. These results indicate that Ni₂P particles are highly dispersed on the MCM-41 suggesting that

P enhances metal dispersion. In previous work [49], Bussell's group reported that incorporation of phosphorous into the silica-supported catalysts enhanced the dispersion of the Ni phase.

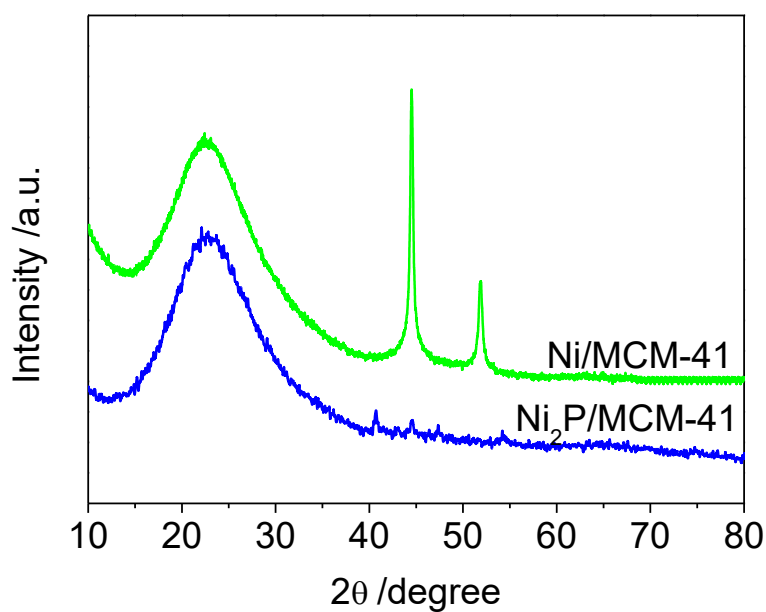


Figure A2. XRD profile for Ni/MCM-41 and Ni₂P/MCM-41

Figure A3 shows GVL conversion as a function of temperature on Ni/MCM-41, Ni₂P/MCM-41, POx/MCM-41, and MCM-41 at 0.5 MPa with 4 mol% GVL in H₂. In order to check stability of catalysts, after one cycle running of temperature dependence testing the conversion was obtained at same points at 300 and 350 °C (open mark). Ni₂P/MCM-41 exhibited stable performance with showing slightly decreasing conversion after the one cycle testing, while Ni/MCM-41 presented low stability during the test with the decrease of conversion. Furthermore, Ni₂P/MCM-41 shows higher activity compared than Ni/MCM-41. These results indicate that Ni₂P/MCM-41 is better performance in terms of activity and stability than Ni/MCM-41.

Figure A4 shows product distribution for HDO of GVL as a function of temperature at 0.5 MPa on (a) Ni/MCM-41 and (b) Ni₂P/MCM-41. The Ni/MCM-41 produced broadening distribution with cracking products such as methane, ethane, propane, and butane. At high temperature (350 °C), oxygen containing compounds (butanol, 2-MTHF and pentanoic acid) were still remained and most of oxygen containing compounds were converted into methane and butane. The formation of CO₂ was observed and it is evidence of decarboxylation. On the other hand, the Ni₂P/MCM-41 produced mainly CO, butane and pentanoic acid. At high temperature, oxygen-containing compounds were converted into butane which was produced by decarbonylation with formation of CO. These results indicate that addition of phosphorous inhibited the cracking activity of Ni metal. This is because of ligand effect which can enhance the dissociation of reactant and molecular hydrogen [50].

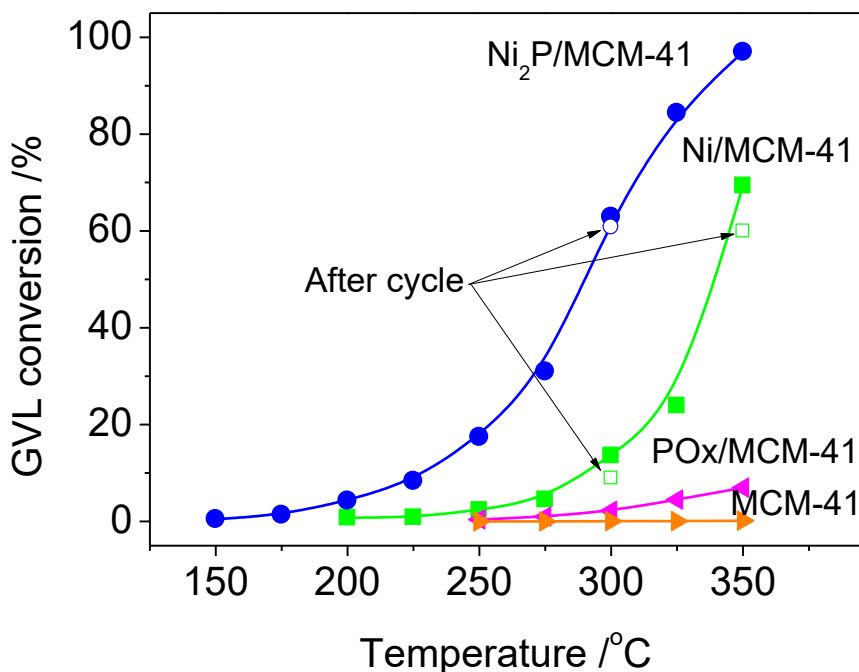


Figure A3. GVL conversion as a function of temperature on Ni/MCM-41, Ni₂P/MCM-41, POx/MCM-41, and MCM-41 at 0.5 MPa with 4 mol% GVL in H₂

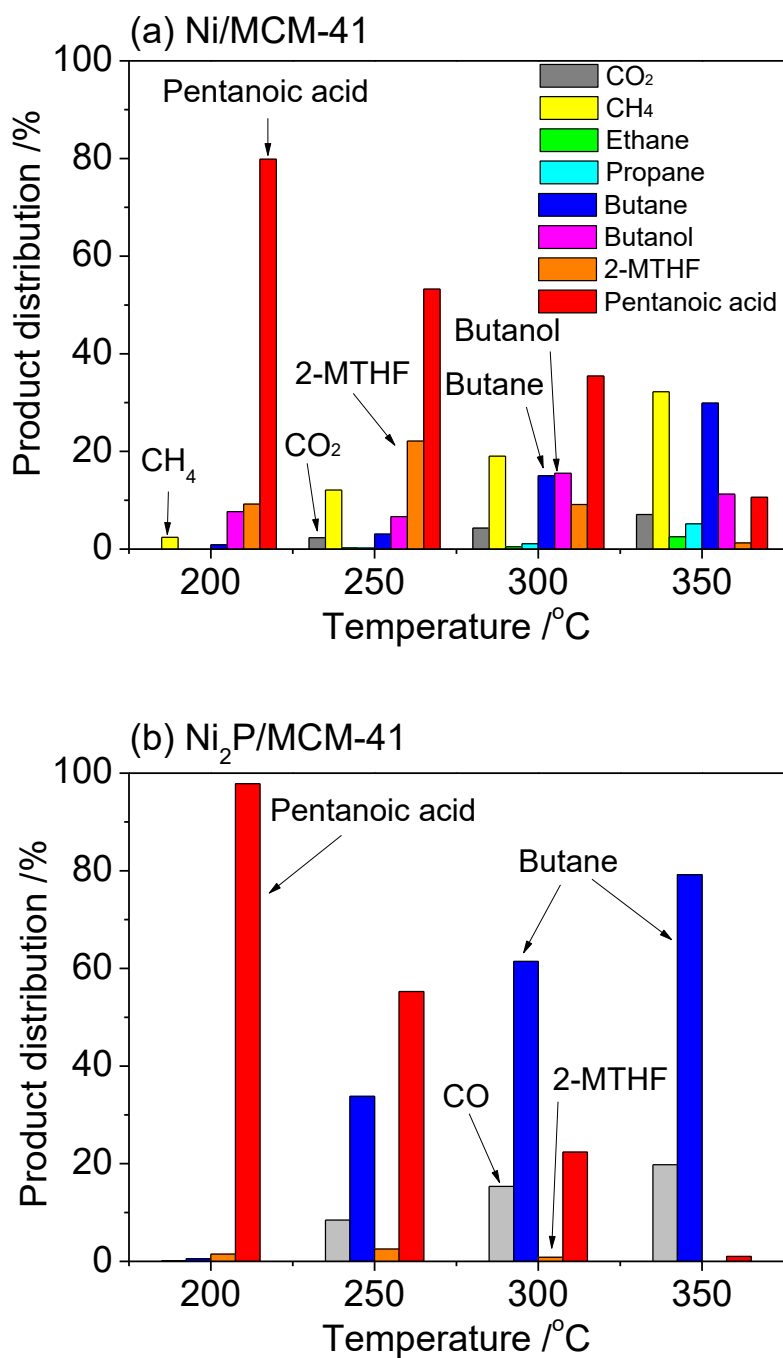


Figure A4. Product distribution for HDO of GVL as a function of temperature at 0.5 MPa on (a) Ni/MCM-41 and (b) Ni₂P/MCM-41

Reference

- [1] H. Hernando, S. Jiménez-Sánchez, J. Feroso, P. Pizarro, J. M. Coronado and D. P. Serrano, *Catal. Sci. Technol.* 6 (2016) 2829–2843
- [2] S. D. Stefanidis, K. G. Kalogiannis, P. A. Pilavachi, C. M. Fougret, E. Jordan and A. A. Lappas, *Catal. Sci. Technol.* 6 (2016) 2807–2819
- [3] C.-H. Zhou, X. Xia, C.-X. Lin, D.-S. Tong and J. Beltramini, *Chem. Soc. Rev.* 40 (2011) 5588–5617
- [4] L. Nazari, Z. Yuan, S. Souzanchi, M. B. Ray, C. Xu, *Fuel* 162 (2015) 74–83
- [5] N. Koike, S. Hosokai, A. Takagaki, S. Nishimura, R. Kikuchi, K. Ebitani, Y. Suzuki, S. T. Oyama, *J. Catal.* 333 (2016) 115–126
- [6] M. S. Mettler, A. D. Paulsen, D. G. Vlachos and P. J. Dauenhauer, *Catal. Sci. Technol.* 4 (2014) 3822–3825
- [7] T. Wang, S. Qiu, Y. Weng, L. Chen, Q. Liu, J. Long, J. Tan, Q. Zhang, Q. Zhang, L. Ma, *Appl. Energ.* 160 (2015) 329–335
- [8] A.V. Bridgwater, *Biomass Bioenerg.* 38 (2012) 68–94
- [9] C. Perego and M. Ricci, *Catal. Sci. Technol.* 2 (2012) 1776–1786
- [10] I. D. V. Torri, V. Paasikallio, C. S. Faccini, R. Huff, E. B. Caramão, V. Sacon, A. Oasmaa, C. A. Zini, *Bioresource Technology* 200 (2016) 680–690
- [11] J. Chen and Q. Xu, *Catal. Sci. Technol.* 6 (2016) 7239–7251
- [12] J. K. Satyarthi, T. Chiranjeevi, D. T. Gokak and P. S. Viswanathan, *Catal. Sci. Technol.* 3 (2013) 70–80
- [13] O. I. Senol, E.-M. Ryymin, T.-R. Viljava, A. O. I. Krause, *J. Mol. Catal. A: Chem.* 277 (2007) 107–112
- [14] E.-M. Ryymin, M.L. Honkela, T.-R. Viljava, A.O.I. Krause, *Appl. Catal. A: Gen.* 358 (2009) 42–48
- [15] L. Nie, D. E. Resasco, *J. Catal.* 317 (2014) 22–29
- [16] H. Xu, K. Wang, H. Zhang, L. Hao, J. Xu and Z. Liu, *Catal. Sci. Technol.* 4 (2014) 2658–2663
- [17] L. Wang, H. Wan, S. Jin, X. Chen, C. Li, C. Liang, *Catal. Sci. Technol.* 5 (2015) 465–474
- [18] C. Zhao, J. He, A. A. Lemonidou, X. Li, J. A. Lercher, *J. Catal.*, 280 (2011) 8–16

-
- [19] C. Newman, X. Zhou, B. Goundie, I. T. Ghampson, R. A. Pollock, Z. Ross, M. C. Wheeler, R. W. Meulenberg, R. N. Austin, B. G. Frederick, *Appl. Catal. A: Gen.* 477 (2014) 64–74
- [20] R. C. Runnebaum, T. Nimmanwudipong, D. E. Block and B. C. Gates, *Catal. Sci. Technol.* 2 (2012) 113–118
- [21] Y. K. Lugo-José, J. R. Monnier, A. Heyden and C. T. Williams, *Catal. Sci. Technol.* 4 (2014) 3909–3916
- [22] Y. K. Lugo-José, J. R. Monnier, C. T. Williams, *Appl. Catal. A: Gen.* 469 (2014) 410–418
- [23] B. Dhandapani, T. St. Clair, S.T. Oyama, *Appl. Catal. A: Gen.* 168 (1998) 219–228
- [24] Z. He, X. Wang, *Catalysis for sustainable energy* 1 (2012) 28–52
- [25] A. Iino, A. Cho, A. Takagaki, R. Kikuchi, S. T. Oyama, *J. Catal.* 311 (2014) 17–27
- [26] A. Cho, H. Kim, A. Iino, A. Takagaki, S. T. Oyama, *J. Catal.* 318 (2014) 151–161
- [27] A. Cho, A. Takagaki, R. Kikuchi, S. T. Oyama, *Top Catal.* 58 (2015) 219–231
- [28] L. Yang, X. Li, A. Wang, R. Prins, Y. Chen, X. Duan, *J. Catal.* 330 (2015) 330–343
- [29] A. I. d’Aquino, S. J. Danforth, T. R. Clinkingbeard, B. Ilic, L. Pullan, M. A. Reynolds, B. D. Murray, M. E. Bussell, *J. Catal.* 335 (2016) 204–214
- [30] P. Bui, J. A. Cecilia, S. Ted. Oyama, A. Takagaki, A. Infantes-Molina, H. Zhao, D. Li, E. Rodríguez-Castellón, A. Jiménez López, *J. Catal.* 294 (2012) 184–198
- [31] J. Chen, H. Shi, L. Li, K. Li, *Appl. Catal. B: Environ.* 144 (2014) 870–884
- [32] F. Liguori, C. Moreno-Marrodan, P. Barbaro, *ACS Catal.* 5 (2015) 1882–1894
- [33] D. M. Alonso, S. G. Wettstein, J. A. Dumesic, *Green Chem.* 15 (2013) 584–595
- [34] J. Q. Bond, D. M. Alonso, D. Wang, R. M. West, J. A. Dumesic, *Science* 327 (2010) 1110–1114
- [35] J. C. Serrano-Ruiz, D. J. Braden, R. M. West, J. A. Dumesic, *Appl. Catal. B: Environ.* 100 (2010) 184–189
- [36] J.-P. Lange, R. Price, P. M. Ayoub, J. Louis, L. Petrus, L. Clarke, H. Gosselink, *Angew. Chem. Int. Ed.* 49 (2010) 4479–4483

-
- [37] P. Sun, G. Gao, Z. Zhao, C. Xia, F. Li, *ACS Catal.* 4 (2014) 4136–4142
- [38] J.A. Cecilia, A. Infantes-Molina, E. Rodríguez-Castellón, A. Jiménez-López, *J. Catal.* 263 (2009) 4–15
- [39] J.A. Cecilia, A. Infantes-Molina, E. Rodríguez-Castellón, A. Jiménez-López, *Appl. Catal. B: Environ.* 92 (2009) 100–113
- [40] J. A. Cecilia, A. Infantes-Molina, E. Rodríguez-Castellón, A. Jiménez-López, *J. Phys. Chem. C* 113 (2009) 17032–17044
- [41] Y. Shu, Y.-K. Lee, S. T. Oyama, *J. Catal.* 236 (2005) 112–121
- [42] Y.-K. Lee, Y. Shu, S. T. Oyama, *Appl. Catal. A: Gen.* 322 (2007) 191–204
- [43] S. T. Oyama, X. Zhang, Y.-K. Lee, and W.-J. Chun, *J. Catal.* 221 (2004) 263–273
- [44] Y.-K. Lee, S. T. Oyama, *J. Catal.* 239 (2006) 376–389
- [45] S. T. Oyama, X. Zhang, J. Lu, Y. Gu, T. Fujitani, *J. Catal.* 257 (2008) 1–4
- [46] P.B. Weisz, C.D. Prater, *Adv. in Catal.* 6 (1954) 143–196
- [47] Vannice, M. Albert, *Kinetics of catalytic reactions*. Springer Science+Business Media, 2005, Chapter 4, 63–65
- [48] D. E. Mears, *Ind. Eng. Chem. Process Des. Dev.* 10 (1971) 541–547
- [49] S. J. Sawhill, K. A. Layman, D. R. Van Wyk, M. H. Engelhard, C. Wang, M. E. Bussell, *J. Catal.* 231 (2005) 300–313
- [50] P. Liu, J. A. Rodriguez, T. Asakura, J. Gomes, K. Nakamura, *J. Phys. Chem. B* 109 (2005) 4575–4583

Chapter 3

Hydrodeoxygenation of γ -Valerolactone on Bimetallic NiMo Phosphide Catalysts

3.1 Introduction

Bio-oil derived from biomass is being considered as a sustainable source for the production of a variety of chemicals and fuels [1, 2, 3]. Unlike current petroleum-based chemicals, bio-oil contains a lot of oxygen-containing compounds such as furans, pyrans, phenols, and lactones, which are undesirable components in fuels and fuel-additives, leading to low heating value, high acidity, and chemical and thermal instability [4, 5].

Hydrodeoxygenation (HDO) is a key process to lower the oxygen content of biomass streams, analogous to hydrodesulfurization (HDS) and hydrodenitrogenation (HDN) processes that lower sulfur and nitrogen levels in petroleum feedstocks [6, 7]. The development of effective HDO catalysts is critical to unearthing the full potential of biomass-derived compounds.

Traditionally, molybdenum sulfide (MoS_2) catalysts supported on $\gamma\text{-Al}_2\text{O}_3$ with either nickel or cobalt as a promoter have been used in the HDS and HDN processes [8, 9, 10]. In addition, a plethora of studies for bimetallic sulfide catalysts has reported the existence of synergistic effect between metals, which enhances the performance of the catalysts in comparison to their monometallic counterparts [11]. For example, in the simultaneous HDS of dibenzothiophene and HDN of *o*-propylaniline promoted NiMoS catalysts showed more elevated dispersion, higher concentration of adsorption sites, and

enhanced intrinsic activity compared to the plain MoS₂ phase [8]. However, the application of sulfide catalysts for bio-oil upgrading is limited by their need for a sulfur source to maintain their activity, leading to increased interest in non-sulfide catalysts [12]. Transition metal phosphides, which have been demonstrated to be effective HDS [13, 14] and HDN [15, 16] catalysts, are considered as a viable alternative to sulfide catalysts for HDO [17, 18]. The subject has been reviewed [19,20,21,22]. Recently, several studies on HDO over phosphide catalysts have been reported showing their higher activity and stability compared to commercial sulfide catalysts [23, 24]. It has been found that a commercial CoMoS/Al₂O₃ quickly deactivated and exhibited lower activity compared to phosphide catalysts in the HDO of guaiacol at the same reaction conditions.

Furthermore, several studies involving alloys of phosphide catalysts have been undertaken [25, 26, 27]. A study of the HDO of aryl ethers and phenol revealed that bimetallic FeMoP catalysts were highly selective for C-O bond cleavage (~ 90 % benzene selectivity) at 400 °C and 2.1 MPa [28]. In another study the HDO of 2-MTHF over bimetallic NiFeP catalysts was investigated, in which a weak ligand effect and a significant ensemble effect on the selectivity at equal number of active sites were observed [29]. The catalytic performance of bimetallic NiMoP catalysts in the deoxygenation of methyl laurate has also been investigated, and it was shown that charge transfer from Ni to Mo in NiMoP₂ or the incorporation of Mo into the Ni₂P lattice was responsible for modifying the reaction pathway [30]. Furthermore, a study of HDS activities of dibenzothiophene was performed at 320 °C and 3.0 MPa for phosphide catalysts and it was found that catalytic activities followed the order: Ni₂P/SiO₂ > NiMoP/SiO₂ > MoP/SiO₂ and the bimetallic NiMoP/SiO₂ catalyst

presented no synergetic effect in activity between phosphide components [31]. On the other hand, an investigation of 4,6-dimethyldibenzothiophene at 310 °C and 3.0 MPa showed the TOF in HDS did not vary much with Mo content [32]. Also, a study of methyl laurate deoxygenation at 300-340 °C and 3.0 MPa found increasing turnover frequency with increasing Mo in Ni-Mo phosphides [27].

The Mo-Ni-P system has been well studied and the known phases and structures have been summarized [33]. As is the case with pure metallic combinations, several specific stoichiometries have been identified, but the materials are referred to as solid solutions [33] or alloys because of their variable composition. Solid solutions in phosphides are well known, for example, NiFeP [34,35], FeCoP, FeMnP and FeWP [36].

In our previous work [37], Ni₂P/MCM-41 and MoP/MCM-41 showed distinct features in activity and selectivity for the HDO of γ -valerolactone. Ni₂P was intrinsically more active but showed lower HDO selectivity (producing mainly C₄ hydrocarbons via decarbonylation), while MoP/MCM-41 was less active but showed higher HDO selectivity (producing mainly C₅ hydrocarbons). This result provides an incentive to explore bimetallic NiMoP catalysts for the HDO of GVL to ascertain possible changes in reactivity in comparison to their monometallic counterparts. In this work, a series of bimetallic NiMoP catalysts with various Ni and Mo metal ratios were prepared, and their activity was tested in the HDO of γ -valerolactone at 0.5 MPa. Analysis by XRD indicated the formation of phase pure alloy and surface site was titrated with CO uptake and fourier transform infrared (FTIR) was used to distinguish adsorption on Ni and Mo sites. It was found that surface Ni atoms controlled the reactivity, but that Mo atoms influenced the selectivity.

3.2 Experimental

3.2.1 Preparation of bimetallic NiMo phosphide catalysts

Table 3.1. Quantities of materials used in catalyst preparation

Sample	Support /g	Ni(OH) ₂ /mmol	(NH ₄) ₆ Mo ₇ O ₂₄ · 4H ₂ O /mmol	Ni /wt.%	Mo /wt.%	P /wt.%
Ni ₂ P/MCM-41	5	5.00	-	5.2	-	5.5
NiMo(3:1)P/MCM-41	5	3.75	0.18	3.9	2.1	5.5
NiMo(1:1)P/MCM-41	5	2.50	0.36	2.6	4.2	5.4
NiMo(1:3)P/MCM-41	5	1.25	0.54	1.3	6.3	5.4
MoP/MCM-41	5	-	0.71	-	8.3	5.3

H₃PO₃: 10 mmol

A commercial MCM-41 support (Aldrich) was used as received. Samples of the Ni₂P/MCM-41, MoP/MCM-41, and NiMoP/MCM-41 catalysts with varying nickel to molybdenum molar ratios were prepared by incipient wetness impregnation of aqueous precursor solutions, followed by temperature-programmed reduction (TPR). The precursor solutions were prepared by dissolving appropriate amounts of Ni(OH)₂ (Aldrich, 99 %) and/or (NH₄)₆ Mo₇O₂₄ · 4H₂O (Aldrich, 99 %) with H₃PO₃ (Aldrich, 99 %) in distilled water. The initial (Ni+Mo)/P molar ratio in the solutions was fixed to 1/2, and the total amount of metal was maintained at 1.0 mmol/g_{support}. The quantities of Ni, Mo and P in each sample are summarized in Table 3.1. After impregnation, the samples were dried at 80 °C for 12 h without calcination, and then pelletized and sieved to a size of 650-1180 μm. The resulting precursors were reduced to phosphides under 1000 cm³ min⁻¹ g⁻¹_{catalyst} of hydrogen. The reduction temperature of the catalysts was determined by the TPR method, using the peak maximum for the synthesis. After reduction, the phosphides were cooled to room temperature under helium flow and then passivated under 0.2 % O₂/He flow (100 cm³ min⁻¹ g⁻¹_{catalyst}) for 3 h.

3.2.2 Characterization

The reduction characteristics of the catalysts were determined by H₂-temperature-programmed reduction (TPR). Dried precursors (0.1 g) were placed in a quartz reactor and heated from 50 to 800 °C at 3 °C/min under H₂ flow of 100 cm³ min⁻¹ while monitoring the water signal (m/z=18) with a quadruple mass spectrometer. The TPR peak maxima were used in the reduction of the catalyst precursors to prepare the catalyst samples. Following this reduction procedure, the materials were passivated as described previously. For subsequent characterization and catalytic testing the passivated samples were re-reduced at 550 °C. The procedures are described in the following paragraphs.

Surface metal atoms were titrated by chemisorption uptake of carbon monoxide (CO). Before the measurement, the catalyst sample was pretreated at 550 °C for 2 h in H₂ flow and then pulses of CO in a He flow (3 % CO/He gas) were passed over the sample at 50 °C, and the mass signal (m/z = 28) was monitored by the mass spectrometer to measure the total dynamic gas uptake. The specific surface area of the samples was calculated from the linear portion of BET plots ($P/P_0 = 0.01 - 0.20$) obtained from N₂ adsorption isotherms at 77 K using a BELSORP mini II micropore size analyzer. Prior to the measurements, all the samples were dried and evacuated at 120 °C overnight. X-ray diffraction (XRD) patterns of passivated samples were measured with a diffractometer (Rigaku RINT 2400) operated at 40 kV and 100 mA, using a Cu-K α monochromatic x-ray source. Fourier transform infrared (FTIR) measurements of the samples were performed using a JASCO FT/IR-6100 spectrometer. About 15 mg of the powder samples were pressed at 3.0 MPa into a disk-type wafer and placed in an infrared cell with KBr windows. Prior to the measurements, the IR cell was

purged in flowing N₂ for 0.5 h, pretreated under flowing H₂ at 550 °C for 2 h, and then cooled to 50 °C under N₂ flow. A 3 % CO/He gas mixture was introduced over the sample until saturation was completed. Afterwards, the sample was purged under flowing N₂ to remove gas phase CO and physically and weakly adsorbed CO species on the catalyst surface. Spectra were then recorded in the absorbance mode with a resolution of 4 cm⁻¹ using 200 scans in the region of 4,000–1,000 cm⁻¹. Background spectra were recorded under N₂ flow before injection of CO.

X-ray absorption near-edge structure (XANES) spectra at the Ni K-edge (8.333 keV) were obtained at beam line 9C (BL9C) of the Photon Factory in the Institute of Materials Structure Science, High-Energy Accelerator Research Organization (KEK-IMSS-PF). The X-ray ring was operated at 2.5 GeV with a beam current of 450 mA. The XANES spectra were taken in transmission mode using ionization chambers for the detection of the incident X-ray beam (I₀, 100% N₂) and transmitted beam (I_T, 25% Ar in N₂). The passivated disk sample was placed in the center of an in situ cell equipped with Kapton windows, and reduced at 550 °C for 3 h under a H₂ flow.

3.2.3 Activity testing

The catalytic tests of HDO of GVL were carried out in a tubular fixed-bed reactor operated at 0.5 MPa and a temperature range of 200-350 °C. Quantities of catalyst corresponding to 10 μmol of sites (as determined by CO chemisorption) were diluted with quartz sand and loaded in the middle section of the reactor, about 2 cm long. Quantities used were 0.14 g for Ni₂P/MCM-41, 0.19 g for NiMo(3:1)P/MCM-41, 0.2 g for NiMo(1:1)P/MCM-41, 0.18 g for NiMo(1:3)P/MCM-41, and 0.14 g for MoP/MCM-41. After pretreatment of the catalyst under a H₂ flow of 100 Ncm³min⁻¹g_{catalyst}⁻¹ at 550

°C for 3 h, the total pressure was fixed at 0.5 MPa using a back-pressure regulator. The reactant containing 98 wt. % of GVL and 2 wt. % of toluene as an internal standard was fed with a liquid pump via vaporizer at 300 °C with a H₂ gas stream. The toluene was not hydrogenated at the reaction conditions used in this study. The reactant stream of 2 mol% GVL in H₂ was fed at 1.7 μmol s⁻¹. Flow rates in μmol s⁻¹ can be converted to Ncm³ min⁻¹ by multiplication by 1.5. The reactivity of the catalysts was tested by varying the temperature in the following order: 350, 300, 250, 200, 225, 275 and 325 °C, with each temperature maintained for 2 or 3 h. Before the measurements the catalyst was pretreated at 550 °C before changing the reaction temperature and to reach steady-state, the catalysts were stabilized at 350 °C with 2 mol% GVL in H₂. Then reaction temperature was varied without further stabilization at 350 °C. For comparison, a physical mixture of Ni₂P/MCM-41 and MoP/MCM-41 was tested as well. Before changing the reaction temperature, the catalysts were stabilized at 350 °C and 0.5 MPa for 12 h under the reactant stream. An on-line gas chromatograph (Shimadzu GC-14A, DB-624 UI, 60 m x 0.25 mm x 1.40 μm) equipped with a flame ionization detector (FID) and a thermal conductivity detector (TCD) was used for analyzing the products at 1 h intervals. For comparison, a physically mixture sample of 0.071 g of Ni₂P/MCM-41 and 0.067 g of MoP/MCM-41 was prepared and its reactivity was evaluated at the same conditions as the Ni-Mo-P samples. Reactivity was also studied as a function of contact time at 300 °C and 0.5 MPa over the NiMo(1:1)P/MCM-41 catalyst.

The GVL conversion, product distribution, selectivity and turnover frequency value were calculated by the following equations:

$$\text{GVL conversion} = \left(1 - \frac{n_{\text{GVL,e}}}{n_{\text{GVL,f}}} \right) \times 100\%$$

$$\text{Selectivity, } S_i = \left(\frac{n_i}{\sum n_i} \right)$$

Where $n_{GVL,f}$ and $n_{GVL,e}$ denote the moles of GVL in the feed and exit, respectively, and n_i is the moles of product i .

$$\text{TOF}(\text{s}^{-1}) = \frac{\text{Conversion} \times \text{Flow rate of GVL } (\mu\text{mol s}^{-1})}{\text{Catalyst weight}(\text{g}) \times \text{Quantity of CO uptake site } (\text{g}^{-1})}$$

3.3 Results and discussion

3.3.1 Synthesis and characterization

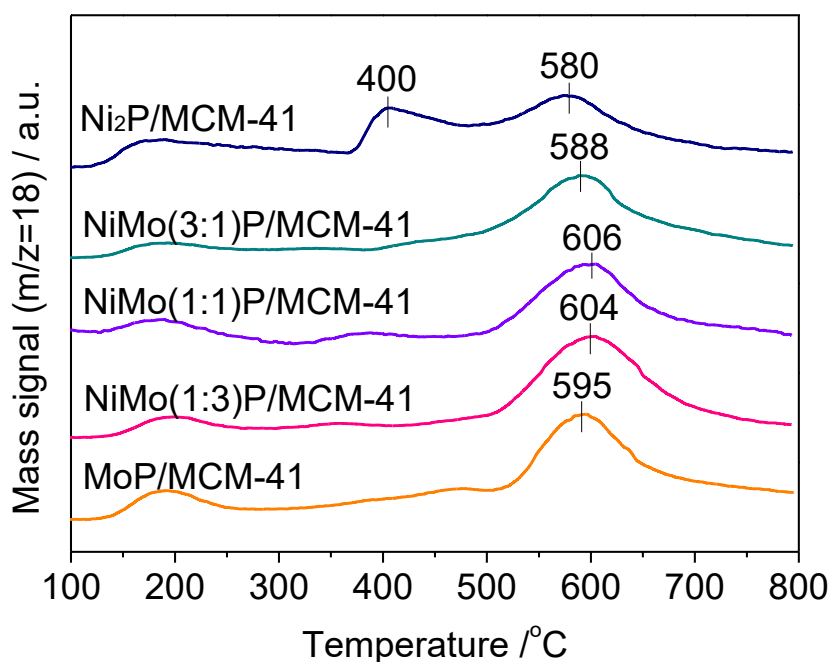


Figure 3.1. TPR profiles (mass signal, $m/z=18$) for the precursors (0.1 g) of phosphide catalyst samples under H_2 flow of $100 \text{ cm}^3 \text{ min}^{-1}$

Fig. 3.1 shows the temperature-programmed reduction (TPR) profiles of the precursors of phosphide catalysts with different Ni and Mo contents. The maximum peak temperature was chosen as the reduction temperature for the syntheses of larger batches of the catalyst for characterization and reactivity testing. The temperatures

were determined to be 580 °C for Ni₂P/MCM-41, 588 °C for NiMo(3:1)P/MCM-41, 606 °C for NiMo(1:1)P/MCM-41, 604 °C for NiMo(1:3)P/MCM-41, and 595 °C for MoP/MCM-41. The Ni₂P catalyst precursor had two main reduction peaks centered at 400 and 580 °C due to different stages in the reduction of Ni phosphite to Ni phosphide [38], while Mo-containing catalysts had a main reduction peak at higher temperature between 588 - 606 °C. This is ascribed to differences in the reducibility of the metals, with Ni more easily reduced compared to Mo [30]. The bimetallic phosphide catalysts presented higher reduction temperature than monometallic phosphide catalysts, especially NiMo(1:1)P/MCM-41, indicating that the reduction of the precursor became more difficult due to Ni-Mo interactions. Although the temperature shifts are small, there are trends in the data, and they are consistent with the formation of Ni-Mo-P alloys. The shifts to higher temperature are consistent with a favorable heat of interaction of the components in the solid solution.

Table 3.2. Crystal data in the Ni-Mo-P system

Compound	Group	a	c	Ref
Ni ₂ P	P $\bar{6}$ 2m	0.5859	0.3382	41
NiMoP	P $\bar{6}$ 2m	0.5861	0.3704	42,43
MoP	P $\bar{6}$ m2	0.3223	0.3191	44

Fig. 3.2 shows the wide-angle XRD patterns of the reduced and passivated phosphide catalysts. The diffraction patterns of NiMoP (PDF 71-0202), Ni₂P (PDF 74-1385), and MoP (PDF 24-0771) are included in Fig. 3.2 as references. A broad peak observed at $2\theta = 14 - 37^\circ$ in all the catalysts is associated with amorphous silica of the MCM-41 support. It is difficult to distinguish distinct peaks of Ni₂P and MoP phases in

all the catalyst samples in the patterns because of the high-surface area MCM-41 support ($997 \text{ m}^2 \text{ g}^{-1}$) which led to highly dispersed metal phosphides.

The crystal chemistry in the Ni-Mo-P system has been well documented [33]. Several compounds with specific stoichiometries have been identified [39,40], but Ni_2P [41] and NiMoP [42, 43] both share the same hexagonal space group (Table 3.2) while MoP has a different hexagonal structure [44]. Unsupported $\text{Ni}_{2-x}\text{Mo}_x\text{P}$ powders of variable composition have been reported and shown to obey Vegard's law [45], so the supported materials here are expected to form solid solutions.

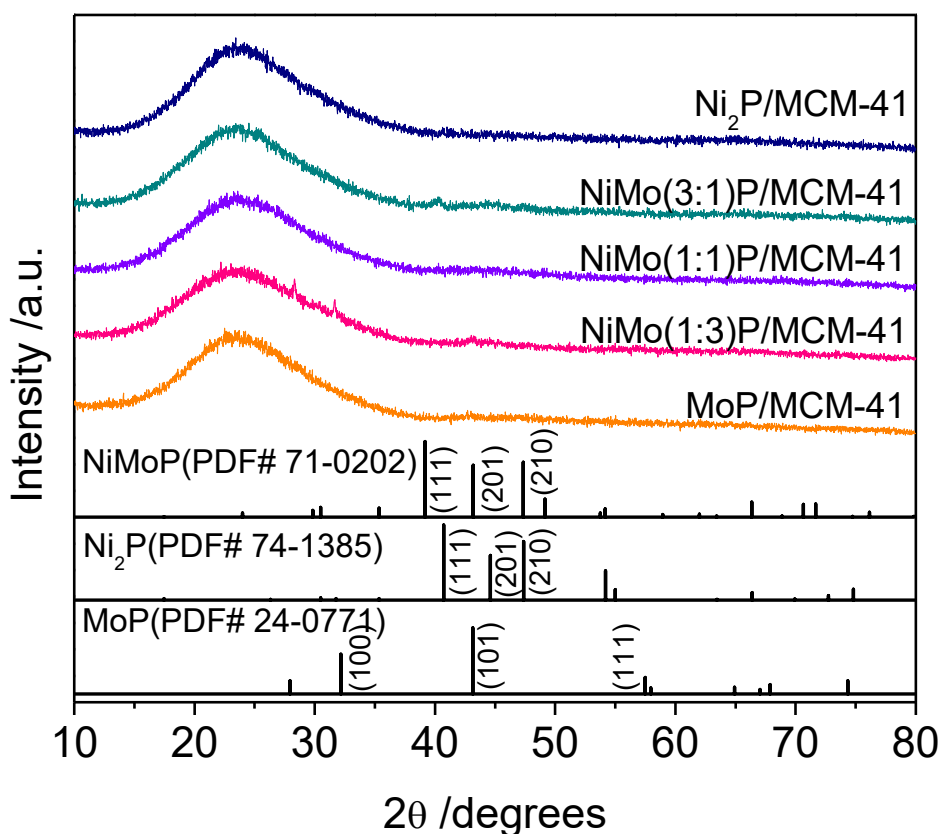


Figure 3.2. Powder XRD patterns for phosphide catalysts at wide-angle (2θ : $10\text{-}80^\circ$, step size: 0.02, scanning rate: 1.0 step/s, repeats: 3 times)

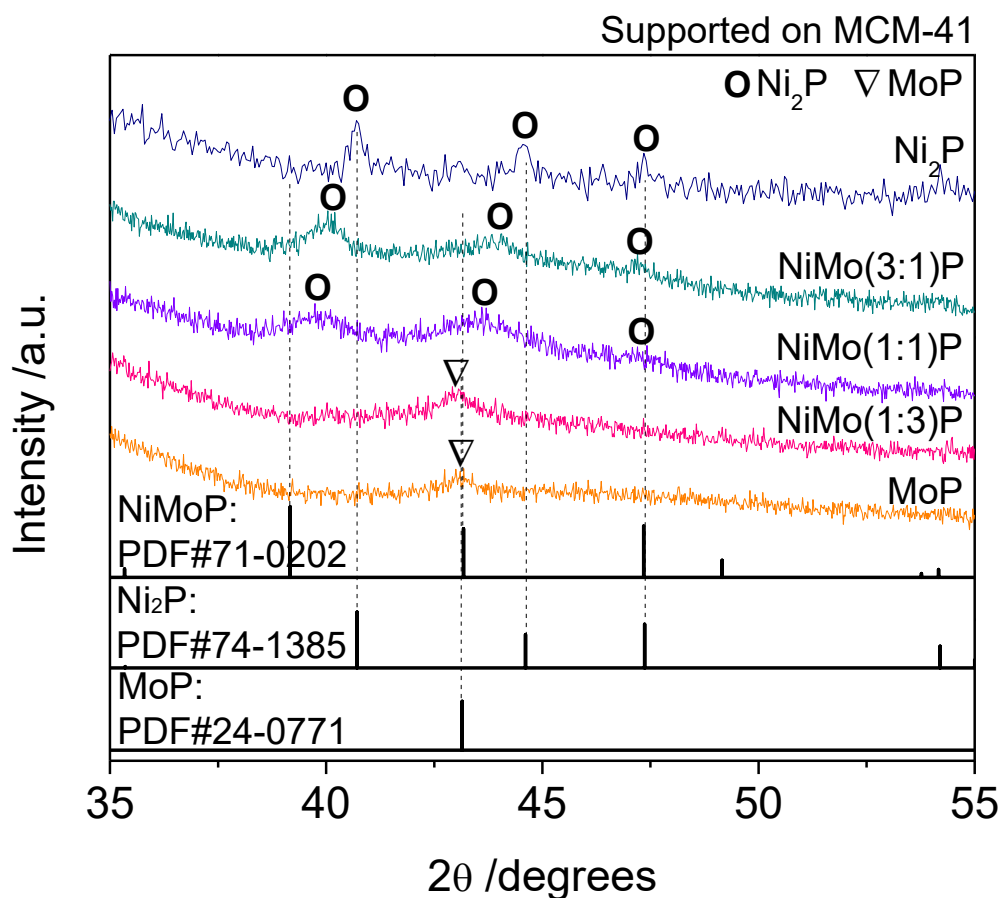


Figure 3.3. Powder XRD patterns for phosphide catalysts at narrow angle (2θ : 35-55°, step size: 0.02, scanning rate: 0.1 step/s, repeats: 5 times) ○ Peaks due to (111), (201) and (210) reflections of the $\overline{P6}2m$ group ▽ Peak due to (101) reflection of the $\overline{P6}m2$ group. Shifts indicate alloy formation.

To augment the signal, the XRD measurements were repeated over a narrower 2θ range of 35 - 50° with slower scanning rate of 0.1 step/s as shown in Fig. 3.3. Overall, the intensity was slightly improved and some peaks became visible. The Ni-rich samples such as $\text{Ni}_2\text{P}/\text{MCM-41}$, $\text{NiMo}(3:1)\text{P}/\text{MCM-41}$, and $\text{NiMo}(1:1)\text{P}/\text{MCM-41}$ presented a series of peaks corresponding to the (111), (201), and (210) reflections which gradually shifted to lower angle from the positions for Ni_2P toward those of NiMoP , consistent with the formation of alloys. The Mo-rich sample shows the (101)

reflection of MoP also shifted to lower angle. The driving force for the formation of the alloys is the increase in entropy due to atomic mixing, and it is surmised, a favorable heat of mixing of Ni and Mo as evidenced by the formation of compounds rather than separate phases, as well as the enthalpy of mixing of the pure metals [46]. In addition, the reduction peaks are shifted to higher temperatures than the pure Ni₂P and MoP. The XRD peaks of NiMo(1:1)P/MCM-41 sample did not quite reach those of NiMoP, and this could have been due to the interactions of the Ni component in the small crystallites with the silicious support. Nickel silicates have high heats of formation ($\Delta H_f = -1396$ kJ mol⁻¹ [47]), and are more stable than Mo silicates. Calculations by DFT show that Ni interacts much more strongly than Mo with the surface of oxidic supports [48]. The Mo-rich NiMo(1:3)P/MCM-41 sample showed a peak close to the (101) reflection of MoP, but shifted slightly to lower angle, consistent with the smaller radius of metallic Ni (0.125 nm) compared to metallic Mo (0.139 nm). Again the shift is consistent with solid solution formation. In this case a crystal structure closer to MoP is obtained, and although the crystal structure is different from that of Ni₂P and NiMoP, it has been pointed out that the building blocks remain the same, trigonal prisms where a P atom is surrounded by six metal atoms [33], so the changes in crystal structure are unlikely to change the alloy nature of the materials. The structure of NiMoP is hexagonal and is isomorphic with that of Ni₂P [43] with similar crystallographic index a, but considerably larger index c. This explains why the (101) and (201) reflexions above are shifted to lower angle but the (210) reflexion is hardly displaced. These consistent variations in the XRD patterns give evidence for the formation of the Ni and Mo alloy.

Table 3.3. Lattice parameters for the catalyst samples Ni₂P/MCM-41, NiMoP(3:1)/MCM-41, and NiMoP(1:1)/MCM-41 samples

2 θ /degree	(hkl)	d _{hkl} /nm	Lattice parameter /nm	
			a	c
Ni ₂ P crystal (PDF#74-1385)				
40.72	(111)	0.2213	0.5857	0.3380
44.61	(201)	0.2029		
47.36	(210)	0.1917		
Ni ₂ P/MCM-41				
40.70	(111)	0.2214	0.5860	0.3384
44.57	(201)	0.2031		
47.34	(210)	0.1918		
NiMo(3:1)P/MCM-41				
40.04	(111)	0.2249	0.5879	0.3485
44.04	(201)	0.2054		
47.17	(210)	0.1925		
NiMo(1:1)P/MCM-41				
39.78	(111)	0.2263	0.5894	0.3539
43.65	(201)	0.2071		
47.05	(210)	0.1929		

Table 3.3 summarizes the lattice parameters for the samples calculated from the XRD peak positions of the (111), (201), and (210) planes in the various samples. In the NiMoP samples of high Ni content (NiMo(3:1)P/MCM-41 and NiMo(1:1)P/MCM-41) the a- and c-lattice parameters were larger than those in the Ni₂P crystal. As Mo content increased, the lattice parameters gradually increased. This trend is consistent with Vegard's law, indicating that Ni is likely to be homogeneously substituted with alloy formation between Ni and Mo phosphide.

Table 3.4. Characterization of fresh and spent catalyst samples

Sample	Condition	BET surface area /m ² g ⁻¹	CO uptake /μmol g ⁻¹
MCM-41	As received	997	-
Ni ₂ P/MCM-41	Fresh	663	70
	Spent	651	67
NiMo(3:1)P/MCM-41	Fresh	604	53
	Spent	598	49
NiMo(1:1)P/MCM-41	Fresh	587	51
	Spent	561	48
Ni ₂ P/MCM-41+MoP/MCM-41	Fresh	602	72
NiMo(1:3)P/MCM-41	Fresh	551	56
	Spent	541	51
MoP/MCM-41	Fresh	539	74
	Spent	521	71

Table 3.4 shows the BET surface areas and CO uptakes of the fresh and spent metal phosphide catalysts. The fresh samples are the reduced samples. The surface area of the phosphide catalysts were lower than that of the pure MCM-41 support because of sintering during the heating steps of the preparation procedure, as well as the reduction in the pore volume due to the presence of the phosphide. The surface area of the fresh catalysts decreased in the order: Ni₂P/MCM-41 > NiMo(3:1)P/MCM-41 > NiMo(1:1)P/MCM-41 > NiMo(1:3)P/MCM-41 > MoP/MCM-41. The surface area decreased with increasing Mo content, possibly because the interactions between the Ni and Mo required higher reduction temperatures, and this led to sintering. The CO uptakes of the fresh catalysts were between 51 and 74 μmol/g, with the monometallic phosphides showing higher uptake values than the NiMoP/MCM-41 catalysts. After the reactivity testing over the various temperatures indicated before, the surface area and CO uptakes did not change significantly indicating that the catalysts did not sinter during the reaction.

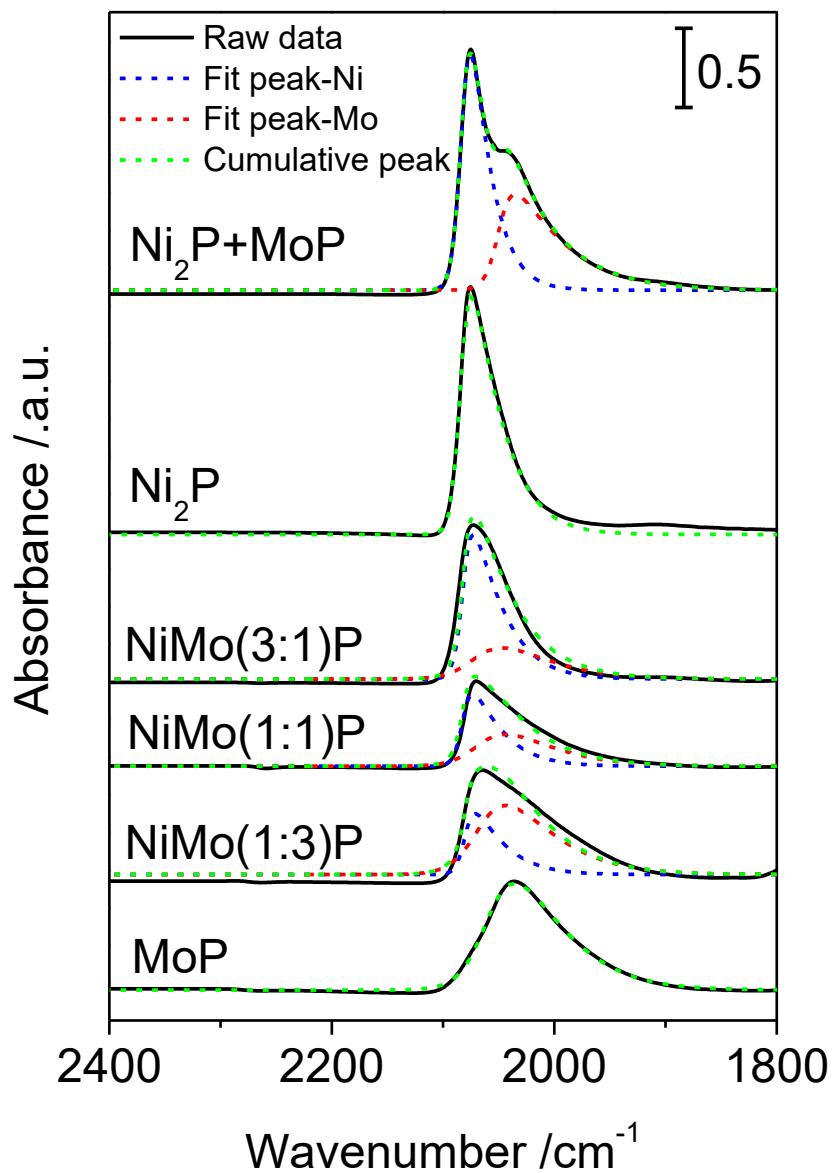


Figure 3.4. IR spectra of CO adsorbed on Ni₂P/MCM-41, NiMo(3:1)P/MCM-41, NiMo(1:1)P/MCM-41, physical mixture of Ni₂P/MCM-41 and MoP/MCM-41, NiMo(1:3)P/MCM-41, and MoP/MCM-41 at 50 °C under N₂ flow after reduction at 550 °C under H₂ flow for 2 h

Fig. 3.4 shows the infrared (IR) spectra of CO adsorbed on the phosphide catalysts at 50 °C under N₂ flow. Before the measurements, the catalyst samples were reduced under H₂ flow at 550 °C for 2 h in the same manner as for the activity tests. For comparison, a physical mixture sample of Ni₂P/MCM-41 (10 mg) and MoP/MCM-41

(10 mg) was also measured. Characteristic IR bands were observed for Ni₂P/MCM-41 and MoP/MCM-41 at 2075 and 2036 cm⁻¹, respectively, which can be assigned to linearly bonded CO on metal sites on reduced samples [49, 50]. The Ni₂P signal at higher wavenumber was narrower and had higher intensity, while the MoP signal at lower wavenumber was broader and had a tail. As expected, the physical mixture sample presented a combined signal, which could be deconvoluted into a combination of the two main Ni₂P and MoP peaks. The alloy NiMoP/MCM-41 catalyst samples presented broad asymmetric IR bands with features similar to those of the Ni₂P and MoP, with a rapidly rising signal on the left and a broad band with a tail on the right. However, the overall signal is not exactly a weighted sum of the respective spectra, indicating that there were small interactions between the components. The peak positions of Ni sites are slightly shifted toward lower wavenumbers with increasing Mo content. These occur at 2075 cm⁻¹ for Ni₂P/MCM-41, 2073 cm⁻¹ for NiMo(3:1)P/MCM-41, 2073 cm⁻¹ for NiMo(1:1)P/MCM-41, and 2071 cm⁻¹ for NiMo(1:3)P/MCM-41. Generally, shifts to a lower frequency are explained by stronger electron back-donation to the antibonding 2π* molecular orbitals of the linearly coordinated CO molecules which lowers the C-O bond strength and vibrational frequency, but this is a secondary effect [51]. In this case the shift to lower frequency is likely to be due to increased σ bonding from donation of the electron lone pair on carbon to Ni p or d orbitals, which is a primary effect as the Ni becomes more electron deficient with Mo incorporation. It can also be due to a dilution effect on dipole-dipole interactions of the CO molecules [50]. The consistent increasing shift with Mo content is also evidence for alloy formation.

The signal was fitted to a sum of asymmetric functions. The weighted sum of the Ni₂P and MoP spectra reported in Table 5. The factors a and b were estimated from the following equation:

$$\text{NiMo}(x:y)\text{P} = a \times (\text{Ni}_2\text{P})_{IR} + b \times (\text{MoP})_{IR}$$

Where NiMo(x:y)P describes the area of the FTIR spectra and (Ni₂P)_{IR} and (MoP)_{IR} are areas of deconvoluted asymmetric spectra. The quantity of Ni sites can be calculated by multiplying the total CO uptake and the factor a/(a+b). The quantity a/(a+b) was close to the Ni composition, indicating that there was no surface enrichment in the alloys. For example, the number of Ni site on NiMo(1:1)P/MCM-41 was 25 μmol g⁻¹ which was as expected from the equimolar composition of Ni and Mo.

Table 3.5. Factor analysis of IR spectra

Sample	a	b	a/(a+b)	Ni site /μmol g ⁻¹	Mo site /μmol g ⁻¹
Ni ₂ P/MCM-41	1	0	1	70	-
NiMo(3:1)P/MCM-41	0.61	0.29	0.67	35.7	17.3
NiMo(1:1)P/MCM-41	0.3	0.3	0.50	25.7	25.3
Ni ₂ P+MoP/MCM-41	0.92	0.84	0.52	37.6	34.4
NiMo(1:3)P/MCM-41	0.26	0.65	0.28	15.8	40.2
MoP/MCM-41	-	1	0	-	74

Fig. 3.5 shows the normalized Ni K-edge XANES spectra for Ni₂P/MCM-41, NiMo(3:1)P/MCM-41, NiMo(1:1)P/MCM-41, and NiMo(1:3)P/MCM-41, with the adsorption edge position, E₀, indicated by vertical lines. Variation of charge distribution leads to changing of the chemical environment of the absorbed atom, and therefore, the absorption edge shifts in the XANES because the core-level energies are

altered. The shifts of E_0 to higher energies as the Mo concentration increased can be explained by electron transfer from Ni to Mo. This is because E_0 is the energy required to excite the core electron to an unoccupied valence band. The direction of electron transfer is consistent with the larger Pauling electronegativity of Mo (2.16) compared to Ni (1.91), and agrees with previous X-ray photoelectron spectroscopy characterization of Ni-Mo-P materials which indicate electron transfer from Ni to Mo as well as from the metals to P [27]. In addition, DFT calculations of atomic charge in NiMoP shows the charge on Ni to be less negative than in Ni_2P and the charge on Mo to be more negative than in MoP, again suggesting electron transfer from Ni to Mo [52]. The consistent variations of edge position with Mo content are evidence for alloy formation.

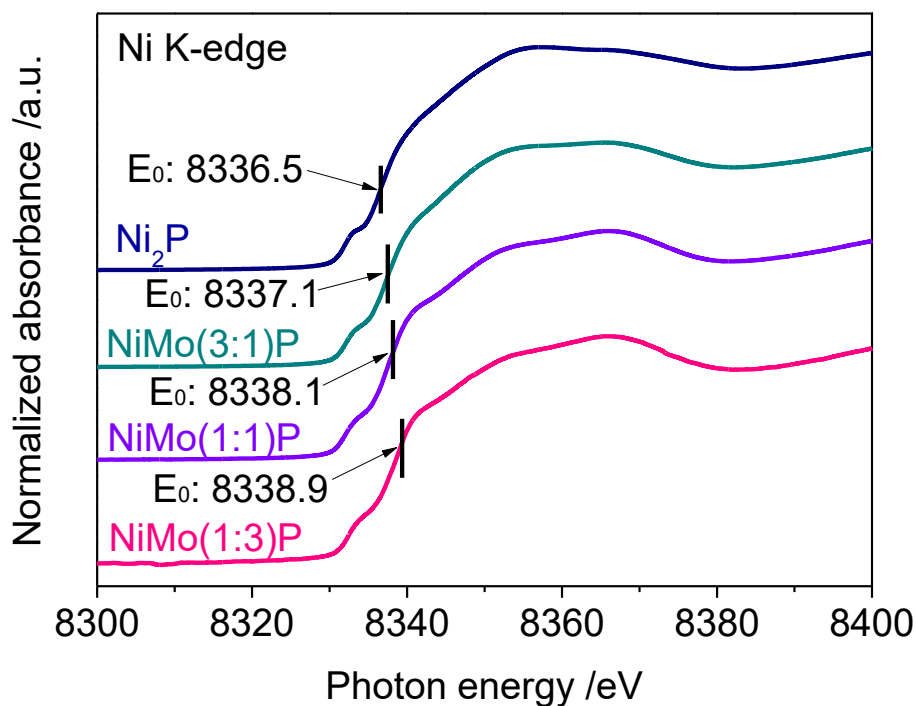


Figure 3.5. Normalized Ni K-edge XANES spectra for Ni_2P /MCM-41, NiMo(3:1)P/MCM-41, NiMo(1:1)P/MCM-41, and NiMo(1:3)P/MCM-41. The spectra were obtained at room temperature after reduction at 550 °C for 3 h with H_2 flow (50 ml/min). The edge energy, E_0 , was defined as the zero intercept of the second XANES derivative.

3.3.2 Reactivity studies

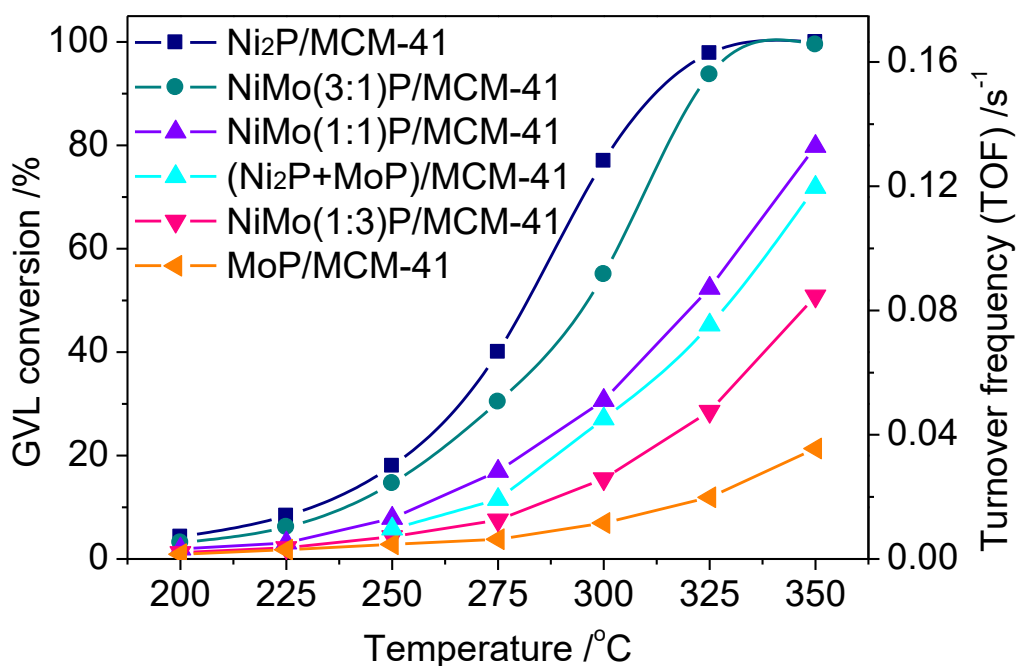


Figure 3.6. GVL conversion and turnover frequency (right scale) as a function of temperature at equal number of active site ($10 \mu\text{mol}$) at 0.5 MPa with 2 mol\% GVL in H_2

The conversions of GVL and turnover frequency (right axis) as a function of temperature at 0.5 MPa over the phosphide catalysts are shown in Fig. 3.6. Both the conversion and TOF follow the same points and curves because the amount of catalyst used corresponds to the same number of surface site of $10 \mu\text{mol}$, as titrated by CO chemisorption. The TOF was obtained directly from the conversion, at conditions where there were no mass transfer limitations (*vide infra*), but included medium conversions ($< \sim 40\%$) where adsorption of products on the surface could start reducing rates. They were not obtained from rate constants, because that would entail knowing the effect of these products, e.g. the kinetics of the reaction. The most accurate rates are obtained in the differential regime, where conversion ($< \sim 10\%$) would be proportional to space time.

The GVL conversion and TOF increased with reaction temperature, as expected, and followed the order: Ni₂P/MCM-41 > NiMo(3:1)P/MCM-41 > NiMo(1:1)P/MCM-41 \cong physical mixture > NiMo(1:3)P/MCM-41 > MoP/MCM-41, indicating that the conversion was highest for the catalysts with the highest amounts of Ni. The NiMo(1:1)P/MCM-41 catalyst had a conversion that was very close to that of the 1:1 physical mixture of Ni₂P/MCM-41 and MoP/MCM-41. The results indicated that Ni is the active site while Mo acts as a diluent.

In order to verify that mass transfer limitations were not affecting the low conversion results, the Weisz-Prater criterion C_{WP} was calculated by the following equation [53, 54]:

$$C_{WP} = \frac{\text{Reaction rate}}{\text{Diffusion rate}} = \frac{-r'_{A(\text{obs})} \rho_c R^2}{D_e C_{As}}$$

The observed reaction rate $-r'_{A(\text{obs})}$, and the Weisz-Prater criterion C_{WP} are summarized in Table 3.6. The quantities used in the calculations are shown in Table S1 of the Supplementary Information. In general, conversion versus temperature curves depict an S-shaped curve as shown by the data for Ni₂P/MCM-4 in Fig. 3.6. The inflection point of the S-curve marks the onset of mass transfer limitations (mass availability), where the rate of increase of conversion no longer rises exponentially with temperature. The rate of the reaction should continue to increase following an Arrhenius temperature dependence, but the consumption of reactant limits the rate with the reaction completely starved of reactant as full conversion is reached. This is different from diffusional limitations. The points of inflexion indicate that mass transfer limitations start to intrude at 300 °C for Ni₂P and at higher temperatures for the others

samples. Calculations of the Weisz-Prater criterion support this observation as shown by the values of C_{wp} in Table 3.6. At low conversions (shaded blue) the C_{wp} values are below 0.3 indicating that the rates are in the kinetic regime, but in the high conversion region over 40-50 % (shaded red), the values of C_{wp} are over 0.3 indicating mass transfer limitations.

Table 3.6. Observed reaction rates and calculated Weisz-Prater criterion

Sample	Ni ₂ P	NiMo(3:1)P	NiMo(1:1)P	NiMo(1:3)P	MoP
Temp. /°C	Observed reaction rate /mol g ⁻¹ s ⁻¹				
200	3.46E-07	2.73E-07	1.68E-07	1.06E-07	7.95E-08
225	7.24E-07	5.35E-07	3.55E-07	1.88E-07	1.29E-07
250	1.56E-06	1.27E-06	6.81E-07	3.72E-07	2.02E-07
275	3.47E-06	2.54E-06	1.47E-06	6.52E-07	3.30E-07
300	6.66E-06	4.77E-06	2.65E-06	1.34E-06	6.02E-07
325	8.55E-06	8.11E-06	4.53E-06	2.47E-06	1.03E-06
350	8.65E-06	8.61E-06	6.91E-06	4.40E-06	1.85E-06
Temp. /°C	Weisz-Prater criterion				
200	0.017	0.013	0.008	0.005	0.004
225	0.036	0.027	0.018	0.009	0.007
250	0.082	0.067	0.036	0.020	0.011
275	0.192	0.141	0.081	0.036	0.018
300	0.386	0.276	0.154	0.078	0.035
325	0.517	0.490	0.274	0.149	0.062
350	0.545	0.542	0.435	0.277	0.116

The conversion results indicated that the conversion was higher for samples with higher Ni content. Thus, it was of interest to calculate turnover frequencies based on Ni sites, as measured earlier by adsorption and FTIR.

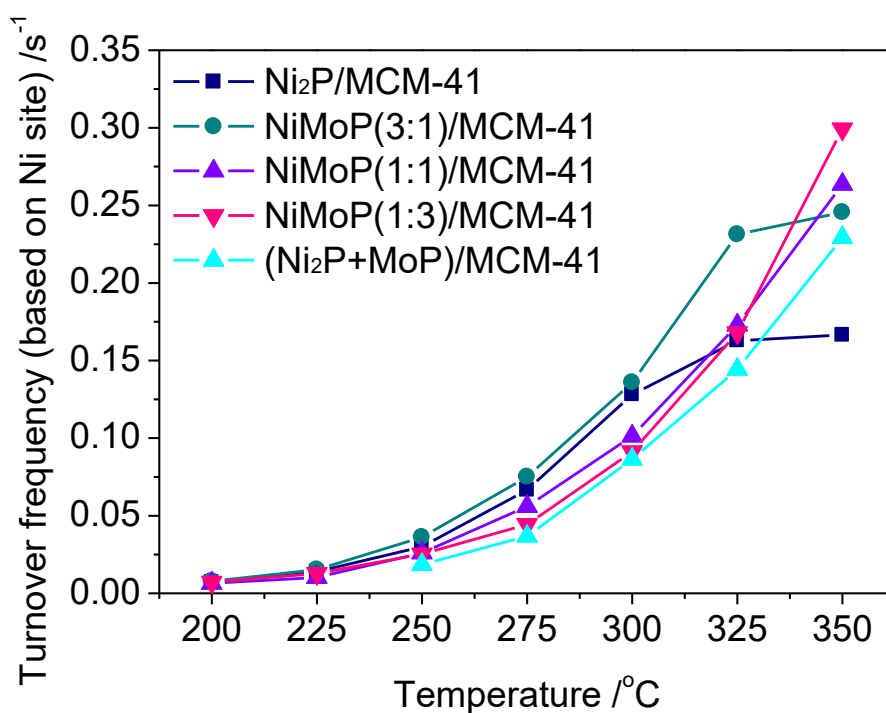


Figure 3.7. Turnover frequency based on Ni sites as a function of temperature at 0.5 MPa

Fig. 3.7 shows the turnover frequencies of the various catalysts based on Ni sites (TOF) as a function of temperature at 0.5 MPa. In contrast to the results in Fig. 3.6, the turnover frequencies did not vary appreciably with metal composition, consistent with the observation that activity tracked the Ni content. For the samples, Ni₂P/MCM-41 and NiMo(3:1)P/MCM-41, the TOF leveled off at higher temperature because of mass transfer limitation. The TOF results indicate that there was no substantial improvement with alloying, confirming the dominance of Ni sites in the catalytic activity of NiMoP/MCM-41 catalysts. Since the Mo content is unimportant, another inference is that the connectivity of atoms in the alloy is inconsequential for the activity, and that the reaction is structure-insensitive. Such a lack of dependence of activity with alloying has been documented in many cases, and is a classical definition of facile or structure-

insensitive reactions [55]. Although the TOF values were close, their order still followed the Ni content: $\text{Ni}_2\text{P} \sim \text{NiMo}(3:1) > \text{NiMo}(1:1) > \text{NiMo}(1:3) > \text{MoP}$, indicating a very slight preference for proximal Ni sites, and it is conjectured that a pair of adjacent Ni sites might be involved in the reaction.

The conversion, TOF, product selectivity, C4 hydrocarbons/CO mole ratio and carbon balance at 250, 300 and 350 °C and 0.5 MPa are summarized in Table 3.7. The results for MoP/MCM-41 are reported at 275 °C owing to the low activity at 250 °C. The products were classified into four groups: C4 (n-butenes, butane), C5 (n-pentadienes, n-pentenes, pentane), C5-O (2-methyltetrahydrofuran, pentanal, 1-pentanol, 2-pentanone, 2-pentanol), and C5-O2 (pentanoic acid, n-pentenoic acids). At 250 °C, all catalysts produced mainly C5-O2 products, but the bimetallic phosphide catalysts produced higher amounts of C5-O compounds than the pure Ni_2P or MoP catalysts, although the $\text{NiMo}(1:3)$ had just a slight increase. Especially, the $\text{NiMo}(1:1)\text{P}/\text{MCM-41}$ catalyst presented the highest C5-O selectivity. At 300 °C, many of the oxygen containing compounds were converted to C4 and C5 hydrocarbons. At this temperature the main products were still C5-O2 products, but this is because the conversions are still moderate. At 350 °C, at the higher conversions the products are C4 and C5 hydrocarbons. In general, the selectivity to deoxygenated products was low at the lower temperatures because the conversion was small, and the reaction is sequential with oxygenated products formed first. If longer contact times were used, selectivity would move to the deoxygenated products.

The ($\text{Ni}_2\text{P}+\text{MoP}$) mixture showed a more similar behavior to $\text{Ni}_2\text{P}/\text{MCM-41}$ in relation to product selectivity than the $\text{NiMo}(1:1)\text{P}$ alloy, because in the mixture the Ni_2P component was more active than the MoP portion and dominated the reactivity.

For example, the n-butane selectivity of both the physical mixture and the pure Ni₂P are high at all temperatures. The C₄/CO mole ratio for all catalysts was close to 1.0. The formation of CO₂ was not detected, indicating that C₄ hydrocarbons were mainly formed by decarbonylation. The carbon balance was within error range (100 % ± 5 %) on all catalysts at 250, 300, and 350 °C. A possible decarbonylation pathway with production of butane is shown in Fig. 3.8. The scheme depicts the involvement of a pair of Ni atoms in the reaction, as concluded from the slight dependence of TOF on Ni content. It is also consistent with the adsorption of CO on Ni observed at similar reaction temperatures in related studies [56, 57], albeit only at room temperature in this study. In the scheme, surface phosphorus is depicted to be associated with oxygen because P is oxyphilic and has been shown to form OH groups in the presence of water [58]. Additional reaction steps are not shown because of the absence of contact time experiments in this work.

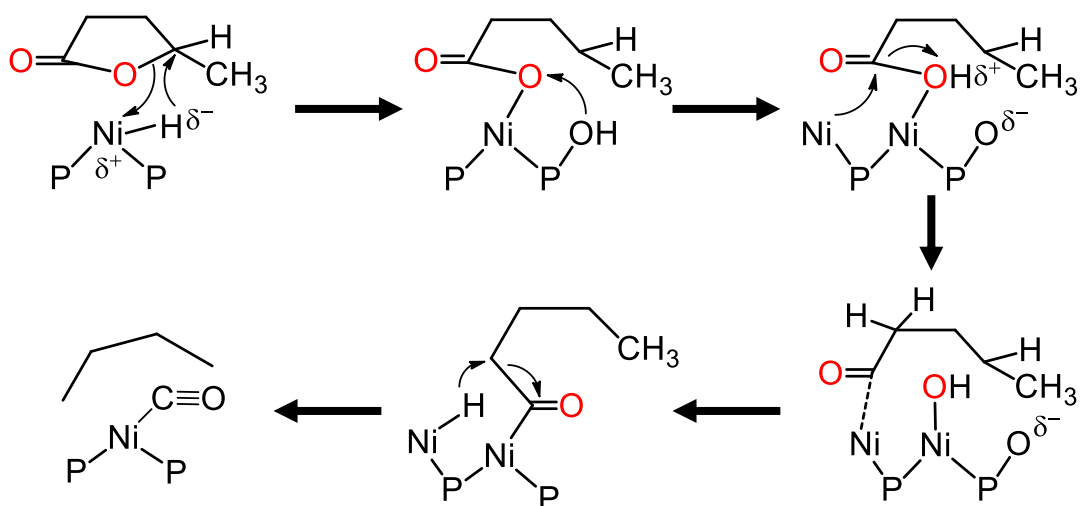


Figure 3.8. A proposed decarbonylation pathway with production of butane

Table 3.7. GVL conversion, TOF, selectivity, mole ratio C4/CO and carbon balance at 250, 300 and 350 °C at 0.5 MPa

Temp. /°C	Sample	Conv. /%	TOF /s ⁻¹	Product selectivity /%				C4/CO ^a	CB ^b /%
				C4	C5	C5O	C5O2		
250	Ni ₂ P/MCM-41	18	0.030	21.9	1.0	3.8	73.3	1.04	102
	NiMo(3:1)P/MCM-41	14	0.024	8.3	2.5	15.2	74.0	1.06	98
	NiMo(1:1)P/MCM-41	8	0.013	3.8	4.4	35.9	55.8	1.02	96
	(Ni ₂ P+MoP)/MCM-41 ^c	6	0.010	14.5	1.6	4.7	79.1	1.01	101
	NiMo(1:3)P/MCM-41	4	0.007	0.5	1.1	4.8	93.6	1.10	97
275	MoP/MCM-41	14	0.006	0.8	0.7	3.7	94.8	1.00	103
300	Ni ₂ P/MCM-41	77	0.128	67.8	1.3	2.5	28.4	1.09	101
	NiMo(3:1)P/MCM-41	55	0.092	34.1	6.9	15.6	43.4	1.01	97
	NiMo(1:1)P/MCM-41	31	0.051	16.6	10.7	15.5	57.3	1.02	96
	(Ni ₂ P+MoP)/MCM-41 ^c	27	0.045	45.6	2.6	5.2	46.5	1.03	100
	NiMo(1:3)P/MCM-41	16	0.026	6.4	7.3	9.1	77.2	1.02	98
	MoP/MCM-41	7	0.012	8.4	12.4	14.1	65.1	1.01	100
350	Ni ₂ P/MCM-41	100	0.167	98.2	1.4	0.3	0.1	1.02	97
	NiMo(3:1)P/MCM-41	99	0.166	85.2	9.8	1.4	3.6	1.04	101
	NiMo(1:1)P/MCM-41	80	0.133	45.4	14.6	11.1	28.9	1.06	96
	(Ni ₂ P+MoP)/MCM-41 ^c	72	0.120	67.7	5.4	3.5	23.5	1.02	99
	NiMo(1:3)P/MCM-41	51	0.085	23.8	21.0	11.0	44.2	1.01	103
	MoP/MCM-41	21	0.036	17.5	19.4	17.1	45.9	1.01	97

C4 (n-butenes, butane), C5 (n-pentadienes, n-pentenenes, pentane), C5-O (2-methyltetrahydrofuran, pentanal, 1-pentanol, 2-pentanone, 2-pentanol), C5-O2 (pentanoic acid, n-pentenoic acids)

a Mole ratio (C₄H₁₀+C₄H₈)/CO

b Carbon balance calculated by $\left(\frac{\sum(\text{carbon number} \times n_{\text{product}})}{5 \times n_{\text{GVL}}}\right)$

c Physical mixture of Ni₂P/MCM-41 and MoP/MCM-41

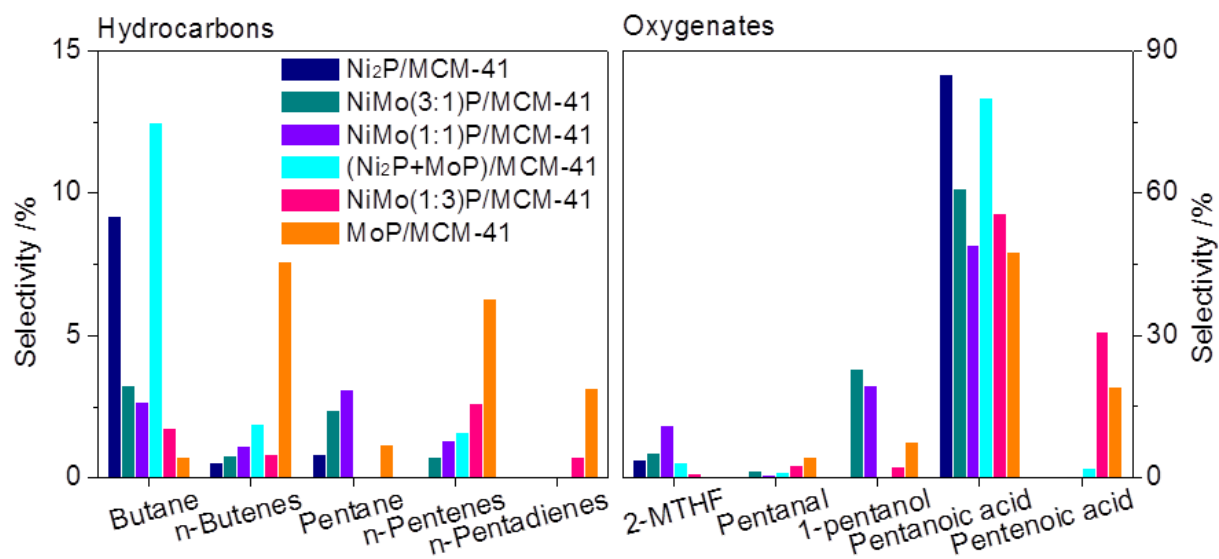


Figure 3.9. Product selectivity for HDO of GVL at around 8 % of conversion (8 % at 225 °C on Ni₂P/MCM-41, 6 % at 225 °C on NiMo(3:1)P/MCM-41, 8 % at 250 °C on NiMo(1:1)P/MCM-41, 6 % at 250 °C on physical mixture of Ni₂P/MCM-41 and MoP/MCM-41, 8 % at 275 °C on NiMo(1:3)P/MCM-41 and 7 % at 300 °C on MoP/MCM-41)

Fig. 3.9 shows the product selectivity from the HDO of GVL at around 8 % of conversion (8 % at 225 °C on Ni₂P/MCM-41, 6 % at 225 °C on NiMo(3:1)P/MCM-41, 8 % at 250 °C on NiMo(1:1)P/MCM-41, 6 % at 250 °C on (Ni₂P+MoP)/MCM-41, 8 % at 275 °C on NiMo(1:3)P/MCM-41 and 7 % at 300 °C on MoP/MCM-41). Ideally, constant conversion should have been obtained by varying the space-time at the same temperature, and the comparison here is thus an approximation. The comparison is justified because the temperature range was not that high, and the slow step was structure-insensitive on all catalysts. The products were categorized into two groups: hydrocarbons (butane, n-butenes, pentane, n-pentenes and n-pentadienes) and oxygenates (2-MTHF, pentanal, 1-pentanol, pentanoic acid and pentenoic acid). The selectivity to 2-pentanone and 2-pentanol is not shown in the result because of their low selectivity (below 1 %). The 2-pentanone and 2-pentanol products arise from the

cleavage of the C-O bond next to the methyl group and their selectivity is much lower than the selectivity of 2-MTHF + pentanal + 1-pentanol. In contrast to the TOF results, the selectivity to the main products did change considerably with metal composition, especially as pertaining to the selectivity to hydrocarbons. All the catalysts produced mostly pentanoic acid and some 2-MTHF, pentanal and 1-pentanol. This tendency to produce oxygenates is not an indication that the phosphides are not good HDO catalysts, but rather that the initial products formed at low conversion (< 10%) still contain oxygen. The NiMo(1:1)P/MCM-41 catalyst presented a high tendency to produce 1-pentanol (14 %). On the other hand, the Ni₂P/MCM-41 and (Ni₂P+MoP)/MCM-41 catalysts produced only small amounts of 1-pentanol (below 0.1 %). Overall, the bimetallic phosphide catalysts displayed higher selectivity to 1-pentanol compared to Ni₂P/MCM-41 and the physically mixed catalyst indicating that the bimetallic phosphide catalysts enhanced hydrogenation of pentanal to 1-pentanol. The selectivity to hydrocarbons for monometallic Ni₂P/MCM-41 differed from that for MoP/MCM-41: the former produced mainly butane (9 %), while the latter produced mainly unsaturated hydrocarbons such as n-butenes (8 %) and n-pentenes (6 %). This is reflective of the higher hydrogenation capability of Ni sites over Mo sites. The bimetallic phosphides also showed a higher selectivity to pentane. Furthermore, increase in Mo content led to higher production of C5 hydrocarbons. The results can be understood by the diminished tendency to undergo decarbonylation from the decreased amount of Ni. In previous work [37], C4 hydrocarbons (butane and n-butenes) and C5 hydrocarbons (pentane, n-pentenes and n-pentadienes) were produced by decarbonylation and hydrodeoxygenation (HDO), respectively. Therefore, the presence of Mo favors the formation of C5 hydrocarbons compared to Ni₂P/MCM-41.

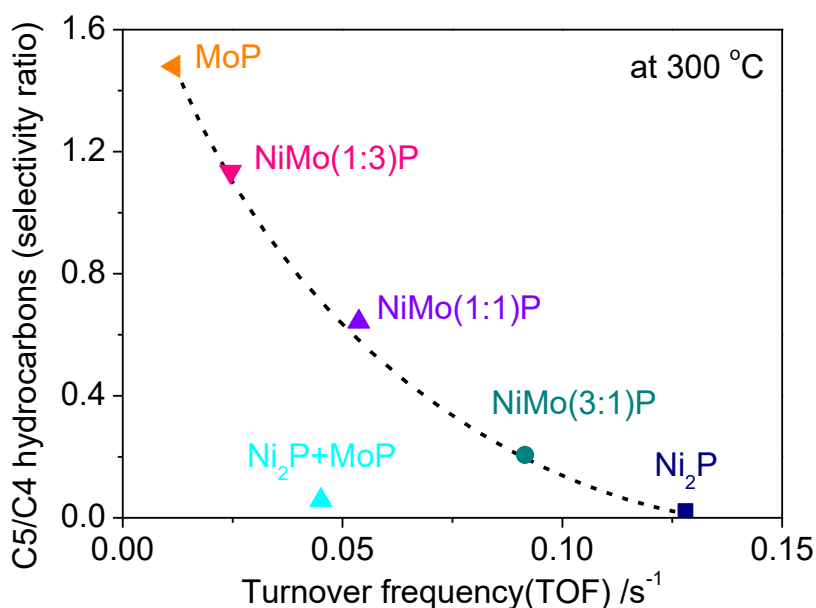


Figure 3.10. C5/C4 hydrocarbons selectivity ratio as a function of turnover frequency (TOF) on Ni₂P/MCM-41, NiMo(3:1)P/MCM-41, NiMo(1:1)P/MCM-41, physical mixture of Ni₂P/MCM-41 and MoP/MCM-41, NiMo(1:3)P/MCM-41 and MoP/MCM-41 at 300 °C and 0.5 MPa

Fig. 3.10 shows the C5/C4 hydrocarbons selectivity ratio as a function of turnover frequency (TOF) over the phosphide catalysts at 300 °C. With Ni addition, the C5/C4 hydrocarbons selectivity ratios decreased while the TOFs increased. These results demonstrated that while increase in Ni content enhanced activity, this was partly offset by a diminished selectivity towards C5 hydrocarbons. In terms of product value the offset is partial because the CO formed with the C4 hydrocarbons represents a valuable product. The CO can undergo water-gas shift to produce H₂. The values of TOF and C5/C4 hydrocarbons selectivity ratio were between those of the monometallic Ni₂P/MCM-41 and MoP/MCM-41 catalysts, indicating that while the proportion of Ni sites in the catalyst governed the activity, the Mo sites controlled the selectivity to C5 hydrocarbons. An alternative explanation is that there are mixtures of NiMoP and Ni₂P

or MoP with the NiMoP displaying a distinct behavior, but this would seem to be more complicated (violating Occam's razor) and contrary to the evidence for the formation of solid solutions. These results provide insights into the behavior of Ni and Mo sites during the HDO of γ -GVL: the Ni and Mo sites behaved independently, and as a result the HDO of GVL is structure-insensitive with regards to activity, but structure-sensitive with respect to selectivity. Interestingly, the NiMo(1:1)P/MCM-41 catalyst presented a higher C5/C4 hydrocarbon selectivity ratio than the physical mixture of Ni₂P/MCM-41 and MoP/MCM-41 as shown in Fig. 3.11. This is because the reactivity of the NiMo(1:1)P alloy is dominated by the Ni and the selectivity is affected by the Mo. Thus, the formation of Ni-Mo led to only a slight ligand effect between the individual Ni and Mo sites in terms of activity.

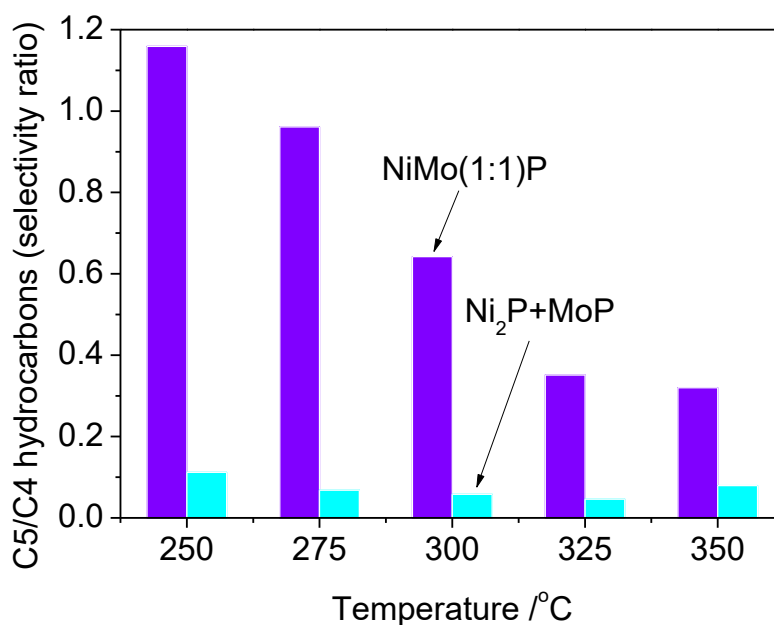


Figure 3.11. C5/C4 hydrocarbons (selectivity ratio) as a function of temperature on NiMo(1:1)P/MCM-41 and physical mixture of Ni₂P/MCM-41+MoP/MCM-41 at 0.5 MPa

3.4 Conclusions

A series of supported bimetallic phosphides was prepared by temperature-programmed reduction of phosphite precursors and tested for the hydrodeoxygenation (HDO) of γ -valerolactone (GVL). Highly dispersed bimetallic phosphide catalysts were successfully synthesized, which were characterized by N_2 physisorption, X-ray diffraction (XRD), CO-chemisorption, and fourier transform infrared spectroscopy (FTIR). The formation of Ni and Mo alloy was confirmed by shifts of diffraction peak positions from XRD patterns and edge positions in X-ray absorption near-edge spectra. Infrared (IR) spectra of CO adsorbed on phosphide catalysts showed a single broad peak. However, deconvolution of the IR spectra of the bimetallic phosphide catalysts revealed contributions from Ni and Mo sites; consequently, the number of Ni active sites was estimated by factor analysis of the deconvoluted peaks and the CO uptake values obtained from chemisorption measurements. The activity was related to the proportion of Ni in the catalyst, following the order: $Ni_2P/MCM-41 > NiMo(3:1)P/MCM-41 > NiMo(1:1)P/MCM-41 \cong (Ni_2P+MoP)/MCM-41 > NiMo(1:3)P/MCM-41 > MoP/MCM-41$, indicating that Ni was the major active site, while Mo was a diluent with respect to activity. This interpretation was confirmed by results of TOF normalized by accessible Ni sites which revealed that the effect of alloying on the activity was small, with TOF only slightly more elevated at higher Ni content. It is concluded that a pair of Ni atoms are likely involved in the rate-determining step. In contrast to the TOF results, the presence of Mo sites had a significant effect on the product selectivity: $Ni_2P/MCM-41$ mostly produced butane, whereas Mo-containing catalysts produced higher amount of 1-pentanol and C5 hydrocarbons such as pentane and n-pentenes. These results demonstrate that the product selectivity was strongly affected by the neighboring atoms of Ni.

References

- [1] J. Zhang, K. Wang, M.W. Nolte, Y.S. Choi, R.C. Brown, B.H. Shanks, Catalytic deoxygenation of bio-oil model compounds over acid–base bifunctional catalysts, *ACS Catal.* 6 (2016) 2608-2621.
- [2] G.S. Foo, A.K. Rogers, M.M. Yung, C. Sievers, Steric effect and evolution of surface species in the hydrodeoxygenation of bio-oil model compounds over Pt/HBEA, *ACS Catal.* 6 (2016) 1292-1307.
- [3] A.D. Sutton, F.D. Waldie, R. Wu, M. Schlaf, L.A. Silks, J.C. Gordon, The hydrodeoxygenation of bioderived furans into alkanes, *Nat. Chem.* 5 (2013) 428-432.
- [4] H. Wang, J. Male, Y. Wang, Recent advances in hydrotreating of pyrolysis bio-oil and its oxygen-containing model compounds, *ACS Catal.* 3 (2013) 1047-1070.
- [5] C. Lindfors, E. Kuoppala, A. Oasmaa, Y. Solantausta, V. Arpiainen, Fractionation of bio-oil, *Energy Fuels* 28 (2014) 5785-5791.
- [6] R.C. Nelson, B. Baek, P. Ruiz, B. Goundie, A. Brooks, M.C. Wheeler, B.G. Frederick, L.C. Grabow, R.N. Austin, Experimental and theoretical insights into the hydrogen-efficient direct hydrodeoxygenation mechanism of phenol over Ru/TiO₂, *ACS Catal.* 5 (2015) 6509-6523.
- [7] A.Y. Bunch, U.S. Ozkan, Investigation of the reaction network of benzofuran hydrodeoxygenation over sulfided and reduced Ni–Mo/Al₂O₃ catalysts, *J. Catal.* 206 (2002) 177-187.
- [8] A.V. da Silva Neto, E.R. Leite, V.T. da Silva, J.L. Zotin, E.A. Urquieta-González, NiMoS HDS catalysts – The effect of the Ti and Zr incorporation into the silica support and of the catalyst preparation methodology on the orientation and activity of the formed MoS₂ slabs, *Appl. Catal. A: Gen.* 528 (2016) 74-85.
- [9] F. Pelardy, A. Daudin, E. Devers, C. Dupont, P. Raybaud, S. Brunet, Deep HDS of FCC gasoline over alumina supported CoMoS catalyst: Inhibiting effects of carbon monoxide and water, *Appl. Catal. B: Environ.* 183 (2016) 317-327.
- [10] O.Y. Gutiérrez, S. Singh, E. Schachtl, J. Kim, E. Kondratieva, J. Hein, J.A. Lercher, Effects of the support on the performance and promotion of (Ni)MoS₂ catalysts for simultaneous hydrodenitrogenation and hydrodesulfurization, *ACS Catal.* 4 (2014) 1487-1499.

-
- [11] U.S. Ozkan, L.P. Zhang, S.A. Ni, E. Moctezuma, Characterization and activity of unsupported Ni-Mo sulfide catalysts in HDN/HDS reactions, *Energy Fuels* 8 (1994) 830-838.
- [12] O.İ. Şenol, E.M. Ryymin, T.R. Viljava, A.O.I. Krause, Effect of hydrogen sulphide on the hydrodeoxygenation of aromatic and aliphatic oxygenates on sulphided catalysts, *J. Mol. Catal. A: Chem.* 277 (2007) 107-112.
- [13] G.-N. Yun, Y.-K. Lee, Dispersion effects of Ni₂P catalysts on hydrotreating of light cycle oil, *Appl. Catal. B: Environ.* 150-151 (2014) 647-655.
- [14] S. Oyama, Y.-K. Lee, The active site of nickel phosphide catalysts for the hydrodesulfurization of 4,6-DMDBT, *J. Catal.* 258 (2008) 393-400.
- [15] P. Clark, W. Li, S.T. Oyama, Synthesis and activity of a new catalyst for hydroprocessing: Tungsten phosphide, *J. Catal.* 200 (2001) 140-147.
- [16] V. Zuzaniuk, R. Prins, Synthesis and characterization of silica-supported transition-metal phosphides as HDN catalysts, *J. Catal.* 219 (2003) 85-96.
- [17] N. Koike, S. Hosokai, A. Takagaki, S. Nishimura, R. Kikuchi, K. Ebitani, Y. Suzuki, S.T. Oyama, Upgrading of pyrolysis bio-oil using nickel phosphide catalysts, *J. Catal.* 333 (2016) 115-126.
- [18] A. Iino, A. Cho, A. Takagaki, R. Kikuchi, S. Ted Oyama, Kinetic studies of hydrodeoxygenation of 2-methyltetrahydrofuran on a Ni₂P/SiO₂ catalyst at medium pressure, *J. Catal.* 311 (2014) 17-27.
- [19] A. Takagaki, R. Kikuchi, S.T. Oyama, Transition metal phosphides: New catalysts for deep hydrodeoxygenation, *Shokubai* 55 (2013) 294-299.
- [20] R. Prins, M.E. Bussell, Metal phosphides: Preparation, characterization and catalytic reactivity, *Catal. Lett.* 142 (2012) 1413-1436.
- [21] A.-M. Alexander and J. S. J. Hargreaves, Alternative catalytic materials: carbides, nitrides, phosphides and amorphous boron alloys, *Chem. Soc. Rev.* 39 (2010) 4388-4401.
- [22] S. T. Oyama, T. Gott, H. Zhao, Y.-K. Lee, Transition metal phosphide hydroprocessing catalysts: A review, *Catal. Today* 143 (2009) 94-107.
- [23] R.H. Bowker, M.C. Smith, M.L. Pease, K.M. Slenkamp, L. Kovarik, M.E. Bussell, Synthesis and hydrodeoxygenation properties of ruthenium phosphide catalysts, *ACS Catal.* 1 (2011) 917-922.

-
- [24] H.Y. Zhao, D. Li, P. Bui, S.T. Oyama, Hydrodeoxygenation of guaiacol as model compound for pyrolysis oil on transition metal phosphide hydroprocessing catalysts, *Appl. Catal. A: Gen.* 391 (2011) 305-310.
- [25] L.F. Feitosa, G. Berhault, D. Laurenti, T.E. Davies, V. Teixeira da Silva, Synthesis and hydrodeoxygenation activity of Ni₂P/C – Effect of the palladium salt on lowering the nickel phosphide synthesis temperature, *J. Catal.* 340 (2016) 154-165.
- [26] K. Li, R. Wang, J. Chen, Hydrodeoxygenation of anisole over silica-supported Ni₂P, MoP, and NiMoP catalysts, *Energy Fuels* 25 (2011) 854-863.
- [27] J.X. Chen, Y. Yang, H. Shi, M.F. Li, Y. Chu, Z.Y. Pan, X.B. Yu, Regulating product distribution in deoxygenation of methyl laurate on silica-supported Ni-Mo phosphides: Effect of Ni/Mo ratio, *Fuel* 129 (2014) 1-10.
- [28] D.J. Rensel, S. Rouvimov, M.E. Gin, J.C. Hicks, Highly selective bimetallic FeMoP catalyst for C–O bond cleavage of aryl ethers, *J. Catal.* 305 (2013) 256-263.
- [29] A. Cho, J. Shin, A. Takagaki, R. Kikuchi, S.T. Oyama, Ligand and ensemble effects in bimetallic NiFe phosphide catalysts for the hydrodeoxygenation of 2-methyltetrahydrofuran, *Top. Catal.* 55 (2012) 969-980.
- [30] Z. Pan, R. Wang, M. Li, Y. Chu, J. Chen, Deoxygenation of methyl laurate to hydrocarbons on silica-supported Ni-Mo phosphides: Effect of calcination temperatures of precursor, *J. Energy. Chem.* 24 (2015) 77-86.
- [31] F.X. Sun, W.C. Wu, Z.L. Wu, J. Guo, Z.B. Wei, Y.X. Yang, Z.X. Jiang, F.P. Tian, C. Li, Dibenzothiophene hydrodesulfurization activity and surface sites of silica-supported MoP, Ni₂P, and Ni-Mo-P catalysts, *J. Catal.* 228 (2004) 298-310.
- [32] R. Wang, K.J. Smith, Preparation of unsupported NiMoP catalysts for 4,6-dimethyldibenzothiophene hydrodesulfurization, *Catal. Lett.* 144 (2014) 1594–1601.
- [33] S. V. Oryshchyn, O. V. Zhak, P. Guérin, S. Députier, and Yu. B. Kuz'ma, Structure of Mo_{2.0-0.2x}Ni_{1.0+x}P (x = 0.2) and some crystal-chemical features of ternary phases in the Mo–Ni–P System, *Inorganic Materials*, 38 (2002) 1195–1202. Translated from *Neorganicheskie Materialy*, 38 (2002) 1422.

-
- [34] Y. Maeda, Y. Takashima, Mössbauer studies of FeNiP and related compounds, *J. Inorg. Nucl. Chem.* 35 (1973) 1963-1969.
- [35] A.F. Gaudette, A.W. Burns, J.R. Hayes, M.C. Smith, R.H. Bowker, T. Seda, M.E. Bussell, Mössbauer spectroscopy investigation and hydrodesulfurization properties of iron–nickel phosphide catalysts, *J. Catal.* 272 (2010) 18–27.
- [36] Y. Maeda, Y. Takashima, Mössbauer studies of solid solution systems of Fe(P, As), (Fe, Co)P, (Fe, Mn)P and (Fe, W)P, *J. Inorg. Nucl. Chem.* 35 (1973) 1219-1225.
- [37] G.-N. Yun, A. Takagaki, R. Kikuchi, S. Ted Oyama, Hydrodeoxygenation of gamma-valerolactone on transition metal phosphide catalysts, *Catal. Sci. Technol.* 7 (2017) 281-292.
- [38] J.A. Cecilia, A. Infantes-Molina, E. Rodriguez-Castellon, A. Jimenez-Lopez, The influence of the support on the formation of Ni₂P based catalysts by a new synthetic approach. Study of the catalytic activity in the hydrodesulfurization of dibenzothiophene, *J. Phys. Chem. C* 113 (2009) 17032-17044.
- [39] S.V. Oryshchyn, Yu.B. Kuz'ma, Yu.B., A new compound Mo₂Ni₆P₃ and Its crystal structure, *Kristallografiya*, 25, (1980) 1066–1068.
- [40] S.V. Oryshchyn, Yu.B. Kuz'ma, N.G. Markiv, X-ray Diffraction Study of the Mo–Ni–P System, *Dokl. Akad. Nauk Ukr. SSR*, 9 (1981) 80–83.
- [41] S. Rundqvist, X-ray investigations of Mn₃P, Mn₂P, and Ni₂P, *Acta Chem. Scand.* 16 (1962) 992-998.
- [42] Guérin, R. and Sergent, M., Crystal structure of NiMoP, *Acta Crystallogr., B: Struct. Crystallogr. Cryst. Chem.* 33 (1977) 2920–2823.
- [43] P.R. Guérin, M. Sergent, Structure cristalline de NiMoP, *Acta Crystallogr. B* 33 (1977) 2820-2823.
- [44] S. Rundqvist, T. Lundström, X-ray studies of molybdenum and tungsten phosphides, *Acta Chem. Scand.* 17 (1963) 37–46.
- [45] D. Ma, T. Xiao, S. Xie, W. Zhou, S.L. Gonzalez-Cortes, M.L.H. Green, Synthesis and structure of bimetallic nickel molybdenum phosphide solid solutions, *Chem. Mater.* 16 (2004) 2697-2699.

-
- [46] S.H. Zhou , Y. Wang, C. Jiang, J.Z. Zhu, L.-Q. Chen, Z.-K. Liu First-principles calculations and thermodynamic modeling of the Ni–Mo system, *Mater. Sci. Eng. A* 397 (2005) 288–296.
- [47] O'Neill, H. S. C., Free energies of formation of NiO, CoO, Ni₂SiO₄, and Co₂SiO₄, *Am. Mineral.*, 72, (1987), 280-291.
- [48] N. Rösch, G. Pacchioni, Density functional cluster calculations of metal deposition on oxide surfaces, in *Chemisorption and Reactivity on Supported Clusters and Thin Films*, NATO ASI Series, 131 (1997) 353-370.
- [49] Z. Wu, F. Sun, W. Wu, Z. Feng, C. Liang, Z. Wei, C. Li, On the surface sites of MoP/SiO₂ catalyst under sulfiding conditions: IR spectroscopy and catalytic reactivity studies, *J. Catal.* 222 (2004) 41-52.
- [50] K.A. Layman, M.E. Bussell, Infrared spectroscopic investigation of CO adsorption on silica-supported nickel phosphide catalysts, *J. Phys. Chem. B* 108 (2004) 10930-10941.
- [51] G. Blyholder, Molecular orbital view of chemisorbed carbon monoxide, *J. Phys. Chem.* 68 (1964) 2772–2778.
- [52] J.A. Rodriguez, J.Y. Kim, J. C. Hanson, S. J. Sawhill, M.E. Bussell, Physical and chemical properties of MoP, Ni₂P, and MoNiP hydrodesulfurization catalysts: Time-resolved X-ray diffraction, density functional, and hydrodesulfurization activity studies, *J. Phys. Chem. B* 107 (2003) 6276-6285.
- [53] S. Oyama, X. Zhang, J. Lu, Y. Gu, T. Fujitani, Epoxidation of propylene with H₂ and O₂ in the explosive regime in a packed-bed catalytic membrane reactor, *J. Catal.* 257 (2008) 1-4.
- [54] P.B. Weisz, C.D. Prater, Interpretation of measurements in experimental catalysis, *Adv. Catal.* 6 (1954) 143-196.
- [55] M. Boudart, Effects of surface structure on catalytic activity, *Proc. 6th Int. Cong. Catal*, G.C. Bond, P.B. Wells, F.C. Thompson, Eds., Chemical Society London, 1976, pp. 1-9.
- [56] A. Cho, H. Kim, A. Iino, A. Takagaki, S. T. Oyama, Kinetic and FTIR studies of 2-methyltetrahydrofuran hydrodeoxygenation on Ni₂P/SiO₂, *J. Catal.* 318 (2014) 151–161.

-
- [57] P. Bui, A. Takagaki, R. Kikuchi, S. T. Oyama, Kinetic and infrared spectroscopy study of hydrodeoxygenation of 2-methyltetrahydrofuran on a nickel phosphide catalyst at atmospheric pressure, *ACS Catal.* 6 (2016) 7701-7709.
- [58] Y.-K. Lee and S. T. Oyama, Bifunctional nature of a SiO₂-supported Ni₂P catalyst for hydrotreating: EXAFS and FTIR studies, *J. Catal.* 239 (2006) 376-389.

Chapter 4

Kinetic and Spectroscopic Studies of Catalytic Mechanisms: Hydrodeoxygenation of γ -Valerolactone on Ni₂P/MCM-41

4.1 Introduction

Growing concerns about the depletion of fossil energy supplies have resulted in interest in the development of biomass resources [1]. Biomass is an abundant feedstock which can satisfy the increase in demand for the production of fuels and chemicals [2, 3]. Various conventional technologies, such as torrefaction of birch and corn stalk [4, 5], hydrothermal liquefaction of paulownia [6], and fast pyrolysis of beech wood [7] have shown biomass to be a viable feedstock. In particular, pyrolysis of biomass is considered the most promising approach to produce liquid intermediates [8, 9].

A major barrier in the application of bio-oil is that it contains large levels of oxygen (35 ~ 40 wt.%) which result in low heating value and chemical instability [10]. To overcome these drawbacks, there has been extensive work on hydrodeoxygenation (HDO) of pyrolysis oil derived from cedar chips [11], sawdust [12, 13], and palm oil [14], as well as bio-oil model compounds, such as furans [15, 16, 17], phenols [18, 19, 20], pyrans [21], and ketones [22] using various catalysts including metal sulfides [23, 24], noble metals [25, 26], metal oxides [27], and metal phosphides [28, 29, 30].

Although studies of HDO of real bio-oil feeds have merits, they do not provide detailed insights into factors controlling catalyst performance because of the complexity of the bio-oil, so that model compound studies are required to give greater understanding of catalyst behavior [21, 31, 32]. In addition, in situ spectroscopies such as FTIR [33, 34]

and EXAFS [33, 35, 36] are extensively used for identification of the active phase of catalysts and elucidation of reaction mechanism by providing information on the working state of the catalysts. It was reported that combined in situ QXAFS and FTIR analysis of Ni₂P/MCM-41 indicated that NiPS was the active phase and identified reaction intermediates and the reaction pathway for the hydrodesulfurization of thiophene [34].

Transition metal phosphide catalysts [37] have been shown to be effective in removing oxygen from bio-oil model compounds [38, 39, 40]. In particular, Ni₂P/SiO₂ was found to be the most active among a series of silica-supported transition metal phosphides for the HDO of 2-methyltetrahydrofuran (2-MTHF) [15]. This was also the case in a recent study with γ -valerolactone (GVL) [41], an important component in bio-oil, in which a Ni₂P/MCM-41 catalyst was substantially more active than other transition metal phosphides (CoP/MCM-41, MoP/MCM-41, WP/MCM-41) and a commercial Pd/Al₂O₃ catalyst. This further confirms the exceptional reactivity of Ni₂P for removing oxygen. The previous work [41] did not involve reaction network studies, and for this reason the objective of this work is to provide a kinetic analysis of the reaction network of GVL on Ni₂P/MCM-41 by contact time measurements, and to investigate the effects of GVL and H₂ partial pressures. Furthermore, the adsorbed species on the catalyst surface and the working state of Ni species during the reaction were monitored by in situ infrared spectroscopy and in situ quick x-ray adsorption fine structure measurement to support the proposed reaction sequence. These measurements and analyses are important to obtain basic information about the manner of oxygen removal using Ni₂P/MCM-41.

4.2 Experimental

4.2.1. Preparation and characterization of Ni₂P supported on MCM-41

The supported nickel phosphide was prepared from a phosphite precursor as described in previous studies [42, 43]. A commercial MCM-41 support (Aldrich) was impregnated with aqueous solutions of Ni(OH)₂ (Aldrich, 99%) and H₃PO₃ (Aldrich, 99%), followed by drying at 120 °C overnight without high-temperature calcination. The amount of nickel was 5 mmol per 5 g of support and the initial ratio of Ni/P was fixed at 1/2. The dried precursor was pelletized and sieved, and then reduced at 580 °C for 2 h in H₂ flow (1000 ml min⁻¹ per 1 g of sample). The reduction temperature was determined by H₂-TPR as reported previously [41]. After reduction and cooling in He, the sample was passivated in 0.5% O₂/He flow at room temperature for 3 h, and then stored in a desiccator to minimize further oxidation.

Transmission electron microscopy (TEM) images of Ni₂P/MCM-41 were obtained using a JEOL JEM 2000EXII microscope operated at 200 kV. The passivated Ni₂P/MCM-41 catalyst was ground to a fine powder and dispersed in ethanol for 20 min using a sonicator. The resulting mixture was put on a carbon-coated copper grid and then dried at 30 °C for 30 min. Carbon monoxide (CO) uptake was measured by a pulse injection method using 0.3 g of passivated sample re-reduced at 550 °C in H₂ (100 ml/min) for 3 h. Pulses (25 μl) of 3 % CO/He were passed over the sample at room temperature using a He carrier (50ml/min), and the mass signal (m/z=28) was monitored by a quadruple mass spectrometer to measure the total dynamic gas uptake. The specific surface area of the samples was calculated from the linear portion of BET plots (P/P₀ = 0.01 - 0.20) obtained from N₂ adsorption isotherms at 77 K using a BELSORP mini II

micropore size analyzer. Prior to the measurements, the sample was dried and evacuated at 120 °C overnight.

4.2.2. Catalytic activity test

Reaction tests for the HDO of GVL over the Ni₂P/MCM-41 catalyst were conducted in a fixed-bed continuous flow reactor at 300 °C and 0.5 MPa. The passivated catalyst was loaded in the middle of the reactor with quartz beads to give a uniform flow in the catalyst bed. After pretreatment of the catalyst under H₂ (100 ml min⁻¹g_{catalyst}⁻¹) at 550 °C for 3 h, the total pressure was fixed at 0.5 MPa using a back-pressure regulator. The liquid reactant containing 98 wt. % of GVL and 2 wt. % of toluene as an internal standard was fed with a liquid pump via a vaporizer held at 300 °C with a H₂ flow. The toluene did not react at the reaction conditions used in this study. For all the tests, the reaction conditions were maintained for 2-3 h to reach steady-state. An on-line gas chromatograph (Shimadzu GC-14A, DB-624 UI, 60 m x 0.25 mm x 1.40 μm) equipped with a flame ionization detector (FID) and a thermal conductivity detector (TCD) was used to analyze the products at 1 h intervals.

The conversion of GVL, selectivity, and turnover frequency (TOF) were calculated by the following equations:

$$GVL \text{ conversion} = \left(1 - \frac{\text{Moles of GVL in product}}{\text{Moles of GVL in feed}} \right) \times 100\%$$

$$Selectivity = \left(\frac{\text{Moles of product}}{\text{Moles of total products}} \right) \times 100\%$$

$$TOF(s^{-1}) = \frac{\text{Conversion} \times \text{Flow rate of GVL} (\mu\text{mol s}^{-1})}{\text{Catalyst weight}(g) \times \text{Quantity of CO uptake site} (\mu\text{mol}/g)}$$

Contact time studies were carried out at 300 °C, 0.5 MPa and 0.2 - 6 s of contact time.

Contact time was defined as:

$$\text{Contact time (s)} = \frac{\text{CO uptake site } (\mu\text{mol/g}) \times \text{Amount of catalyst (g)}}{\text{Flow rate of GVL } (\mu\text{mol/s})}$$

The contact time was varied by changing the amount of catalyst (0.03, 0.10, and 0.14 g) and/or the flow rate of GVL (1.66-9.16 $\mu\text{mol/s}$) while adjusting the H_2 flow to give a constant feed concentration (4 mol% GVL in H_2).

For the effect of reactants partial pressure, the reactions were carried out with varying H_2 partial pressure or GVL partial pressure at 300 °C and 0.5 MPa with a quantity of 0.03 g of $\text{Ni}_2\text{P/MCM-41}$. For the effect of H_2 partial pressure, the H_2 partial pressure was varied in the order: 384, 240, 96, 48, 192, and 288 kPa by changing the H_2 flow rate (7.8-63 $\mu\text{mol/s}$) with N_2 as balance gas at a constant GVL partial pressure (12 kPa). For the effect of GVL partial pressure, the GVL partial pressure was changed in the order: 4.8, 14.4, 24.0, 19.2, and 9.6 kPa by varying GVL flow rate (1.63-8.16 $\mu\text{mol/s}$) with N_2 as the balance gas at a constant H_2 partial pressure (439 kPa).

4.2.3. In situ Fourier transform infrared spectroscopy (FTIR) measurements

Infrared spectroscopy was applied in two modes (temperature programmed desorption (TPD) and transient desorption) [16] with the $\text{Ni}_2\text{P/MCM-41}$ catalyst at 0.5 MPa using a JASCO FT/IR-6100 spectrometer equipped with an MCT detector with a resolution of 1 cm^{-1} in the region of $4000\text{--}1000 \text{ cm}^{-1}$. The samples were prepared in the form of a disk (diameter = 1 cm and 15 mg) and placed in the middle of an in situ cell equipped with KBr windows which were maintained at 30 °C by a circulation cooler. In

order to avoid condensation of GVL at the windows, a N_2 stream was used as a purging gas at both ends of the cell. The TPD of GVL adsorbed on the $Ni_2P/MCM-41$ catalyst was studied under N_2 or H_2 flow. After pretreatment of the catalyst at $550\text{ }^\circ\text{C}$ for 3 h in H_2 (50 ml/min), background spectra were obtained at 175, 200, 225, 250, 275, 300, 325 and $350\text{ }^\circ\text{C}$, respectively and then GVL was injected under N_2 or H_2 at $175\text{ }^\circ\text{C}$. After saturation of GVL on the catalyst surface at $175\text{ }^\circ\text{C}$, as indicated by the lack of change in the spectra, the samples were purged with N_2 or H_2 in the absence of GVL for 1 h until unchanging spectra were again obtained. The IR spectra were collected under N_2 or H_2 as the temperature was increased from 175 to $350\text{ }^\circ\text{C}$. The transient spectra for desorption of GVL adsorbed on the $Ni_2P/MCM-41$ catalyst were obtained at $300\text{ }^\circ\text{C}$ and 0.5 MPa under N_2 or H_2 flow. After pretreatment at $550\text{ }^\circ\text{C}$, the samples were cooled to $300\text{ }^\circ\text{C}$ in N_2 or H_2 flow and background spectra were obtained at 0.5 MPa. Then GVL was injected into the cell under N_2 or H_2 until constant spectra were achieved. After saturation, IR spectra were collected in the absence of GVL under N_2 or H_2 flow at $300\text{ }^\circ\text{C}$ and 0.5 MPa.

4.2.4. In situ quick X-ray absorption fine-structure (QXAFS) measurement

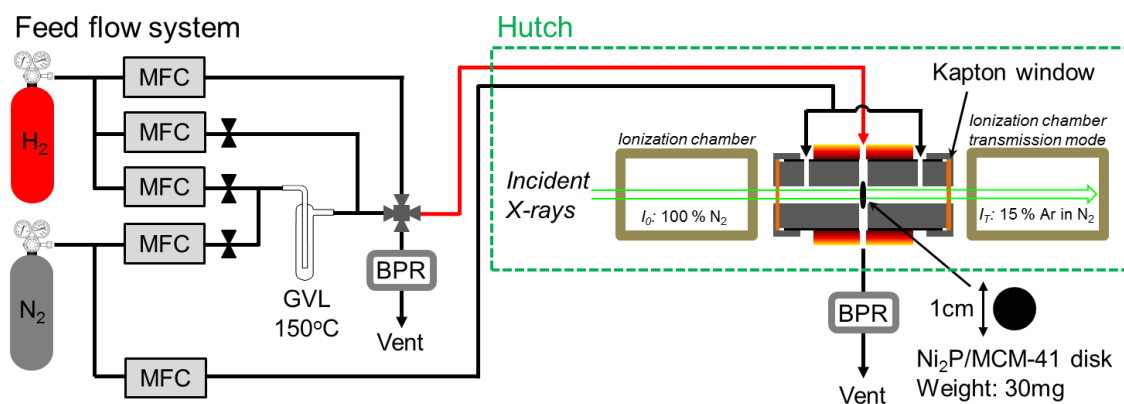


Figure 4.1. In situ quick x-ray absorption fine structure (QXAFS) reactor system

In situ quick X-ray absorption fine-structure (QXAFS) spectra at the Ni K-edge (8.333 keV) of Ni₂P/MCM-41 were recorded in the energy range of 8.233-9.300 keV at beam line 9C (BL9C) of the Photon Factory in the Institute of Materials Structure Science, High-Energy Accelerator Research Organization (KEK-IMSS-PF). The X-ray ring was operated at 2.5 GeV with a beam current of 450 mA. All spectra were recorded in transmission mode using ionization chambers for the detection of primary (I_0 , 100 % N₂) and transmitted (I_T , 25% Ar balanced with N₂) beam intensities. The detailed experimental set-up is illustrated in Fig. 4.1. About 30 mg of Ni₂P/MCM-41 was pressed into a disk with diameter of 10 mm and placed in an in situ cell equipped with water cooled Kapton windows at 70 °C. In order to avoid condensation of reactant and/or products, a purge gas (He, 10 ml/min) was passed at the ends of the reactor. Prior to the measurement, the catalysts were reduced at 550 °C under H₂ (50 ml/min) for 3 h and then cooled to reaction temperature and pressurized at 0.5 MPa. Then the gas was switched to a reactant mixture. The gas flow was passed via the bubbler containing GVL, which was kept at 150 °C by a heating jacket. The Antoine equation was used to estimate the GVL partial pressure as follows:

$$\log P^{sat} = A - \frac{B}{T (K) + C}$$

Where P^{sat} is the vapor pressure (kPa), T is the bubbler temperature (K) and the Antoine coefficients for GVL are 3.486, 1315, and -105.79 for A, B and C, respectively [44].

For temperature-dependence tests, after the pretreatment, the catalysts were stabilized for 20 min and then the gas mixture (4 mol % GVL in H₂) was introduced

into the cell at the reaction temperature and a pressure of 0.5 MPa. The measurement was repeated at 350, 300, and 250 °C with each temperature maintained for 80 min to reach steady-state conditions. After each measurement, the catalysts were treated at 550 °C for 3 h in H₂ flow.

For the effect of GVL partial pressure, after the pretreatment, the catalysts were stabilized at 300 °C and 0.5 MPa for 20 min. The GVL partial pressure was varied in the order: 20, 16, 8, 2, 4 and 12 kPa by adding H₂ as a diluent after the bubbler to maintain a constant total flow rate (50 ml/min).

4.3. Results and discussion

4.3.1. Characterization of Ni₂P/MCM-41 catalyst

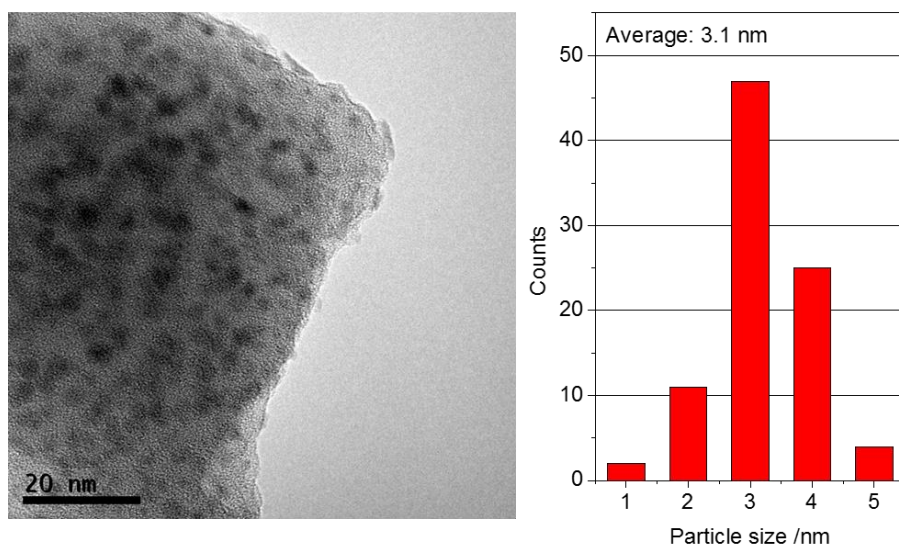


Figure 4.2. TEM image and particle size distribution of Ni₂P/MCM-41

The physicochemical properties of the Ni₂P/MCM-41 are summarized in Table 1. The BET surface area of Ni₂P/MCM-41 was 663 m²g⁻¹ and the number of CO uptake sites was 70 μmolg⁻¹. The presence of the Ni₂P phase was confirmed by XRD and

EXAFS measurements in our previous work [41]. The Ni₂P particles have narrow size distribution with average crystallite size between 3-4 nm, as evidenced by TEM images as shown in Fig. 4.2.

Table 4.1. Textural properties of Ni₂P/MCM-41

Sample	S _{BET}	CO-uptake	Crystallite size ^a
Ni ₂ P/MCM-41	663 m ² g ⁻¹	70 μmol g ⁻¹	3.1 nm

^a Average size estimated by TEM

4.3.2. Contact time analysis and reaction network

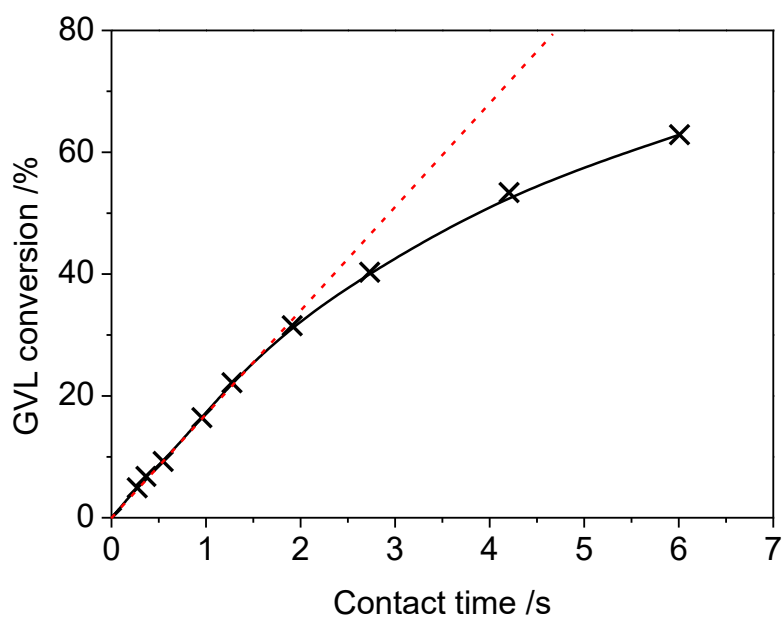


Figure 4.3. GVL conversion as a function of contact time at 300 °C and 0.5 MPa on Ni₂P/MCM-41 with 4 mol% GVL (20 kPa) in H₂ flow

Fig. 4.3 shows GVL conversion as a function of contact time at 300 °C and 0.5 MPa on Ni₂P/MCM-41. The conversion increased with contact time as expected. Within the low conversion region (below 35 %), the plot showed a linear dependence, while in

the high conversion region (over 48 %), the plot deviated below the line. This is ascribed to mass transfer limitations, the occurrence of which were estimated by the Weisz-Prater criterion C_{WP} by the following equation [45, 46]:

$$C_{WP} = \frac{\text{Reaction rate}}{\text{Diffusion rate}} = \frac{-r'_{A(obs)} \rho_c R^2}{D_e C_{As}}$$

Where $-r'_{A(obs)}$ is the observed reaction rate in $\text{mol g}^{-1} \text{s}^{-1}$, ρ_c is the catalyst density in g cm^{-3} , R is the catalyst particle radius in cm , D_e is the effective diffusivity in $\text{cm}^2 \text{s}^{-1}$, and C_{As} is the concentration at the surface in mol cm^{-3} . The parameters, conversion, observed reaction rate $-r'_{A(obs)}$, and the Weisz-Prater criterion C_{WP} are summarized in Table 4.2. The value of C_{WP} was over 0.3 for the contact time of 4.2 s, indicating mass transfer limitations above this value. This agrees with the deviation from linearity observed in Fig. 4.3.

Table 4.2. Summary of parameters, conversion, reaction rates, and Weisz-Prater criteria

R /cm	ρ_c /g cm ⁻³	D_e /cm ² s ⁻¹	C_{As} /mol cm ⁻³
0.09	0.3	0.1	4.11E-07

Contact time /s	Conversion /%	$-r'_{A(obs)}$ /mol g ⁻¹ s ⁻¹	C_{WP}	Regime
6.13	69.7	8.1E-06	0.47	Mass transfer limitations
4.20	56.4	6.6E-06	0.36	
2.73	40.3	4.7E-06	0.27	Free from transport limitations
1.91	31.5	3.7E-06	0.21	
1.27	22.2	2.6E-06	0.15	
0.96	16.4	1.9E-06	0.11	
0.57	9.2	1.1E-06	0.06	
0.38	6.8	7.9E-07	0.05	
0.29	4.9	5.7E-07	0.03	

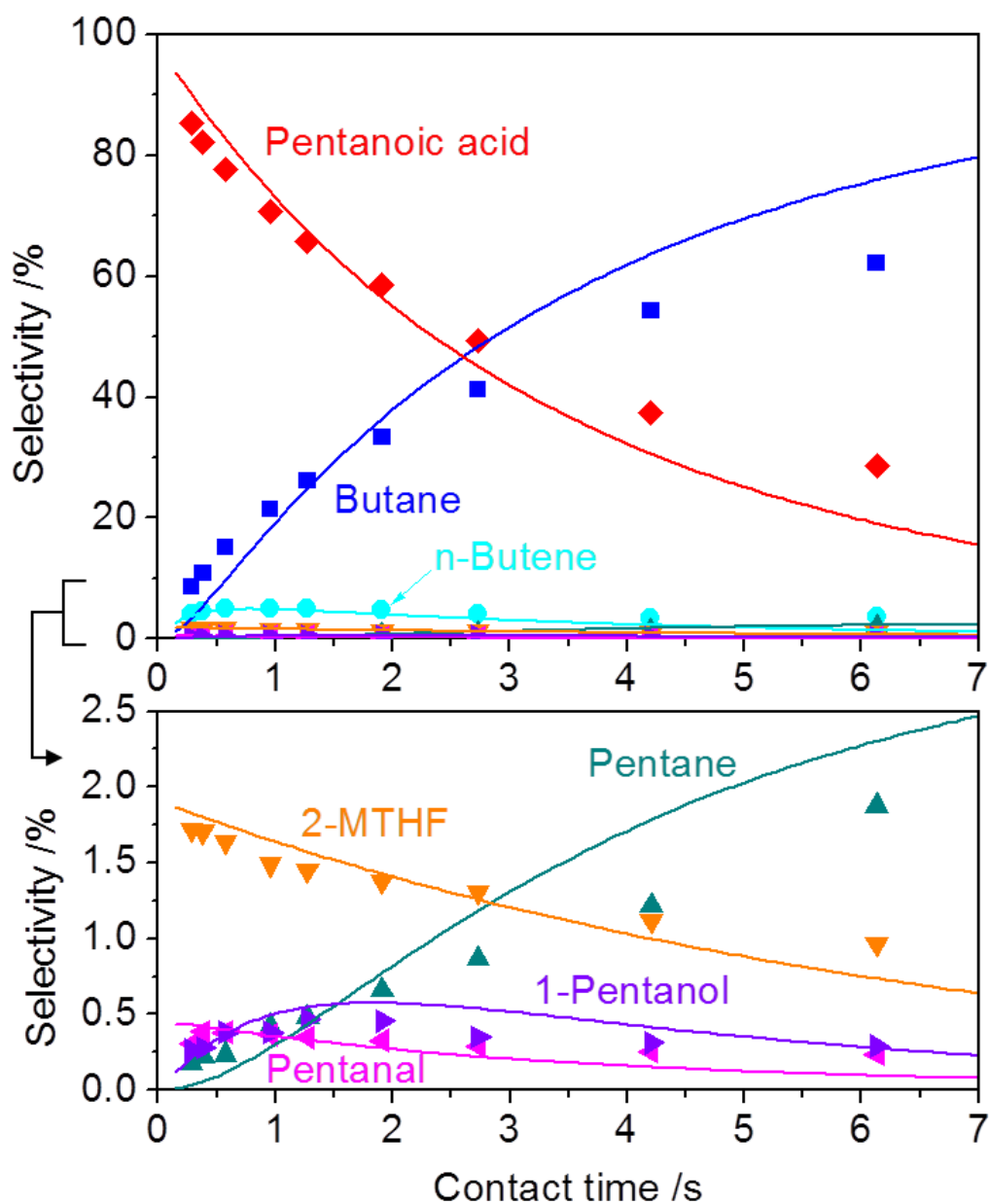


Figure 4.4. Product selectivity of the main products as a function of contact time at 300 °C and 0.5 MPa on Ni₂P/MCM-41. The points are the experimental results and the curves are calculated fits.

Fig. 4.4 shows the selectivity to the main products as a function of contact time at 300 °C and 0.5 MPa on Ni₂P/MCM-41. Minor products such as 2-pentanone and 2-pentanol were excluded from the calculations because their selectivity was below 0.2 %.

Carbon balances for all the data were in the range of $100\% \pm 5\%$. The selectivities to pentanoic acid and 2-MTHF decreased with increasing contact time, while those to butane and pentane increased continuously. The selectivities to pentanal and n-butene went through a maximum (0.3 % at 0.6 s for pentanal and 5 % at 1.0 s for n-butene), and then sharply decreased. Similarly, the selectivity to 1-pentanone passed through a maximum (0.5 % at 1.3 s) and then decreased. These trends suggest that pentanoic acid and 2-MTHF are primary products, pentanal, 1-pentanol, and n-butene are intermediate products, and n-pentane and n-butane are final products. The solid lines are results of fitting to a first order model. The rate constants are shown at the bottom of Fig. 4.5. The fits were reasonable with a regression coefficient of 0.97 below 2.73 s contact time. There are deviations at high contact time, perhaps due to the mass transfer limitations described earlier.

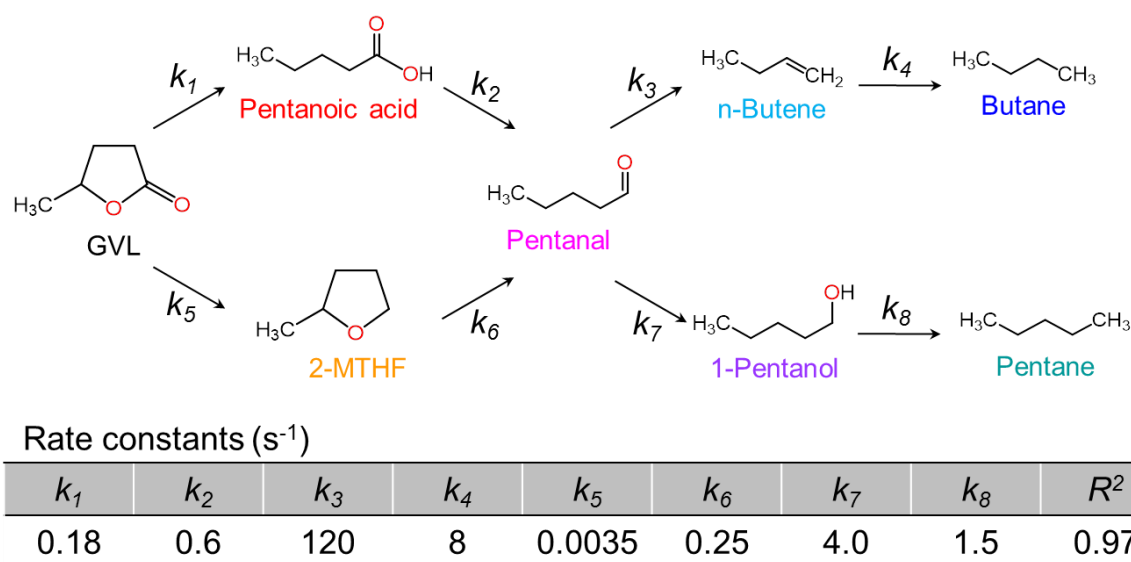


Figure 4.5. Possible reaction network of GVL on $Ni_2P/MCM-41$ at $300\text{ }^\circ\text{C}$ and 0.5 MPa and rate constants (s^{-1})

The reaction network based on the contact time results is shown in Fig. 4.5. General reaction routes of esters and acids have been reviewed [47], and the reactions proposed here are reasonable. There are two reaction routes. The first route (top) involves ring-opening of the lactone on the methyl substituted side, and the second (bottom) involves removal of the oxygen of the carbonyl group. In the first route, pentanoic acid is formed initially, which is then converted into pentanal. Afterward, n-butene is produced by decarbonylation with the formation of CO, following which n-butane is formed by hydrogenation. Although the results are not shown here, the mole ratio of CO/(butane + n-butene) was around 1.0 indicating a decarbonylation step [40, 41]. The product n-pentane was formed by sequential hydrogenation from pentanal. The second route involves the initial formation of 2-MTHF (2-methyltetrahydrofuran), which is then converted into either pentanal or 2-pentanone. the removal of the carbonyl oxygen seems difficult but there is precedent for such transformations of esters [48]. In previous work for the HDO of 2-MTHF on Ni₂P/SiO₂ at 300 °C and 0.5 MPa, the more hindered side was favored for the ring-opening of tetrahydrofuran to produce pentanal [15]. In the present study, the route from GVL to 2-MTHF is not favored, so it is acceptable to omit the formation of 2-pentanone and 2-pentanol because they can be only produced from 2-MTHF. After the formation of pentanal, the reaction route merges with the first route. The selectivity to pentanal is very low, despite being an intermediate for both routes, because it is rapidly converted into n-butane or 1-pentanol due to its high reactivity.

4.3.3 Partial pressure analysis

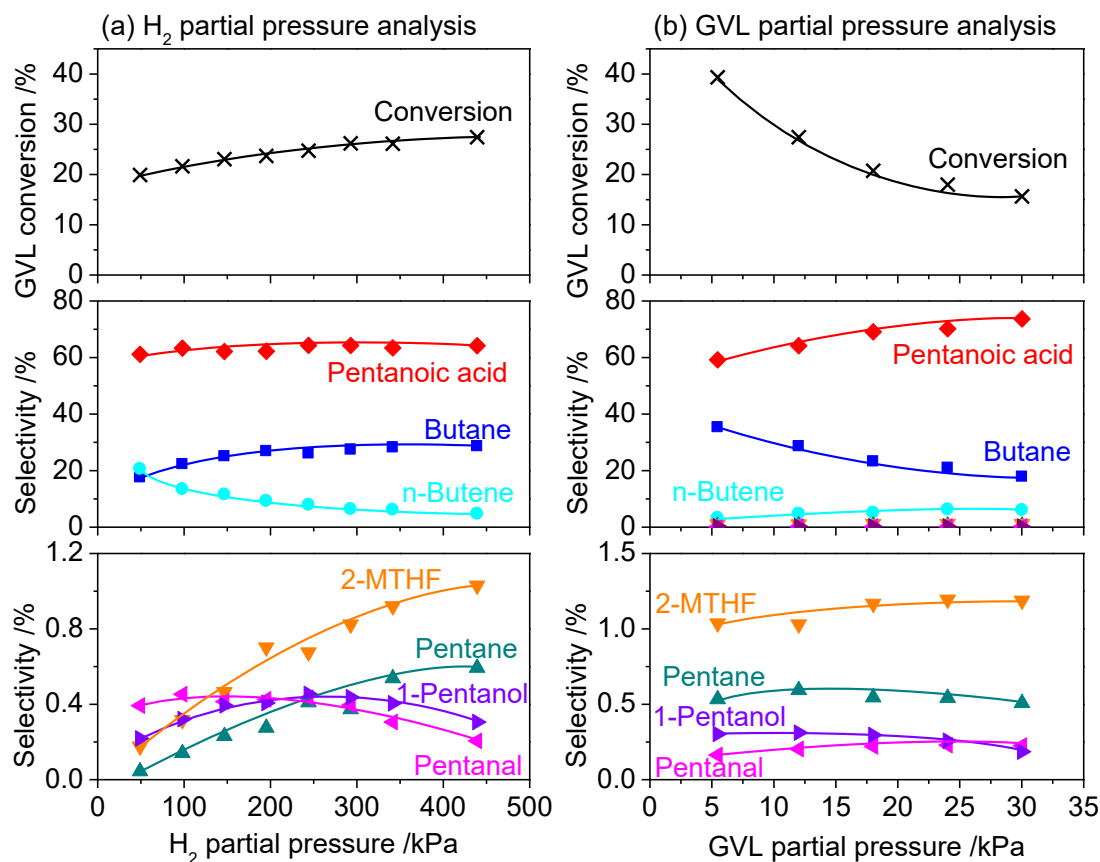
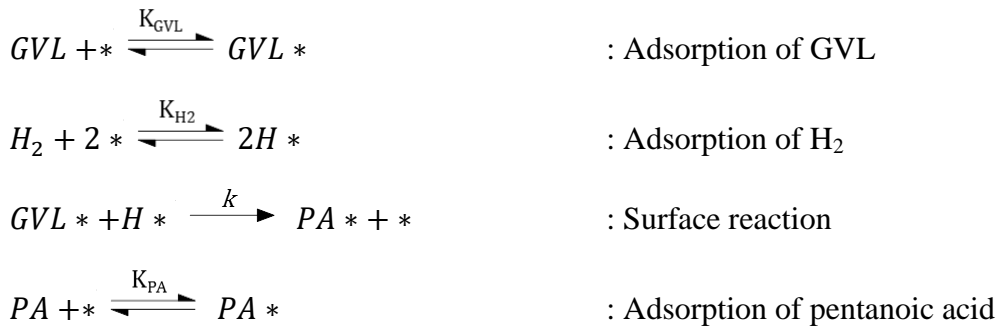


Figure 4.6. GVL conversion and selectivity to main products as a function of (a) H₂ partial pressure (P_{GVL} : 12 kPa) and (b) GVL partial pressure (P_{H_2} : 439 kPa) at 300 °C and 0.5 MPa

Fig. 4.6 shows GVL conversion and selectivity to the main products as a function of (a) H₂ partial pressure and (b) GVL partial pressure at 300 °C and 0.5 MPa with 4 mol% GVL in H₂ flow. Fig. 4.6 (a) shows that as H₂ partial pressure increased, GVL conversion as well as selectivities to pentanoic acid, 2-MTHF, pentane and butane increased, while selectivity to n-butene decreased. Furthermore, selectivity to 1-pentanol and pentanal went through a maximum and then decreased. On the other hand, Fig. 4.6 (b) reveals that as GVL partial pressure increased, selectivities to pentanoic acid, 2-MTHF and n-butene increased, while selectivity to butane and GVL conversion

decreased. These results are consistent with the proposed reaction pathway, in which hydrogenation was involved in transformation of GVL to pentanoic acid and n-butene to butane, and so increasing H₂ partial pressure favored these reactions.

The reaction can be described by a sequence of steps based on the Langmuir-Hinshelwood model.



The symbol * describes vacant sites on the catalyst surface and *GVL* *, *H* * and *PA* * represent adsorbed GVL, hydrogen atoms and pentanoic acid, respectively.

The coverages can be expressed as follows.

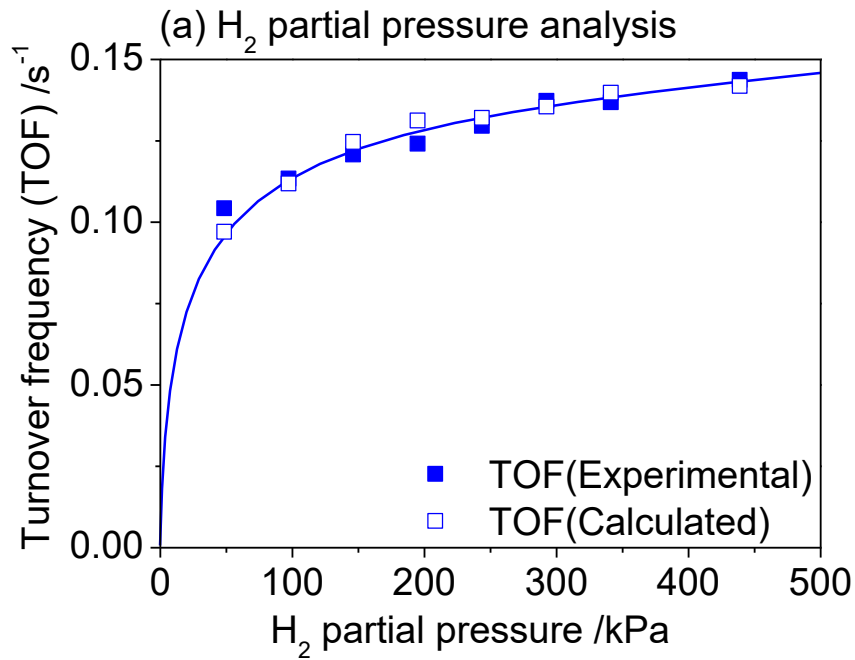
$$\begin{aligned}
 \theta_{GVL} &= K_{GVL} P_{GVL} \theta * \\
 \theta_H &= \sqrt{K_{H_2} P_{H_2}} \theta * \\
 \theta_{PA} &= K_{PA} P_{PA} \theta * \\
 \theta_{GVL} + \theta_H + \theta_{PA} + \theta * &= L \\
 \theta * &= \frac{1}{K_{GVL} P_{GVL} + \sqrt{K_{H_2} P_{H_2}} + K_{PA} P_{PA} + 1}
 \end{aligned}$$

A rate equation based on the partial pressure of GVL (P_{GVL}), H₂ (P_{H_2}) and pentanoic acid (P_{PA}) is derived taking the majority species on the surface to be adsorbed GVL (θ_{GVL}), pentanoic acid (θ_{PA}), hydrogen atoms (θ_H), and empty sites ($\theta *$).

The rate-determining step is assumed to be the surface reaction between adsorbed GVL and a single adsorbed H atom.

$$\begin{aligned}
 \text{Rate} &= k\theta_{GVL}\theta_H \\
 &= (kK_{GVL}P_{GVL}\theta^*)\sqrt{K_{H_2}P_{H_2}\theta^*} \\
 &= \frac{kK_{GVL}P_{GVL}\sqrt{K_{H_2}P_{H_2}}}{(1 + K_{GVL}P_{GVL} + \sqrt{K_{H_2}P_{H_2}} + K_{PA}P_{PA})^n} \quad n = 2
 \end{aligned}$$

Fig. 4.7 shows turnover frequency (TOF) as a function of H₂ partial pressure and GVL partial pressure at 300 °C and 0.5 MPa. The solid points are experimental data and the open points are calculated values. Although conversion decreased as a function of GVL partial pressure, the TOF increased because the increase in flow rate of GVL outweighed the corresponding decrease in conversion at the higher GVL partial pressures.



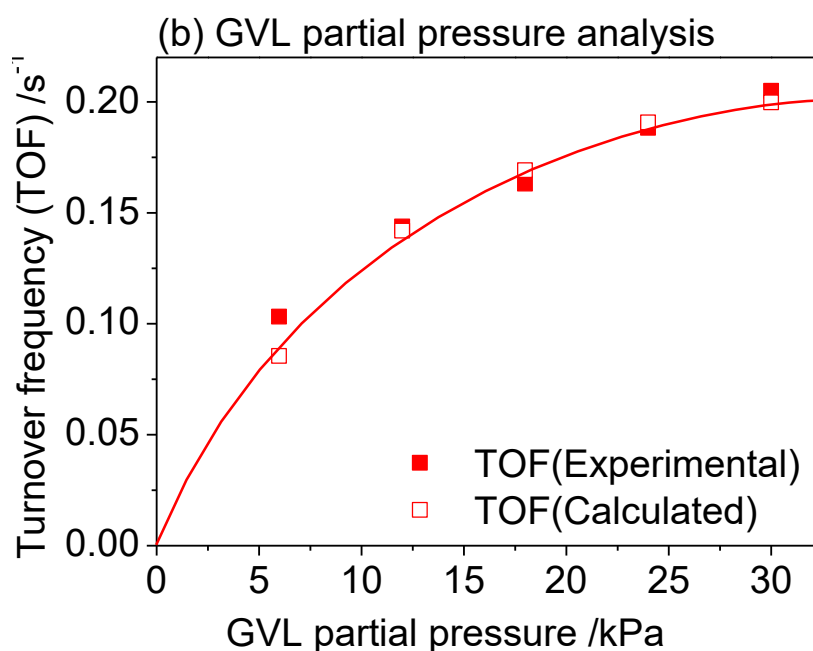


Figure 4.7. Turnover frequency (TOF) as a function of (a) H₂ partial pressure (P_{GVL} : 12 kPa) and (b) GVL partial pressure (P_{H_2} : 439 kPa) at 300 °C and 0.5 MPa from experimental and calculated results

The optimized parameter results are summarized in Table 4.3. In general, the exponent on the denominator is equal to the number of sites participating in the rate-determining surface-catalyzed reaction. The optimized exponent was 1.99, which is close to the theoretical value of 2 giving support for the suggested reaction sequence.

Table 4.3. Fitting parameters and regression coefficient

k (s ⁻¹)	K_{GVL} (kPa ⁻¹)	K_{H_2} (kPa ⁻¹)	K_{PA} (kPa ⁻¹)	n	R^2
1.88	257.3	1.1E+05	21.5	1.999	0.97

In regards to the adsorption equilibrium constants, the order was $K_{\text{H}_2} \gg K_{\text{GVL}} > K_{\text{PA}}$ indicating that hydrogen atoms are more strongly adsorbed on the surface site than GVL or pentanoic acid. This suggests that a substantial portion of the surface is

occupied with hydrogen atoms, except at high GVL partial pressure. This result is consistent with the results in Fig. 4.7 (a) where the TOF decreased slightly with decreasing H₂ partial pressure. However, as shown in Fig. 4.6 (a), selectivity to butane and pentane increased with H₂ partial pressure, suggesting that higher H₂ partial pressure enhanced the subsequent HDO reactions.

Based on the optimized parameters in Table 4.3, the coverages as a function of H₂ partial pressure and GVL partial pressure were calculated with the following equations:

$$\theta_{GVL} = \frac{K_{GVL}P_{GVL}}{K_{GVL}P_{GVL} + \sqrt{K_{H_2}P_{H_2}} + K_{PA}P_{PA} + 1}$$

$$\theta_{PA} = \frac{K_{PA}P_{PA}}{K_{GVL}P_{GVL} + \sqrt{K_{H_2}P_{H_2}} + K_{PA}P_{PA} + 1}$$

$$\theta_{H_2} = \frac{\sqrt{K_{H_2}P_{H_2}}}{K_{GVL}P_{GVL} + \sqrt{K_{H_2}P_{H_2}} + K_{PA}P_{PA} + 1}$$

$$\theta_* = \frac{1}{K_{GVL}P_{GVL} + \sqrt{K_{H_2}P_{H_2}} + K_{PA}P_{PA} + 1}$$

The calculated coverages are shown in Fig. 4.8. Increase of H₂ partial pressure resulted in an increase in H₂ coverage and decrease in GVL and pentanoic acid coverages, as expected (Fig. 4.8a). Similarly increase of GVL partial pressure resulted in an increase in GVL coverage and decrease in H₂ and pentanoic acid coverages (Fig. 4.8b). In both cases, empty sites were much smaller in number than the others, suggesting that GVL and pentanoic acid look for mainly adsorbed H₂ on the surface rather than empty sites.

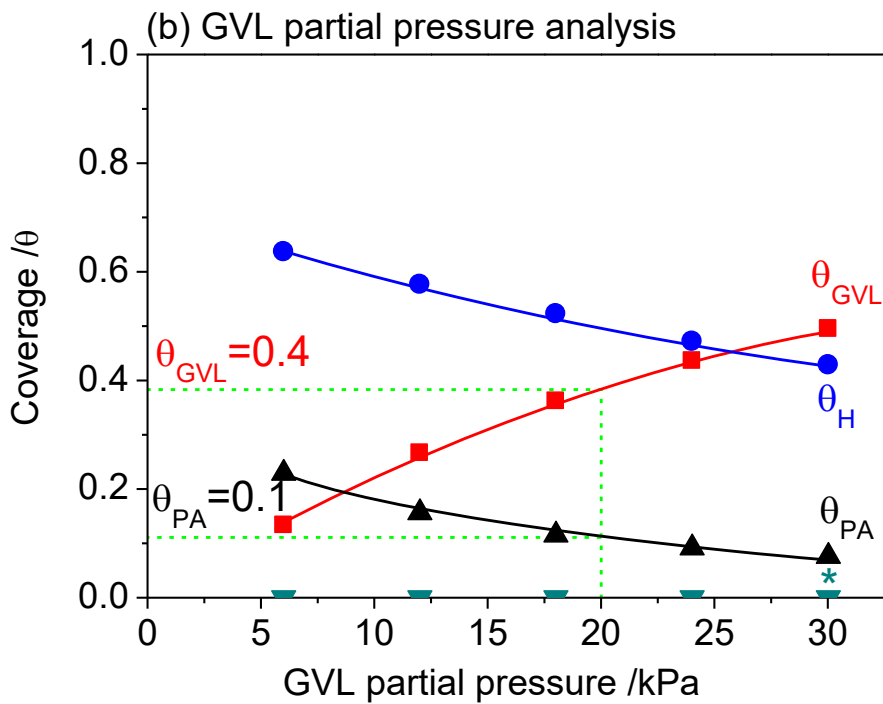
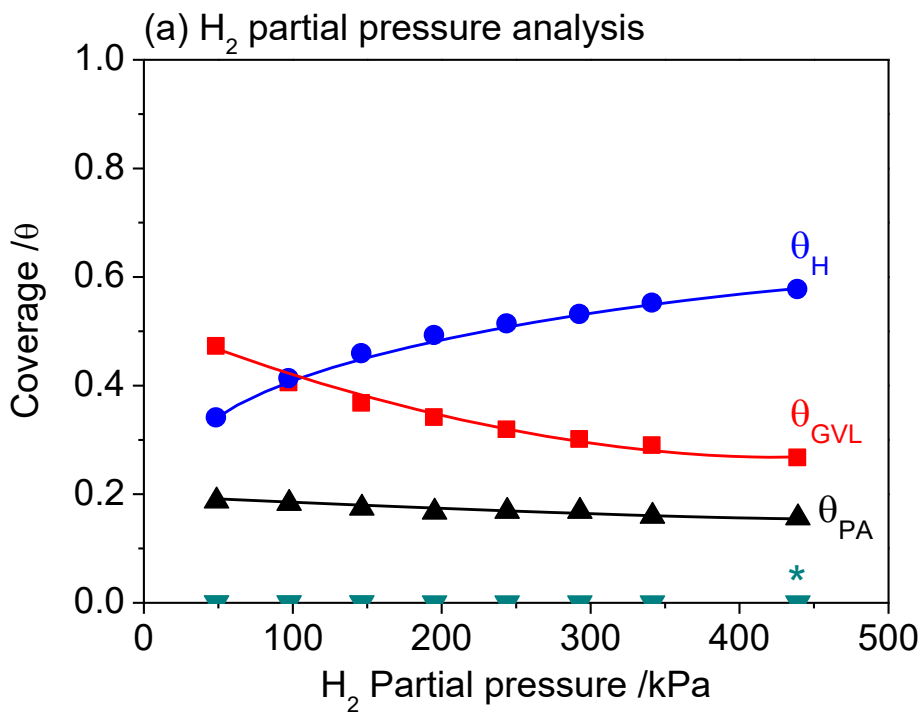


Figure 4.8. Calculated coverages as a function of (a) H₂ partial pressure (P_{GVL} : 20 kPa) and (b) GVL partial pressure (P_{H_2} : 452 kPa) at 300 °C and 0.5 MPa from experimental and calculated results (At a GVL partial pressure of 20 kPa, $\theta_{GVL} = 0.4$ $\theta_{PA} = 0.1$)

4.3.4 In situ Fourier transform infrared spectroscopy (FTIR) analysis

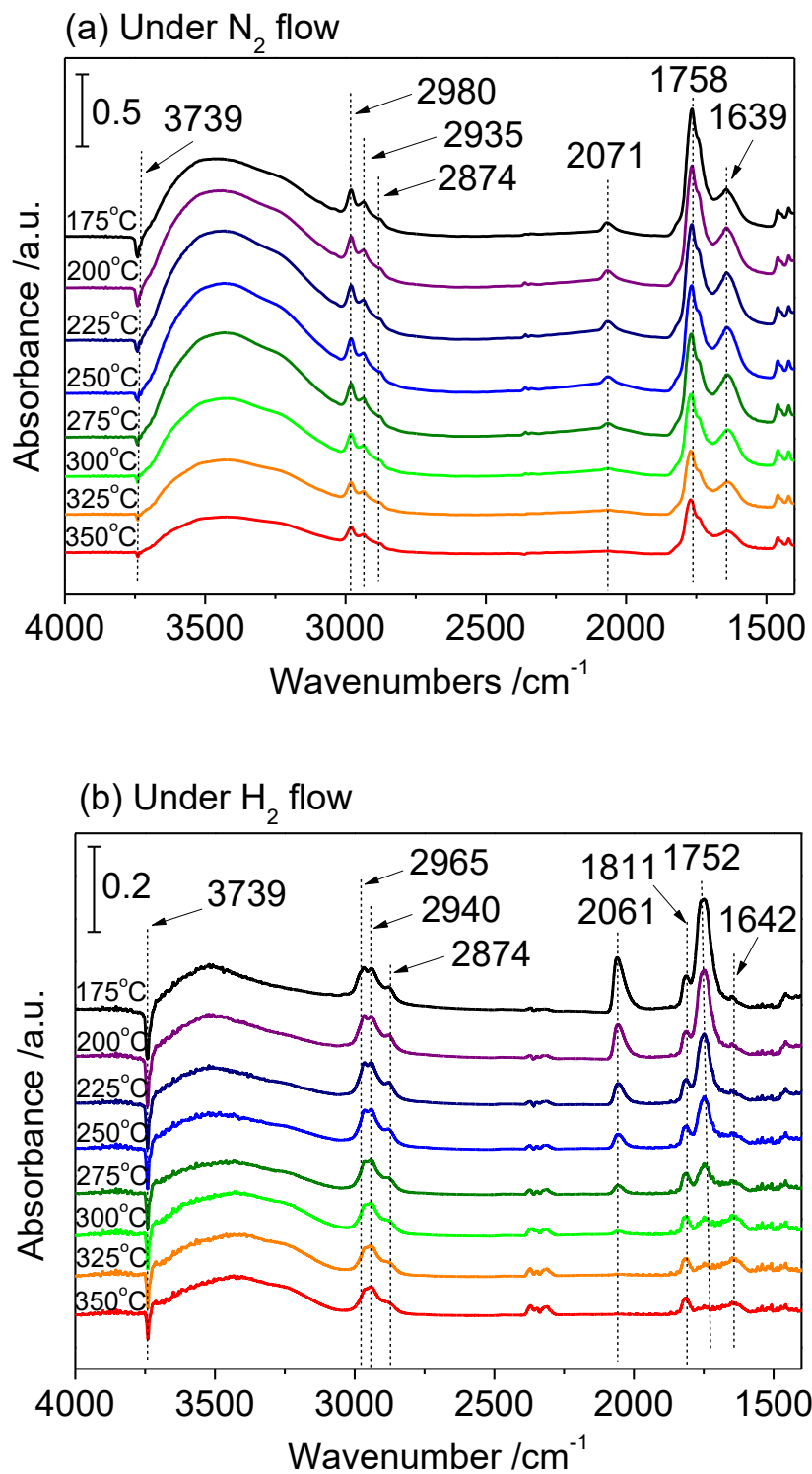


Figure 4.9. FTIR spectra of GVL adsorption on Ni₂P/MCM-41 under (a) N₂ flow and (b) H₂ flow as a function of temperature (175-350 °C) at 0.5 MPa

Fig. 4.9 shows FTIR spectra of GVL adsorbed on the Ni₂P/MCM-41 catalyst at 175-350 °C and 0.5 MPa under (a) N₂ flow and (b) H₂ flow. Each temperature was maintained for 0.5 h to get stable spectra. After pretreatment at 550 °C for 3 h with H₂, the catalyst was saturated with injection of GVL with H₂ at 175 °C for 0.2 h and then the cell was flushed with pure H₂ flow (50 ml/min) for 0.5 h to remove gas-phase and weakly-adsorbed GVL on the catalyst surface. All IR bands decreased with increasing temperature because of desorption of adsorbed species from the catalyst surface. A peak at 3741 cm⁻¹ (Si–OH) was observed under both N₂ and H₂, and was negative because of consumption of hydroxyl groups by interaction with GVL. The peak recovered intensity as temperature was raised because of desorption of GVL or some other species on the support. But, in H₂, the negative Si–OH peak still remained even at the highest temperature. These results indicate that some products or GVL were not formed under N₂ which were difficult to desorb, whereas these were formed under H₂. All spectra also showed aliphatic C–H stretching bands at 3000-2850 cm⁻¹ and C–H bending and scissoring bands at 1460–1380 cm⁻¹. These bands were attributed to adsorbed GVL and/or other reaction intermediates. Interestingly, under H₂ flow, the peak at 1752 cm⁻¹ decreased with increasing temperature while the peaks at 1811 and 1642 cm⁻¹ increased. On the other hand, under N₂ flow, all the peaks consistently decreased gradually. It is speculated that in reactive H₂ gas substantial reaction occurred with production of intermediates which remained on the surface, while in inert N₂ gas only desorption of GVL mainly occurred without reaction. The peak at 2061 cm⁻¹ derived from linearly adsorbed CO on Ni₂P under H₂ was visible at low temperature and then decreased with increasing temperature because of desorption of CO, while under N₂ flow the peak, shifted to 2071 cm⁻¹, was very small at all temperatures. The formation of CO resulted

from a decarbonylation reaction of pentanal as shown in the proposed reaction network (Fig. 4.5). Thus, the presence of H₂ was necessary for ring-opening and the subsequent deoxygenation reactions.

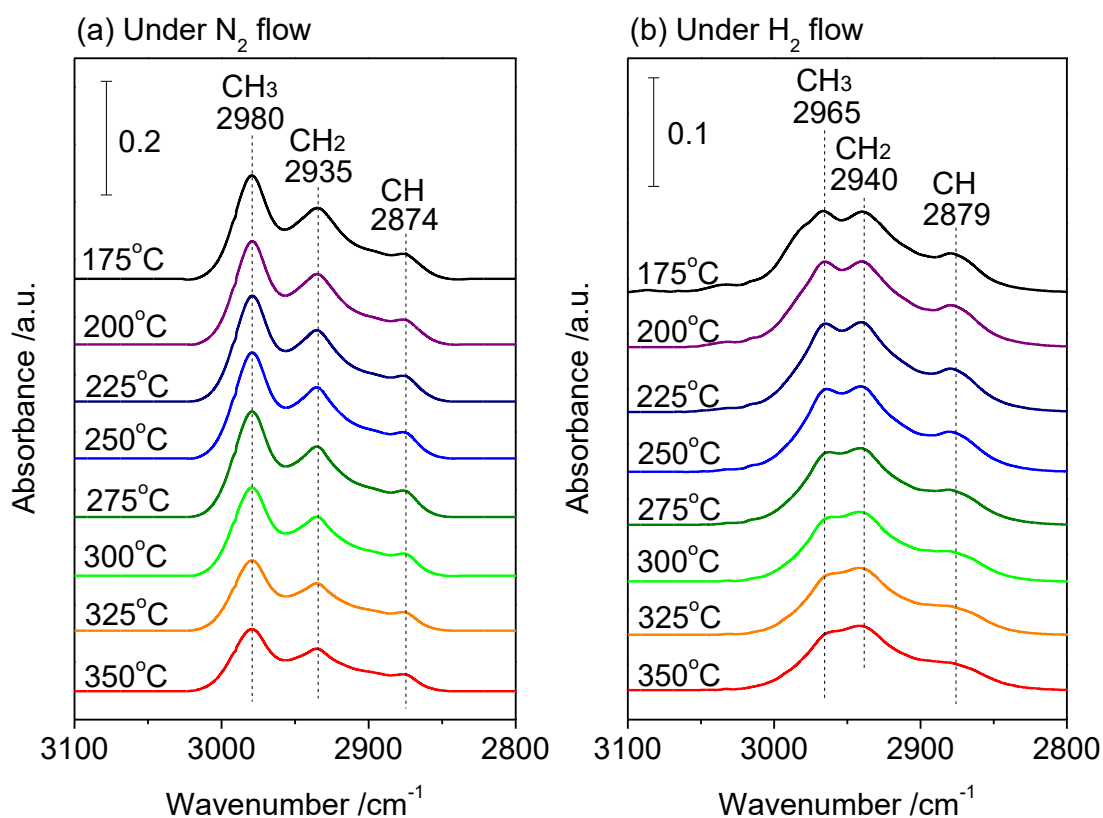


Figure 4.10. FTIR spectra of GVL adsorption on Ni₂P/MCM-41 under (a) N₂ flow and (b) H₂ flow on aliphatic C-H stretching region

Fig. 4.10 shows an expanded view in the aliphatic C-H stretching region of FTIR spectra of GVL adsorbed on the Ni₂P/MCM-41 catalyst under (a) N₂ flow and (b) H₂ flow. Three bands were observed, which can be assigned to predominantly CH₃, CH₂, and CH groups. In N₂ the bands corresponding to $\nu(\text{CH}_3)$ at 2981 cm⁻¹ and $\nu(\text{CH}_2)$ at 2965 cm⁻¹ presented similar intensities as temperature was increased, while in H₂ the $\nu(\text{CH}_2)$ at 2940 cm⁻¹ was relatively stronger than the $\nu(\text{CH}_3)$ at 3019 cm⁻¹. Fig. 4.11

shows modes of adsorption of GVL in N_2 and H_2 . In N_2 simple molecular adsorption occurs (Fig. 4.11(a)) via interaction of the carbonyl O in a $\eta^1(O)$ -aldehyde configuration with a Ni metal center, as suggested from work with molecular complexes [49]. The process is reversible. In H_2 ring opening can occur via two paths (Fig. 4.11 (b)). The strong intensity of the $\nu(CH_2)$ band suggests that the surface species formed by hydrogenation of the adsorbed GVL has more CH_2 bonds, so that ring-opening by the top branch (Path 1 in Fig. 4.11 (b)) is the main pathway of GVL conversion, as it produces three CH_2 groups from two. The bottom branch (Path 2) forms an intermediate that retains two CH_2 groups and cannot explain the intensity changes.

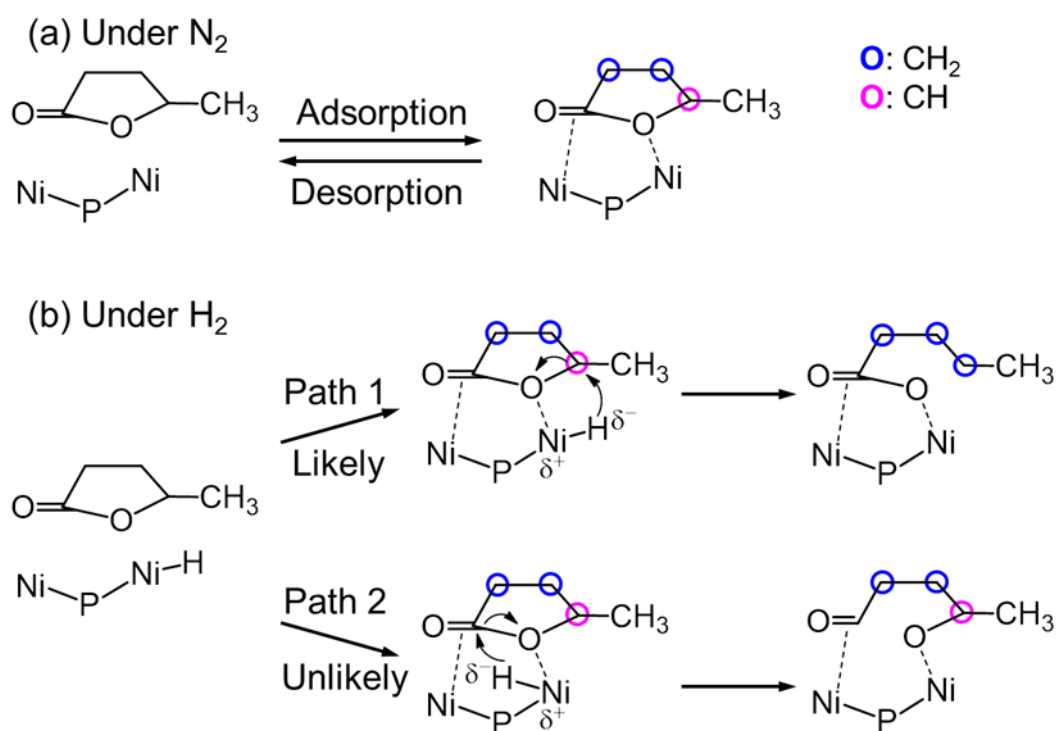


Figure 4.11. (a) Under N_2 , simple adsorption/desorption, (b) Under H_2 , two possible surface ring-opening pathways

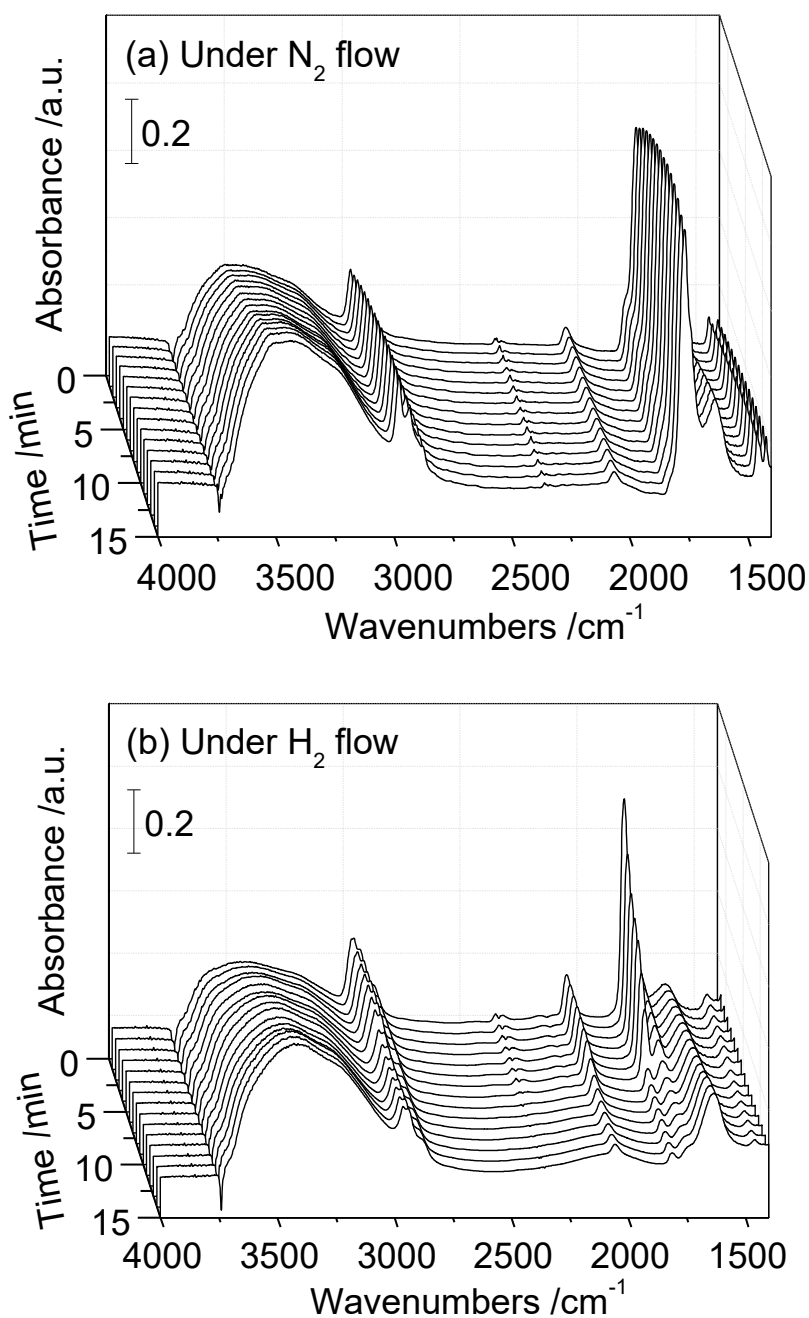


Figure 4.12. Transient spectra for desorption of GVL on Ni₂P/MCM-41 under (a) N₂ flow and (b) H₂ flow at 300 °C and 0.5 MPa

To gain insight on the state of the surface during reaction, a transient analysis was carried out for the desorption of GVL from Ni₂P/MCM-41 under N₂ and H₂ at 300 °C and 0.5 MPa as shown in Fig. 4.12. Prior to the measurements, the catalyst was

pretreated at 550 °C for 3 h with H₂. The spectra were recorded after saturation of GVL on the catalyst surface for 0.2 h at 300 °C and 0.5 MPa under H₂ or N₂ flow (50 ml/min). The peaks in the 3000-2900 cm⁻¹ range correspond to C–H stretches of adsorbed species and showed different behaviors. In N₂ the band at 2980 cm⁻¹ due to CH₃ groups was dominant, while in H₂ the band at 2940 cm⁻¹ corresponding to the CH₂ contribution was the main feature. These results are consistent with the results of adsorption mode depicted in Fig. 4.11. Also the main differences are that in N₂ flow the peaks at around 1700-1500 cm⁻¹ were constant with the time on stream, while in H₂ flow the peaks did change significantly with increasing the peak at 1642 cm⁻¹. These results suggest that reactive H₂ accelerated surface reaction and desorption of adsorbed GVL or/and intermediates and inert N₂ did not change significantly surface reaction.

4.3.5 In situ extended X-ray absorption fine structure (EXAFS) analysis

Fig. 4.13 shows the changes of the XANES signal at 8347 eV and 8333 eV of the passivated Ni₂P/MCM-41 (30 mg) during temperature-programmed reduction under H₂ flow (50 ml/min). All the data underwent background subtraction and normalization to the edge-jump in ATHENA0.8.56. The peak at 8347 eV is known as the white line and tracks the oxidation state of the Ni species [33, 50], while the peak at 8333 eV is a pre-edge feature related to Ni coordination and symmetry [33, 50]. As reduction proceeded with increase in temperature the white line peak decreased in intensity while the pre-edge peak increased in size. This is typical behavior in the reduction of Ni species, and from the flatness of the normalized absorption curves (Fig. 4.13(b)) it can be concluded that the Ni₂P/MCM-41 catalyst was sufficiently reduced at 550 °C after 3 h. It was reported that the reduction process of Ni₂P/K-USY consisted of three reduction

phases, phase I for the decomposition of Ni(OH)₂ to disperse Ni²⁺ species, phase II for the loss of Ni-O bonding without change in structure, and phase III for simultaneous reduction of NiO and phosphidation [51]. Similar phases seem to exist for the current Ni₂P catalyst (Fig. 4.13(b)).

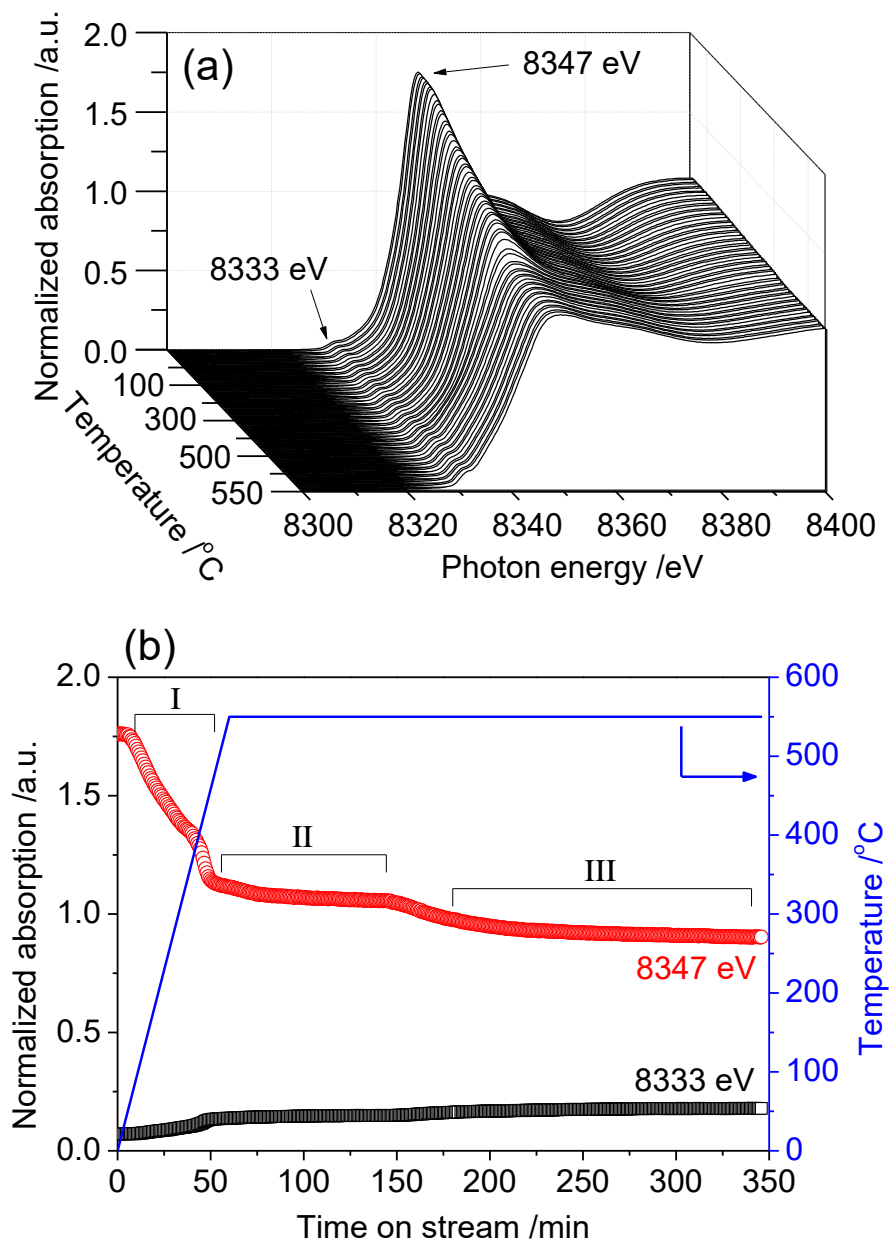


Figure 4.13. Changes of XANES spectra at 8347 eV and 8333 eV on the passivated Ni₂P/MCM-41 catalyst (30 mg) during temperature-programmed reduction under H₂ flow (50 ml/min) at 0.1 MPa (a) Spectral changes (b) Plots of intensities.

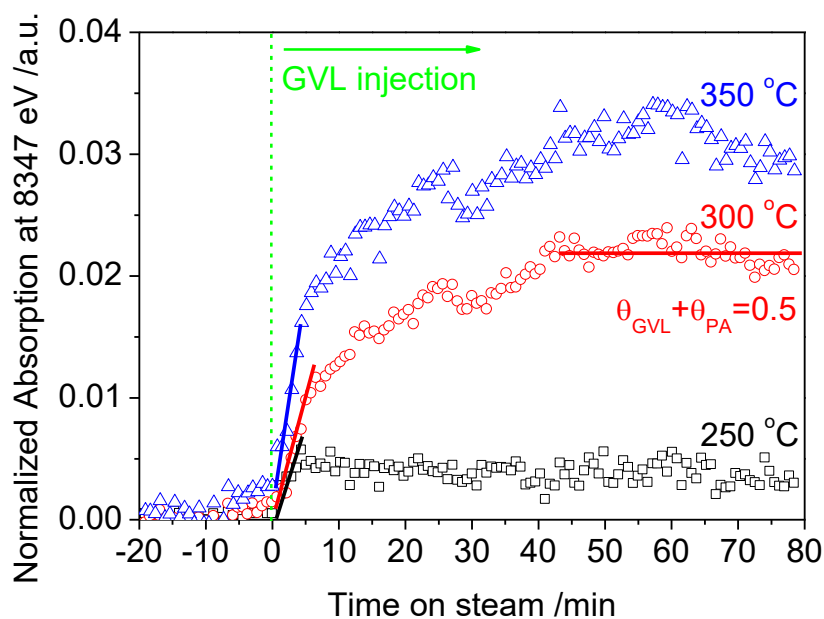


Figure 4.14. Transient XANES signal at 8347 eV before and after GVL injection at 250, 300, and 350 °C and 0.5 MPa under H₂ with 4 mol% GVL

In order to investigate the working state of Ni during the reaction, the intensity of the signal at 8347 eV was plotted as a function of time on stream at 250-350 °C and 0.5 MPa with 4 mol% GVL in H₂ flow as shown in Fig. 4.14. The change of absorbance at 8347 eV was larger than that of the absorbance at 8331 eV before and after reduction, so the former was used to track the state of the Ni species. Before introduction of the reactant the signals were stable at all temperatures indicating that Ni was in the same initial reduced state. The signal is normalized to the edge-jump, and a zero absorption in the reduced state. At 250 °C, the changes in absorbance were very small, while at higher temperature, significant changes in absorbance were observed with the absorbance increasing as temperature was increased. The attainment of unchanging spectra with stable signals at all temperatures indicate that steady-state was reached, and that the catalyst was stable during reaction. These results are consistent with the activity results

as a function of temperature, where the GVL conversion increased rapidly as temperature was increased [41]. This suggests that at higher temperature the adsorption and transformation of GVL to intermediates on Ni sites were enhanced, resulting in the formation of Ni⁺ on the surface (Fig. 12). Since the formation Ni^{δ+} is associated with adsorbates, the absorption curves can be related to the coverages of GVL and pentanoic acid obtained from Fig. 8. This allows calculation of initial slopes, dθ/dt (Fig. 4.14), which follow the order: 0.19 s⁻¹ at 350 °C > 0.05 s⁻¹ at 300 °C > 0.02 s⁻¹ at 250 °C. Furthermore, the comparison of initial slopes in He and H₂ at 300 °C and 0.5 MPa with 4 mol% GVL is shown in Fig. 4.15.

In He flow, the change in coverage with time gives the net rate of adsorption (rate of adsorption (r_{ads}) minus rate of desorption (r_{des})).

$$\left(\frac{d\theta}{dt}\right)_{He} = r_{ads} - r_{des}$$

In H₂ flow, the change in coverage with time represents the net rate of adsorption minus the rate of GVL reaction (r_{rxn}).

$$\left(\frac{d\theta}{dt}\right)_{H_2} = r_{ads} - r_{des}$$

The difference in the changes in coverage under He and H₂ gives the rate of GVL reaction.

$$\left(\frac{d\theta}{dt}\right)_{He} - \left(\frac{d\theta}{dt}\right)_{H_2} = r_{rxn}$$

Thus, at 300 °C and 0.5 MPa the GVL reaction rate can be calculated to be

$$\left(\frac{d\theta}{dt}\right)_{He} - \left(\frac{d\theta}{dt}\right)_{H_2} = 0.23 \text{ s}^{-1} - 0.05 \text{ s}^{-1} = 0.18 \text{ s}^{-1}$$

Although the coverage (θ) was calculated with sum of the coverages in GVL and pentanoic acid, the calculated reaction rate (0.18 s⁻¹) is close to the obtained

turnover frequency (0.17 s^{-1}) from steady-state activity testing in Fig. 4.7 (b). This agreement indicates that surface reaction involving the formation of $\text{Ni}^{\delta+}$ due to Ni-O intermediates is a key step.

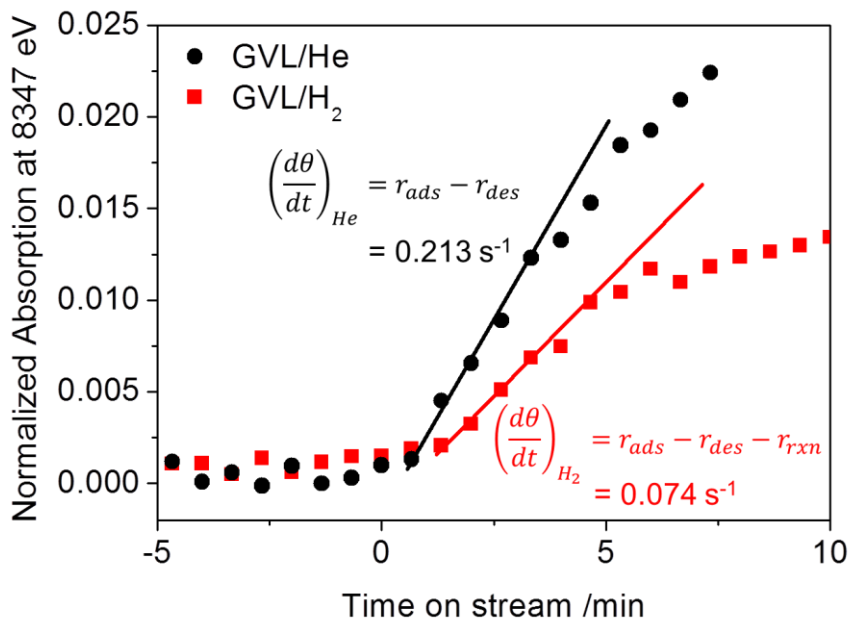


Figure 4.15. Initial slope in normalized absorption at 8347 eV under He and H₂ at 300 °C and 0.5 MPa with 4 mol% GVL.

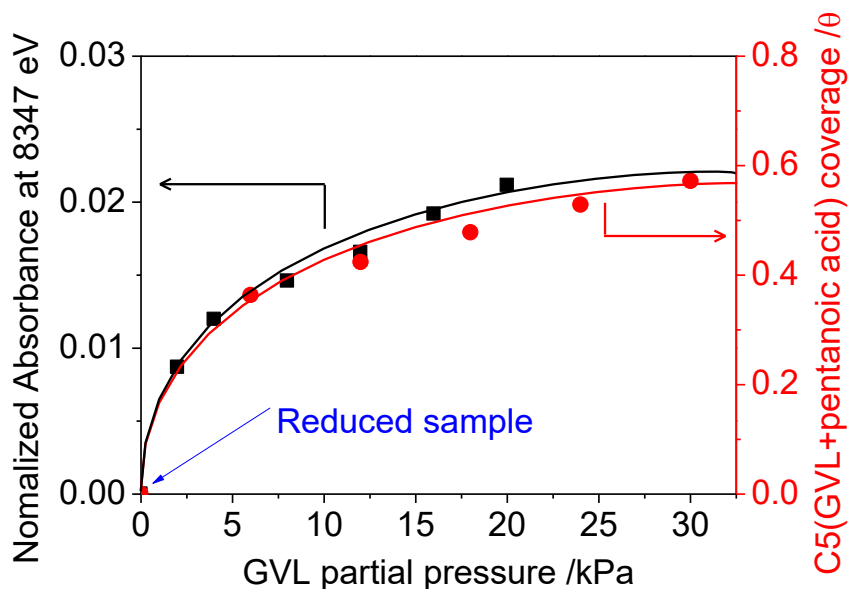


Figure 4.16. Normalized absorbance at 8347 eV and sum of GVL and pentanoic acid coverages as a function of GVL partial pressure at 300 °C and 0.5 MPa

Fig. 4.16 shows the normalized absorbance at 8347 eV and the sum of the coverages of GVL and pentanoic acid as a function of GVL partial pressure. It can be seen that the two curves follow the same trend, in which the absorbance and the C5 coverage increased with increasing GVL partial pressure. This result reveals that the intermediate compounds were adsorbed on the Ni centers rather than on the support or on phosphorous. This is in accordance with the view that Ni₂P is the catalytic active species in the reaction.

4.4. Conclusions

A highly dispersed Ni₂P catalyst supported on MCM-41 was synthesized by temperature-programmed reduction of a phosphite precursor and was tested for the hydrodeoxygenation (HDO) of gamma-valerolactone (GVL) at 0.5 MPa. A contact time study allowed determination of the reaction pathway and the estimation of the reaction constants of each step. There are two routes: the first route involves ring-opening of the lactone on the methyl-substituted side and the second route involves removal of the oxygen from the carbonyl group. Along the first route, which was proposed pentanoic acid is formed initially, which is then converted into pentanal. Following this, n-butene is produced by decarbonylation with the formation of CO, and the n-butene was further hydrogenated to n-butane. The pentanal could also be hydrogenated sequentially to n-pentane but this was not preferred. Simulated fitting results to a first-order network showed good agreement with the experimental results. From partial pressure analysis, it was concluded that higher H₂ partial pressure favors hydrogenation and enhances the overall reaction rate. In situ infrared spectroscopy measurements indicated that an intermediate with greater number of CH₂ groups than GVL was formed at reaction

conditions, and this gave support for the proposed reaction mechanism, in which the initial reaction led to the production of pentanoic acid which has more CH₂ bonds than GVL. In situ quick X-ray absorption fine structure (QXAFS) measurements confirmed that with increasing activity more reactant adsorbed on Ni sites, and as a result, the effect of GVL concentration exhibited the same behavior as that calculated from the coverage of C5 compounds. These include the GVL and pentanoic acid. Overall, the combined kinetic and spectroscopic results give a consistent picture of the mechanism of GVL hydrodeoxygenation on Ni₂P/MCM-41.

References

- [1] L. Soh, M.J. Eckelman, Green solvents in biomass processing, *ACS Sustain. Chem. Eng.* 4 (2016) 5821-5837.
- [2] A.M. Robinson, J.E. Hensley, J.W. Medlin, Bifunctional catalysts for upgrading of biomass-derived oxygenates: A review, *ACS Catal.* 6 (2016) 5026-5043.
- [3] R.A. Sheldon, Green chemistry, catalysis and valorization of waste biomass, *J. Mol. Catal. A: Chem.* 422 (2016) 3-12.
- [4] M.J.C. van der Stelt, H. Gerhauser, J.H.A. Kiel, K.J. Ptasinski, Biomass upgrading by torrefaction for the production of biofuels: A review, *Biomass Bioenerg* 35 (2011) 3748-3762.
- [5] Y.Y. Mei, Q.F. Che, Q. Yang, C. Draper, H.P. Yang, S.H. Zhang, H.P. Chen, Torrefaction of different parts from a corn stalk and its effect on the characterization of products, *Ind. Crop. Prod.* 92 (2016) 26-33.
- [6] P.Q. Sun, M.X. Heng, S.H. Sun, J.W. Chen, Direct liquefaction of paulownia in hot compressed water: Influence of catalysts, *Energy* 35 (2010) 5421-5429.
- [7] G. Haarlemmer, C. Guizani, S. Anouti, M. Deniel, A. Roubaud, S. Valin, Analysis and comparison of bio-oils obtained by hydrothermal liquefaction and fast pyrolysis of beech wood, *Fuel* 174 (2016) 180-188.
- [8] H.M. Wang, J. Male, Y. Wang, Recent advances in hydrotreating of pyrolysis bio-oil and its oxygen-containing model compounds, *ACS Catal.* 3 (2013) 1047-1070.
- [9] Y. Xue, S. Zhou, R.C. Brown, A. Kelkar, X.L. Bai, Fast pyrolysis of biomass and waste plastic in a fluidized bed reactor, *Fuel* 156 (2015) 40-46.
- [10] W.F. Cai, R.H. Liu, Performance of a commercial-scale biomass fast pyrolysis plant for bio-oil production, *Fuel* 182 (2016) 677-686.
- [11] N. Koike, S. Hosokai, A. Takagaki, S. Nishimura, R. Kikuchi, K. Ebitani, Y. Suzuki, S.T. Oyama, Upgrading of pyrolysis bio-oil using nickel phosphide catalysts, *J. Catal.* 333 (2016) 115-126.
- [12] Y.B. Huang, L. Wei, X.H. Zhao, S.Y. Cheng, J. Julson, Y.H. Cao, Z.R. Gu, Upgrading pine sawdust pyrolysis oil to green biofuels by HDO over zinc-assisted Pd/C catalyst, *Energy Convers. Manage.* 115 (2016) 8-16.
- [13] T. Cordero-Lanzac, R. Palos, J.M. Arandes, P. Castano, J. Rodriguez-Mirasol, T. Cordero, J. Bilbao, Stability of an acid activated carbon based bifunctional

-
- catalyst for the raw bio-oil hydrodeoxygenation, *Appl. Catal. B: Environ.* 203 (2017) 389-399.
- [14] V. Itthibenchapong, A. Srifa, R. Kaewmeesri, P. Kidkhunthod, K. Faungnawakij, Deoxygenation of palm kernel oil to jet fuel-like hydrocarbons using Ni-MoS₂/γ-Al₂O₃ catalysts, *Energy Convers. Manage.* 134 (2017) 188-196.
- [15] A. Iino, A. Cho, A. Takagaki, R. Kikuchi, S.T. Oyama, Kinetic studies of hydrodeoxygenation of 2-methyltetrahydrofuran on a Ni₂P/SiO₂ catalyst at medium pressure, *J. Catal.* 311 (2014) 17-27.
- [16] A. Cho, H. Kim, A. Iino, A. Takagaki, S.T. Oyama, Kinetic and FTIR studies of 2-methyltetrahydrofuran hydrodeoxygenation on Ni₂P/SiO₂, *J. Catal.* 318 (2014) 151-161.
- [17] H. Song, J. Gong, H.L. Song, F. Li, A novel surface modification approach for synthesizing supported nickel phosphide catalysts with high activity for hydrodeoxygenation of benzofuran, *Appl. Catal. A: Gen.* 505 (2015) 267-275.
- [18] I.T. Ghampson, C. Sepulveda, A.B. Dongil, G. Pecchi, R. Garcia, J.L.G. Fierro, N. Escalona, Phenol hydrodeoxygenation: effect of support and Re promoter on the reactivity of Co catalysts, *Catal. Sci. Technol.* 6 (2016) 7289-7306.
- [19] I.T. Ghampson, C. Sepulveda, R. Garcia, J.L.G. Fierro, N. Escalona, Carbon nanofiber-supported ReOx catalysts for the hydrodeoxygenation of lignin-derived compounds, *Catal. Sci. Technol.* 6 (2016) 4356-4369.
- [20] V.O.O. Goncalves, P.M. de Souza, V.T. da Silva, F.B. Noronha, F. Richard, Kinetics of the hydrodeoxygenation of cresol isomers over Ni₂P/SiO₂: Proposals of nature of deoxygenation active sites based on an experimental study, *Appl. Catal. B: Environ.* 205 (2017) 357-367.
- [21] P.P. Bui, S.T. Oyama, A. Takagaki, B.P. Carrow, K. Nozaki, Reactions of 2-methyltetrahydropyran on silica-supported nickel phosphide in comparison with 2-methyltetrahydrofuran, *ACS Catal.* 6 (2016) 4549-4558.
- [22] T.A. Le, H.V. Ly, J. Kim, S.S. Kim, J.H. Choi, H.C. Woo, M.R. Othman, Hydrodeoxygenation of 2-furyl methyl ketone as a model compound in bio-oil from pyrolysis of *Saccharina Japonica* Alga in fixed-bed reactor, *Chem. Eng. J.* 250 (2014) 157-163.

-
- [23] A. Popov, E. Kondratieva, L. Mariey, J.M. Goupil, J. El Fallah, J.P. Gilson, A. Travert, F. Mauge, Bio-oil hydrodeoxygenation: Adsorption of phenolic compounds on sulfided (Co)Mo catalysts, *J. Catal.* 297 (2013) 176-186.
- [24] A.L. Jongorius, R. Jastrzebski, P.C.A. Bruijninx, B.M. Weckhuysen, CoMo sulfide-catalyzed hydrodeoxygenation of lignin model compounds: An extended reaction network for the conversion of monomeric and dimeric substrates, *J. Catal.* 285 (2012) 315-323.
- [25] Y.W. Bie, J. Lehtonen, J. Kanervo, Hydrodeoxygenation (HDO) of methyl palmitate over bifunctional Rh/ZrO₂ catalyst: Insights into reaction mechanism via kinetic modeling, *Appl. Catal. A: Gen.* 526 (2016) 183-190.
- [26] T.-S. Nguyen, D. Laurenti, P. Afanasiev, Z. Konuspayeva, L. Piccolo, Titania-supported gold-based nanoparticles efficiently catalyze the hydrodeoxygenation of guaiacol, *J. Catal.* 344 (2016) 136-140
- [27] M. Shetty, K. Murugappan, T. Prasomsri, W.H. Green, Y. Roman-Leshkov, Reactivity and stability investigation of supported molybdenum oxide catalysts for the hydrodeoxygenation (HDO) of m-cresol, *J. Catal.* 331 (2015) 86-97.
- [28] J.S. Moon, E.G. Kim, Y.K. Lee, Active sites of Ni₂P/SiO₂ catalyst for hydrodeoxygenation of guaiacol: A joint XAFS and DFT study, *J. Catal.* 311 (2014) 144-152.
- [29] L.F. Feitosa, G. Berhault, D. Laurenti, T.E. Davies, V.T. da Silva, Synthesis and hydrodeoxygenation activity of Ni₂P/C - Effect of the palladium salt on lowering the nickel phosphide synthesis temperature, *J. Catal.* 340 (2016) 154-165.
- [30] S. Boullosa-Eiras, R. Lodeng, H. Bergem, M. Stocker, L. Hannevold, E.A. Blekkana, Catalytic hydrodeoxygenation (HDO) of phenol over supported molybdenum carbide, nitride, phosphide and oxide catalysts, *Catal. Today* 223 (2014) 44-53.
- [31] L. Nie, D.E. Resasco, Kinetics and mechanism of m-cresol hydrodeoxygenation on a Pt/SiO₂ catalyst, *J. Catal.* 317 (2014) 22-29.
- [32] P. Bui, A. Takagaki, R. Kikuchi, S.T. Oyama, Kinetic and infrared spectroscopy study of hydrodeoxygenation of 2-methyltetrahydrofuran on a nickel phosphide catalyst at atmospheric pressure, *ACS Catal.* 6 (2016) 7701-7709.

-
- [33] S.T. Oyama, T. Gott, K. Asakura, S. Takakusagi, K. Miyazaki, Y. Koike, K.K. Bando, In situ FTIR and XANES studies of thiophene hydrodesulfurization on Ni₂P/MCM-41, *J. Catal.* 268 (2009) 209-222.
- [34] K.K. Bando, T. Wada, T. Miyamoto, K. Miyazaki, S. Takakusagi, Y. Koike, Y. Inada, M. Nomura, A. Yamaguchi, T. Gott, S.T. Oyama, K. Asakura, Combined in situ QXAFS and FTIR analysis of a Ni phosphide catalyst under hydrodesulfurization conditions, *J. Catal.* 286 (2012) 165-171.
- [35] T. Wada, K.K. Bando, S.T. Oyama, T. Miyamoto, S. Takakusagi, K. Asakura, Operando observation of Ni₂P structural changes during catalytic reaction: Effect of H₂S pretreatment, *Chem. Lett.* 41 (2012) 1238-1240.
- [36] H.M. Wang, E. Iglesia, Thiophene hydrodesulfurization catalysis on supported Ru clusters: Mechanism and site requirements for hydrogenation and desulfurization pathways, *J. Catal.* 273 (2010) 245-256.
- [37] L. Zhang, W.Q. Fu, Q.Y. Yu, T.D. Tang, Y.C. Zhao, Y.D. Li, Effect of citric acid addition on the morphology and activity of Ni₂P supported on mesoporous zeolite ZSM-5 for the hydrogenation of 4,6-DMDBT and phenanthrene, *J. Catal.* 345 (2017) 295-307.
- [38] S.T. Oyama, T. Onkawa, A. Takagaki, R. Kikuchi, S. Hosokai, Y. Suzuki, K.K. Bando, Production of phenol and cresol from guaiacol on nickel phosphide catalysts supported on acidic supports, *Top. Catal.* 58 (2015) 201-210.
- [39] J.A. Cecilia, A. Infantes-Molina, E. Rodriguez-Castellon, A. Jimenez-Lopez, S.T. Oyama, Oxygen-removal of dibenzofuran as a model compound in biomass derived bio-oil on nickel phosphide catalysts: Role of phosphorus, *Appl. Catal. B: Environ.* 136 (2013) 140-149.
- [40] A. Cho, A. Takagaki, R. Kikuchi, S.T. Oyama, Active Sites in Ni₂P/USY Catalysts for the Hydrodeoxygenation of 2-Methyltetrahydrofuran, *Top. Catal.* 58 (2015) 219-231.
- [41] G.N. Yun, A. Takagaki, R. Kikuchi, S.T. Oyama, Hydrodeoxygenation of gamma-valerolactone on transition metal phosphide catalysts, *Catal. Sci. Technol.* 7 (2017) 281-292.
- [42] P. Bui, J.A. Cecilia, S.T. Oyama, A. Takagaki, A. Infantes-Molina, H.Y. Zhao, D. Li, E. Rodriguez-Castellon, A.J. Lopez, Studies of the synthesis of transition

-
- metal phosphides and their activity in the hydrodeoxygenation of a biofuel model compound, *J. Catal.* 294 (2012) 184-198.
- [43] A. Infantes-Molina, J.A. Cecilia, B. Pawelec, J.L.G. Fierro, E. Rodriguez-Castellon, A. Jimenez-Lopez, Ni₂P and CoP catalysts prepared from phosphite-type precursors for HDS-HDN competitive reactions, *Appl. Catal. A: Gen.* 390 (2010) 253-263.
- [44] D.R. Stull, Vapor pressure of pure substances - Organic compounds, *Ind. Eng. Chem.* 39 (1947) 517-540.
- [45] S. Oyama, X. Zhang, J. Lu, Y. Gu, T. Fujitani, Epoxidation of propylene with H₂ and O₂ in the explosive regime in a packed-bed catalytic membrane reactor, *J. Catal.* 257 (2008) 1-4.
- [46] P.B. Weisz, C.D. Prater, Interpretation of measurements in experimental catalysis, *Adv. Catal.* 6 (1954) 143-196.
- [47] J. Pritchard, G. A. Filonenko, R. van Putten, E. J. M. Hensen, E.A. Pidko, Heterogeneous and homogeneous catalysis for the hydrogenation of carboxylic acid derivatives: history, advances and future directions, *Chem. Soc. Rev.* 44 (2015) 3808-3833.
- [48] W. Kuriyama, T. Matsumoto, O. Ogata, Y. Ino, K. Aoki, S. Tanaka, K. Ishida, T. Kobayashi, N. Sayo and T. Saito, Catalytic hydrogenation of esters. Development of an efficient catalyst and processes for synthesising (*R*)-1,2-propanediol and 2-(*l*-menthoxy)ethanol, *Org. Process Res. Dev.*, 2011, 16, 166–171.
- [49] M. Mavrikakis, M.A. Barteau, Oxygenate reaction pathways on transition metal surfaces, *J. Mol. Catal. A: Chem.* 131 (1998) 135-147.
- [50] M. Fernandez-Garcia, Xanes analysis of catalytic systems under reaction conditions, *Catal Rev* 44 (2002) 59-121.
- [51] K.K. Bando, Y. Koike, T. Kawai, G. Tateno, S.T. Oyama, Y. Inada, M. Nomura, K. Asakura, Quick X-ray absorption fine structure studies on the activation process of Ni₂P supported on K-USY, *J. Phys. Chem. C* 115 (2011) 7466-7471.

Chapter 5

General Conclusions

This work focused on the catalytic hydrodeoxygenation (HDO) of the cyclic five-membered ester γ -valerolactone (GVL- $C_5H_8O_2$) on a series of supported metal phosphide catalysts and the kinetic analysis of reaction network of GVL on Ni₂P/MCM-41. In addition, a special focus was given to the adsorbed species on the catalyst surface and the working state of Ni species during the reaction were monitored by in situ infrared spectroscopy and in situ quick x-ray adsorption fine structure measurement to support the proposed reaction sequence. These measurements and analyses are important to obtain basic information about the manner of oxygen removal from pyrolysis oil using Ni₂P/MCM-41.

Chapter 2 describes the HDO of GVL on a series of transition metal phosphides supported on MCM-41. Highly dispersed phosphide catalysts were successfully synthesized. The activity for GVL conversion and deoxygenation degree followed the order: Ni₂P/MCM-41 >> CoP/MCM-41 >> Pd/Al₂O₃ \approx MoP/MCM-41 > WP/MCM-41. The iron group phosphide catalysts (Ni₂P/MCM-41 and CoP/MCM-41) and Pd/Al₂O₃ follow a decarbonylation pathway whereas group 6 phosphides (MoP/MCM-41 and WP/MCM-41) follow an HDO pathway in the removal of oxygen. The iron group phosphides and Pd/Al₂O₃ showed high hydrogenation ability to form saturated hydrocarbons.

Chapter 3 describes the HDO of GVL on a series of supported NiMo bimetallic phosphides catalysts (NiMoP/MCM-41). The formation of Ni and Mo alloy was confirmed by shifts of diffraction peak positions from XRD patterns. Deconvolution of

the IR spectra of CO adsorbed on the bimetallic phosphide catalysts revealed contributions from Ni and Mo sites; consequently, the number of Ni active sites was estimated by factor analysis of the deconvoluted peaks and the CO uptake values obtained from chemisorption measurements. The activity was related to the proportion of Ni in the catalyst, following the order: Ni₂P/MCM-41 > NiMo(3:1)P/MCM-41 > NiMo(1:1)P/MCM-41 \cong (Ni₂P+MoP)/MCM-41 > NiMo(1:3)P/MCM-41 > MoP/MCM-41, indicating that Ni was the major active site, while Mo was a diluent. This interpretation is confirmed by results of TOF normalized by accessible Ni sites which revealed that the effect of alloying on the activity was very small. Therefore, a single Ni atom was involved in the rate-determining step. In contrast to TOF results, the presence of Mo sites had a significant effect on the product selectivity: Ni₂P/MCM-41 mostly produced butane, whereas Mo-containing catalysts produced higher amount of 1-pentanol and C5 hydrocarbons such as pentane and n-pentenes. These results demonstrate that the product selectivity was strongly affected by the neighboring atoms of Ni.

Chapter 4 describes determination of the reaction pathway and the estimation of the reaction constants of each step by a contact time study. There are two routes: the first route involves ring-opening of the lactone on the methyl-substituted side and the second route involves removal of the oxygen from the carbonyl group. Along the first route, which was proposed pentanoic acid is formed initially, which is then converted into pentanal. Following this, n-butene is produced by decarbonylation with the formation of CO, and the n-butene was further hydrogenated to n-butane. The pentanal could also be hydrogenated sequentially to n-pentane but this was not preferred. Simulated fitting results to a first-order network showed good agreement with the

experimental results. From partial pressure analysis, it was concluded that higher H_2 partial pressure favors hydrogenation and enhances the overall reaction rate. In situ infrared spectroscopy measurements indicated that an intermediate with greater number of CH_2 groups than GVL was formed at reaction conditions, and this gave support for the proposed reaction mechanism, in which the initial reaction led to the production of pentanoic acid which has more CH_2 bonds than GVL. In situ quick X-ray absorption fine structure (QXAFS) measurements confirmed that with increasing activity more reactant adsorbed on Ni sites, and as a result, the effect of GVL concentration exhibited the same behavior as that calculated from the coverage of C5 compounds. These include the GVL and pentanoic acid. Overall, the combined kinetic and spectroscopic results give a consistent picture of the mechanism of GVL hydrodeoxygenation on $Ni_2P/MCM-41$.

Publication List

1. **Gwang-Nam Yun**, Atsushi Takagaki, Ryuji Kikuchi and S. Ted Oyama, “Hydrodeoxygenation of γ -valerolactone on transition metal phosphide catalysts”, Catal. Sci. Technol., 7 (2017) 281 (contribution: 1.0)
2. **Gwang-Nam Yun**, So-Jin Ahn, Atsushi Takagaki, Ryuji Kikuchi and S. Ted Oyama, “Hydrodeoxygenation of γ -valerolactone on bimetallic NiMo phosphide catalysts”, accepted (contribution: 0.9)
3. **Gwang-Nam Yun**, So-Jin Ahn, Atsushi Takagaki, Ryuji Kikuchi and S. Ted Oyama, “Catalytic mechanism of GVL HDO on NiMo(1:1)P/MCM-41 catalyst”, in preparation (contribution: 0.9)
4. **Gwang-Nam Yun**, So-Jin Ahn, Kyoko Bando, Atsushi Takagaki, Ryuji Kikuchi and S. Ted Oyama, “Kinetic and spectroscopic studies of catalytic mechanisms: Hydrodeoxygenation of gamma-valerolactone on Ni₂P/MCM-41”, in preparation. (contribution: 0.9)
5. So-Jin Ahn, **Gwang-Nam Yun**, Atsushi Takagaki, Ryuji Kikuchi and S. Ted Oyama, “Synthesis and characterization of hydrogen selective silica membrane prepared by chemical vapor deposition of vinyltriethoxysilane”, J. Membr. Sci., submitted. (contribution: 0.1)
6. So-Jin Ahn, **Gwang-Nam Yun**, Atsushi Takagaki, Ryuji Kikuchi, S. Ted Oyama, “Dehydrogenation of Ethane over Cr/ZSM-5 Catalyst in Hydrogen Selective Silica-based Membrane Reactor”, in preparation. (contribution: 0.1)
7. Jianwen Zhang, Kazuki Matsubara, **Gwang-Nam Yun**, Huidong Zheng, Atsushi Takagaki, Ryuji Kikuchi, S. Ted Oyama, “Comparison of Phosphide Catalysts Prepared by Temperature-Programmed Reduction and Liquid-Phase Methods in the Hydrodeoxygenation of 2-Methylfuran”, Appl. Catal. A. accepted. (contribution: 0.1)

Acknowledgment

I would like to say this work could not be completed without assistances from many people who I am deeply indebted.

First and foremost, I would like to express my sincere gratitude to my advisor, Prof. Shigeo Ted Oyama, who has given me the opportunity to study in Japan and has supported me throughout my doctor course with his patience, encouragement, advice and financial support. I also appreciate the efforts made by the committee members Prof. Kazunari Domen, Prof. Masaru Ogura, Prof. Tetsuya Shishido, Prof. Ryuji Kikuchi, and Prof. Tsutomu Minegishi.

I am deeply thankful to Dr. Kyoko Bando and Dr. Astushi Takagaki for their on-site teaching and advices, especially on journey of EXAFS measurements in Tsukuba. Without their supports I couldn't get any forwarder in my research and experiments.

Special thanks to Prof. Yong-Kul Lee for his continuous help in my study and life. His discerning directions have made me strong and upright in difficult circumstances.

During the last three years, our research group has given me overcome learning barriers with a wide variety of comments and helped me broaden my academic and professional perspectives. I would like to thank to our past and current group members for their help and strong interaction: Dr. Qing, Dr. Tyrone, Dr. Phoung, Dr. Shouha, Kageyama, Vibin, Koike, Goto, Marina, Mishina, Fujiwara, Namba.

I would like to thank my parents, Young-Don Yun and Hea-Ok Kim, my elder sister, Na-Rae Yun, and family in law for their faith in me and allowing me to be as ambitious as I wanted. They have always encouraged me with incessant love and careful consideration in any circumstance.

I also would like to thank Korean colleagues in the University of Tokyo, especially @5 members, Jeong-Hyun, Hye-Min, Sae-Mi, and Soo-Min. It would have been a lonely campus life without them.

Finally, and most importantly, I would like to thank my wife So-Jin Ahn. She has been my classmate for 10 years and, even now she is working on right next to me. Her support, encouragement, patience and unwavering love were undeniably the root of the force that sustains me.